

Imperial College London
Department of Electrical and Electronic Engineering

Design and Development of Safety Systems for High Frequency Inductive Power Transfer

Lingxin (Steve) Lan

November 2021

A thesis submitted for the degree of Doctor of Philosophy of
Imperial College London and the Diploma of Imperial College

Abstract

As wireless charging is gaining its popularity among consumer electronics, e.g., phones, smart wearables, electric toothbrushes, etc., there has been a trend of expanding this technology into a wider range of applications e.g. drones, robots, electric vehicles etc.. To achieve this, both the charging power and range need to be increased. This thesis discusses the limitations of widely used kHz inductive power transfer systems and emphasises the challenge of deploying into a wider range of applications. High-frequency inductive power transfer (HF-IPT) systems are then discussed with two real-world applications presented to showcase HF-IPT's potential over kHz IPT systems. Some of the benefits of the HF-IPT, e.g., the large air gap and tolerance to misalignment, could increase the chances for live or other unintended objects to be coupled into the wireless charging system, which could cause safety hazards if the system was not designed carefully. This thesis, therefore, focuses on the safety systems design and development for HF-IPT systems.

A number of existing and potential foreign and live object detection methods (FOD/LOD) including a new FOD/LOD method based on reflected impedance are introduced. The proposed method can operate without additional sensors, and without a communication link between IPT transmitter and receiver. A detection accuracy of 95% is achieved by implementing such FOD/LOD method. In addition, a FOD/LOD technique based on a mmWave radar sensor is also introduced. Differing from typical radar applications, the proposed method leverages machine learning techniques to perform object recognition to reduce the false detection rate. The developed FOD/LOD system could classify six different charging scenarios with an average accuracy of 96%. For applications that do not involve any live or unintended objects, this thesis also introduces a localisation technique based on the IPT system to help guide a drone or robot to a specific location e.g. a wireless charging point. Such a system was designed to reduce the risk of charging by minimising human's involvement.

Declarations

I herewith certify that all materials in this thesis which is not my own work, have been properly acknowledged.

The copyright of this thesis rests with the author. Unless otherwise indicated, its contents are licensed under a Creative Commons Attribution-Non Commercial 4.0 International Licence (CC BY-NC).

Under this licence, you may copy and redistribute the material in any medium or format. You may also create and distribute modified versions of the work. This is on the condition that: you credit the author and do not use it, or any derivative works, for a commercial purpose.

When reusing or sharing this work, ensure you make the licence terms clear to others by naming the licence and linking to the licence text. Where a work has been adapted, you should indicate that the work has been changed and describe those changes.

Please seek permission from the copyright holder for uses of this work that are not included in this licence or permitted under UK Copyright Law.

Acknowledgements

I have to start by thanking my awesome parents, Guilan Qiu and Jianhua Lan, who have been unconditionally supporting me through my whole PhD study, none of this would have been accomplished without them.

I am deeply grateful to Prof. Paul Mitcheson, who not only gave me this opportunity to be involved in this game-changing technology but also provided me with great support and guidance through my PhD, not only as my supervisor, but also as my friend. I would also like to thank Dr. David Yates. Like Paul, Dave is also very passionate towards wireless power, and he has offered a lot of help with many technical discussions.

I would also like to express my sincere gratitude to current and former members of the Wireless Power Lab: Christopher Kwan, Juan Arteaga, Ioannis Nikiforidis, Nunzio Pucci, James Lawson, Samer Aldhaher, and George Kkelis, I really appreciate for all the help you offered through my PhD and it has been a great pleasure to work with you guys.

I would also like to thank Yuan Qin, Tommaso Polonelli, and Niall Woodward for the collaboration of the Sensor network and IPT localisation part of the thesis. Alexander Aujla-Jones is also acknowledged for helping with the mmWave foreign object detection work.

The funding from UK EPSRC Centre for Power Electronics is acknowledged for the 100 W drone wireless charging research. The funding from Her Majesty's Government for the sensor network charging research is also gratefully acknowledged.

Contents

Abstract	3
Declarations	5
Acknowledgements	7
1 Introduction	21
1.1 Background	27
1.1.1 Inductive Power Transfer	27
1.1.2 High-frequency IPT systems	30
1.1.3 Safety of IPT systems	34
1.1.4 Research Areas and Thesis Outline	42
2 End-to-end HF-IPT Systems	43
2.1 Design and Development of a 100 W Wireless UAV Charger	44
2.1.1 System Design	46
2.1.2 Testing	53
2.1.3 Summary	56

2.2	Building an IPT System for Sensor Network Re-charging	57
2.2.1	System Overview	58
2.2.2	The Integration of IPT Transmitter into a Drone	59
2.2.3	The IPT Receive-side Electronics and Sensor Node	61
2.2.4	The User Interface	64
2.2.5	Summary	65
3	Analysis of Foreign/ Living Object Detection Methods	66
3.1	Properties Definition	67
3.2	Analysis of Existing and Potential IPT FOD/LOD Implementations	69
3.2.1	Q-factor measurement method	70
3.2.2	Efficiency measurement method	72
3.2.3	Ultrasonic	75
3.2.4	Visible Light	78
3.2.5	Radar	81
3.2.6	Overview of FOD/LOD Implementation	83
4	Impedance Reflection FOD/LOD	85
4.0.1	Load-independent Class EF Inverter	86
4.0.2	Reflected Impedance Estimation	87
4.0.3	Experimental Verification	93
4.1	Impedance Reflection FOD/LOD	95

4.2	Implementation on Low-cost Hardware	96
4.2.1	Sub-sampling	97
4.2.2	Real-time Task on General Purpose Operating System	100
5	mmWave Radar-based FOD/LOD System	105
5.1	Sensor Selection	106
5.2	General Object Detection	106
5.3	System Overview	108
5.4	FOD/LOD by Zone Occupancy	109
5.5	Object classification	111
5.5.1	Data Capture and Preprocessing	112
5.5.2	Neural Network Configuration and Classifier Training	114
5.6	Performance Evaluation	116
5.7	Implementation on Low-cost Hardware	116
5.8	Recommendations	119
6	An IPT-based Localisation Technique	120
6.0.1	Automated Flight Control	121
6.0.2	IPT-based Localisation	122
6.0.3	Experimental Verification	125
6.0.4	Summary	126

7 Conclusion	128
7.0.1 Main Research Outcomes	129
7.1 Author’s Contribution	131
7.2 Publications	134
7.3 Suggestions for Future Work	136
Bibliography	137

List of Tables

1.1	ICNIRP 2010 E- and H-field Reference Level (3 kHz to 10 MHz)	35
1.2	ICNIRP 2010 Basic Restrictions (100 kHz to 6 GHz)	37
2.1	Link parameters for 100 W at minimum coupling with optimal load	48
2.2	Component values of load-independent Class EF inverter	49
2.3	Component values of the rectifier	51
3.1	FOD/LOD methods comparison	83
4.1	Simulation and Experimental Component Values	88
4.2	Network Layers	91
4.3	Estimated Impedance of FO and IPT Receiver (5 cm to the coil)	96
4.4	FOD/LOD methods comparison	96
5.1	Network Layers	115
5.2	FOD/LOD methods comparison	119
6.1	Spice Simulation Component Values	124

List of Figures

1.1	AirPower (Apple Inc.)	21
1.2	AirPower Coil Patent (Apple Inc.)	22
1.3	Inside of the AirPower prototype	23
1.4	Inside of the Xiaomi Auto-tracking Wireless Charger Prototype	25
1.5	Batteryless Drone Powered Wirelessly (BBC)	26
1.6	The relationship between link efficiency, coupling factor and Q-factor [1]	29
1.7	Q-factor of a typical Qi-standard coil	30
1.8	Class EF inverter circuit topology	31
1.9	A comparison of wide-band-gap devices	32
1.10	Class EF inverter circuit with equivalent load	33
1.11	A passive rectifier (full wave rectifier)	33
1.12	A passive rectifier (Class D Half Wave rectifier)	34
1.13	Induction Hob H-field Measurement Setup	36
1.14	Induction Hob H-field Measurement Result	37
1.15	SAR human body simulation	38
1.16	SAR and internal E-field Simulation simulation	39

1.17	A coin heating up on a Qi charger	40
1.18	A coin placed on a 13.56 MHz IPT system	41
1.19	Induction Heating of a CD	42
2.1	The Ingenuity helicopter	45
2.2	A wirelessly charged DJI M100 drone	46
2.3	High-level system block digram of IPT system	46
2.4	Coil and shielding shape and size	47
2.5	Class EF inverter circuit topology	48
2.6	The wireless charging transmitter box	49
2.7	DJI M100 on the edge of the charging pad	50
2.8	Class D rectifier	50
2.9	Full-wave rectifier	51
2.10	Rectifier output voltage at minimum coupling (5%)	52
2.11	Rectifier output voltage at maximum coupling (16.7%)	52
2.12	Receiver side PCB rendering	53
2.13	The wireless power receiver on the drone	54
2.14	IPT receive-side thermal test	55
2.15	DJI M100 approaching the charging pad on the Thales ASV	56
2.16	System Overview	57
2.17	Class EF inverter circuit topology	58
2.18	Inverter (left) and DC/DC converter (right) hardware	59

2.19	Transmit coil attached to the drone	60
2.20	receiver side power electronics	61
2.21	Panasonic 18650 cell (www.nealsgadgets.com)	63
2.22	the sensor node board (Tommaso Polonelli)	63
2.23	A web-based UI	64
3.1	FOD/LOD workflow	67
3.2	Q-factor change with foreign objects (wirelesspowerconsortium.com)	71
3.3	Phone Charging	74
3.4	Phone NOT Charging	74
3.5	A ultrasonic sensor (sparkfun.com)	75
3.6	Automobile parking assist system based on ultrasonic sensors	76
3.7	Object detected on an ultrasonic-based FOD/LOD system	77
3.8	Object not detected on an ultrasonic-based FOD/LOD system	78
3.9	A camera module for Raspberry Pi (raspberrypi.org)	78
3.10	A real-time objector using YOLO (ultralytics.com)	79
3.11	A mmWave radar demo (ti.com)	81
3.12	TI's Proximity Sensors (ti.com)	84
4.1	Class EF inverter circuit topology driving an inductively coupled reflected impedance (Z_{eq}).	86
4.2	Theoretical drain-source voltage waveform under various loading conditions	87
4.3	Class EF circuit simulation on Matlab Simulink	89

4.4	CNN estimation model training process	92
4.5	Photograph of the experimental setup.	93
4.6	Impedance estimation model results from a simulated and an experimental environment.	94
4.7	Altera EP4CE10 EVM	97
4.8	AD9226 ADC Module	97
4.9	Sub-sampling Test Setup	99
4.10	Sine wave	100
4.11	square wave	100
4.12	Sub-sampled Sine waveform	100
4.13	Sub-sampled Square waveform	101
4.14	The ADC board for Raspberry Pi Zero	101
4.15	Sub-sampling a 50.01 MHz Signal with a 10 MHz ADC	104
5.1	IWR6843AOP Evaluation Module (ti.com)	106
5.2	mmWave configuration (dev.ti.com)	107
5.3	3D Scatter Plot	108
5.4	Range Profile Plot	108
5.5	Range Doppler Plot	109
5.6	Azimuth-Range Heatmap Plot	109
5.7	System Overview	110
5.8	E-scooter IPT setup (Christopher Kwan)	110

5.9	Nothing	111
5.10	A person approaching	111
5.11	A person in detection range	111
5.12	A person squatting down	111
5.13	mmWave heatmap plot with an e-scooter	113
5.14	mmWave heatmap plot with a tea can	114
5.15	mmWave heatmap data processing	115
5.16	CNN training process	116
5.17	Result confusion matrix	117
5.18	Background Only	118
5.19	Scooter Only	118
5.20	Human Only	118
5.21	Human Lying Down	118
5.22	Human Only	118
5.23	Scooter Only	118
6.1	UWB hardware	121
6.2	flight control hardware	121
6.3	flight Control Software Implementation	122
6.4	localisation using GPS, UWB & ultrasonic	123
6.5	Class EF inverter circuit topology	123
6.6	Coils shape and size using CST (Christopher Kwan)	125

6.7	Horizontal displacement vs k	126
6.8	Induced Voltage vs k	126
6.9	Photograph of the experimental setup	127
6.10	IPT induced voltage vs relative position	127
7.1	WPW2019	132

Chapter 1

Introduction



Figure 1.1: AirPower (Apple Inc.)

Wireless power transfer (WPT) was first proposed by Nikola Tesla over a century ago, and since then a considerable amount of research has been conducted in this field [2–7]. It is common to classify WPT into two categories: far-field and near-field WPT. Far-field WPT applications typically uses radio frequency (RF) to transfer power and are commonly used for low-power

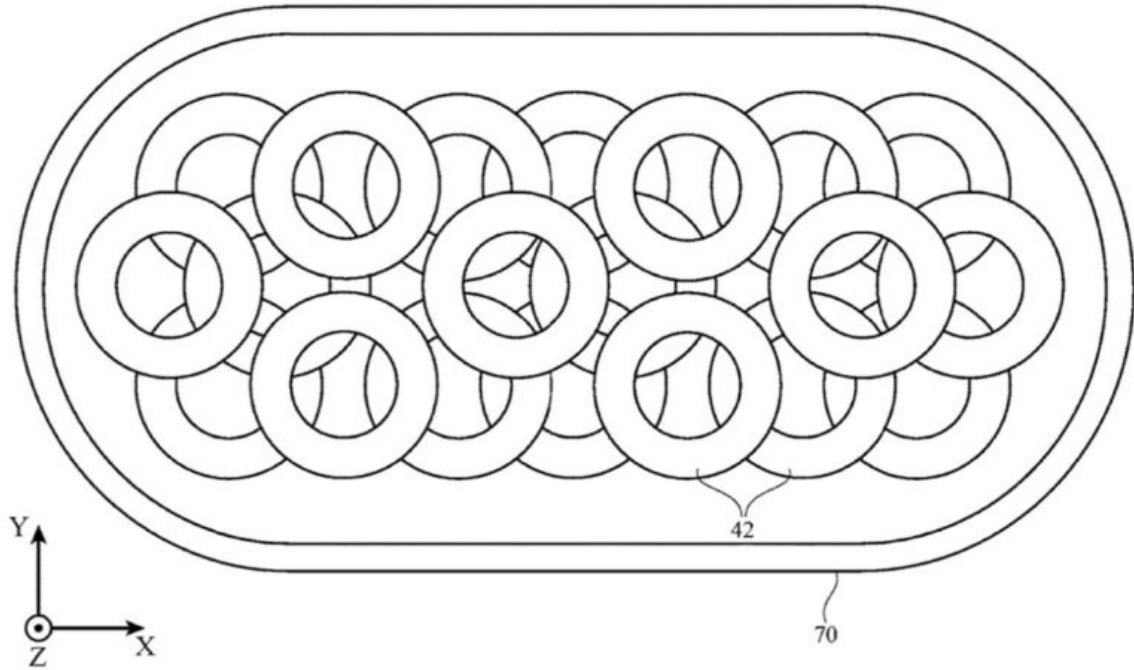


Figure 1.2: AirPower Coil Patent (Apple Inc.)

(micro- to Milli-watt) [8–12]. There are also applications using laser beams to transfer power over a long distance [13–15]. Near-field WPT, or nonradioactive WPT, on the other hand, focuses on shorter range, but higher power applications [16–19]. There are also some research focuses on capacitive and ultrasonic-based wireless charging methods [20–22] [23, 24].

While there are various means of transferring power wirelessly, the near-field inductive power transfer (IPT), has been the most widely used WPT solution. The Qi wireless charging standard (Qi Standard), for example, is an IPT-based wireless charging standard mainly developed for consumer electronics, e.g., mobile phones, smart watches, and electronic toothbrushes [25]. Although Qi is the most widely used wireless charging standard for portable devices, e.g., smart phones, this is not the case for many fields other than consumer electronics. Even within consumer electronics, the Qi-standard is not applied to every category. Laptops and tablets, for example, are not commonly delivered to customers with wireless charging capability. And outside the consumer electronics world, it is even rarer to see commercial applications of wireless charging. One of the reasons for that is the Qi-standard typically requires a tight alignment (usually within a few cm) between the charging pad and the device to be charged, as demonstrated in Fig. 3.4 and Fig. 3.3. Such requirement means that even a small movement of

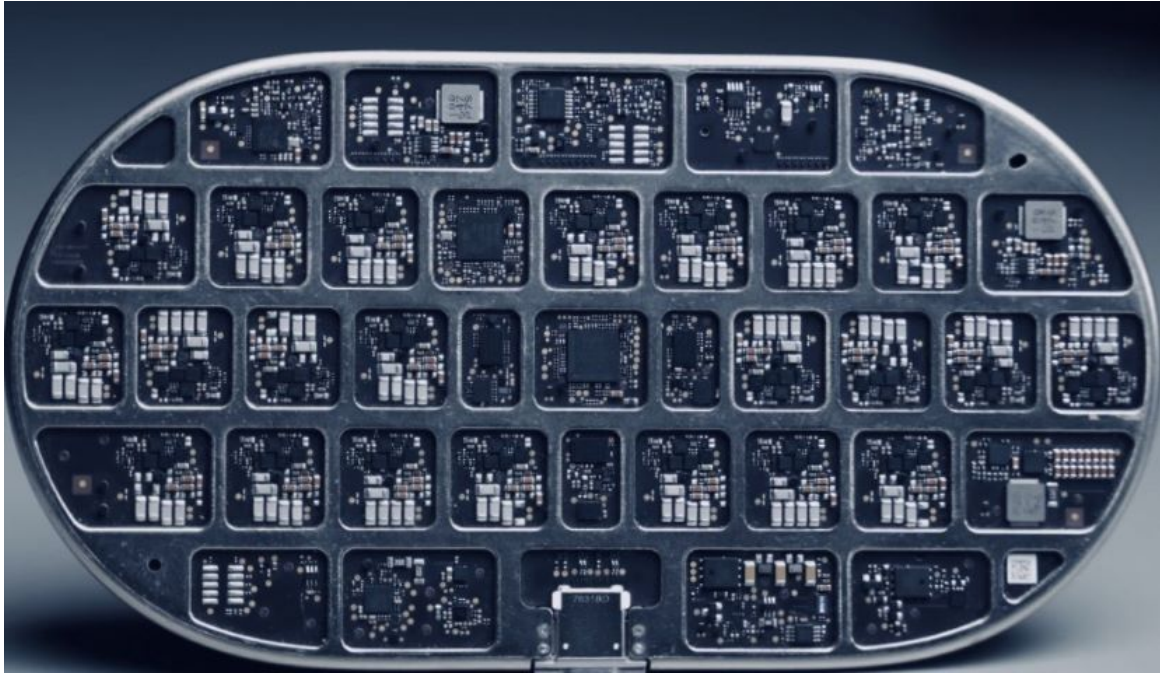


Figure 1.3: Inside of the AirPower prototype

the charging device could terminate the charging, which puts a constraint on many applications, e.g., laptops, e-scooters, drones and EVs etc..

Therefore, many research teams have been working on increasing the tolerance of misalignment of wireless charging. Multi-coil IPT systems, for example, are one way to increase the tolerance of misalignment. Such a technique has been proposed by various research teams world-wide [26–29]. Back in 2017, Apple Inc announced a wireless charger named AirPower that could charge multiple devices with a high tolerance to misalignment, as shown in Fig 1.1. The device was based on multi-coil technology, as shown in one of the patents filed by Apple in Fig. 1.2 [30]. The principle behind this idea is rather straightforward. By stacking multiple Qi-standard wireless charging coils together, it is possible to allow the device-to-be-charged always be placed on a coil and deliver power to it. Such a method could also allow multiple devices to be charged simultaneously. The disadvantages of this method, however, are also rather obvious. A multi-coil IPT system adds significant complexity compared to a single-coil one. The system has multiple resonant inductive resonators with close coupling to the adjacent resonators, which could make it difficult to tune each resonator to the same frequency. The system also needs an tracking system to locate the receive coil and turn on the correct transmit coil. The dense

stacking of coils also makes thermal management a challenging task. Finally, such a system could be more prone to inductive heating of foreign objects than a single-coil Qi charger due to the higher number of transmit coils. Perhaps this is one of the reasons that AirPower - with all exciting promises - was officially cancelled by Apple on 29th March 2019 [31]. In fact, there have been numerous reports about engineering challenges and overheating issues during the product's development [32]. Fig. 1.3 also shows what the inside of a claimed-to-be AirPower prototype looks like [33]. It can be seen how the increased number of coils adds complexity to the overall system.

Another approach to increase the tolerance of misalignment is by dynamically adjusting the position of the transmit coil to ensure a perfect alignment between the transmit coil and the receive coil, as proposed in [34]. Such a method is also showcased by Xiaomi. [33]. Fig .1.4 shows how this device functions. The device consists of a standard Qi-standard charger, two-axis motor and a tracking circuit board to locate the position of the device to be charged, and a circuit board that detects the position of the device to be charged and sends the location information to the motor controller, which then brings the coil to charge the device. When one device finishes charging, the motors then bring the charger to the next device that needs charging. More details about how such system works can be viewed at [33]. While this solution reduces the number of charging coils and electronics compared to the multi-coil solution, additional mechanical and localisation systems are required, which also increases the complexity, size, and fragileness of the overall system. Moreover, such solution shares the same charging power limit as the typical Qi-standard charger.

In summary, while both methods show some potential of increasing the range of wireless charging, they are essentially Qi-standard chargers with additional complexity, and therefore could share the same limitations as the Qi-standard charger e.g., the charging power. The additional complexity could also increase the size, cost, and possibly safety risks to the overall system.

Another approach of increasing the tolerance of misalignment is by increasing the operating frequency of the IPT system. Team in [35] for example, demonstrated a 10 W battery-less drone powered completely by a 13.56 MHz high frequency inductive power transfer (HF-IPT)

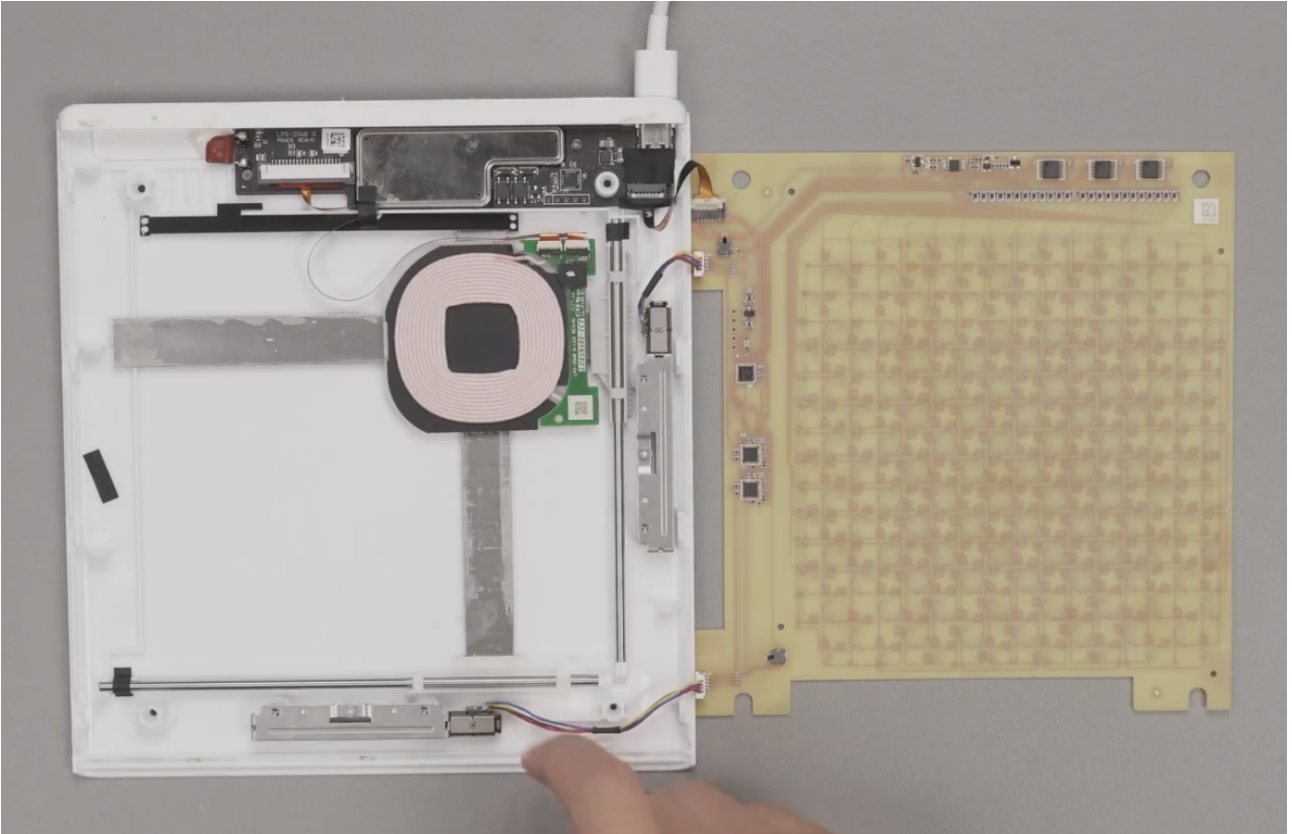


Figure 1.4: Inside of the Xiaomi Auto-tracking Wireless Charger Prototype

system with a charging range that is significantly larger than a Qi-standard wireless charger, as shown in Fig. 1.5 [36]. An 100 W 6.78MHz IPT system for e-scooters was also showcased in [37]. Another MHz IPT system that could charge a drone at 100W was presented in [38]. These applications have demonstrated that the misalignment tolerance of an IPT system could be increased with higher operating frequency and matched coil and inverter design. The Airfuel is another wireless charging standard that also focuses on high-frequency (specifically 6.78 MHz) inductive power transfer [39]. A more detailed description of high-frequency IPT systems will be included in the background section.

While these mentioned HF-IPT applications have showcased some advantages over the kHz or the Qi-standard wireless charging technology, there are still works needing to be done before it is readily available to the general public, and one major part of it is safety. For an IPT system, the safety considerations mainly fall into two categories, one being the electromagnetic exposure to humans/animals and the other being the inductive heating and interference of foreign objects. Like most electrical devices, an IPT system should be designed to keep its electro-

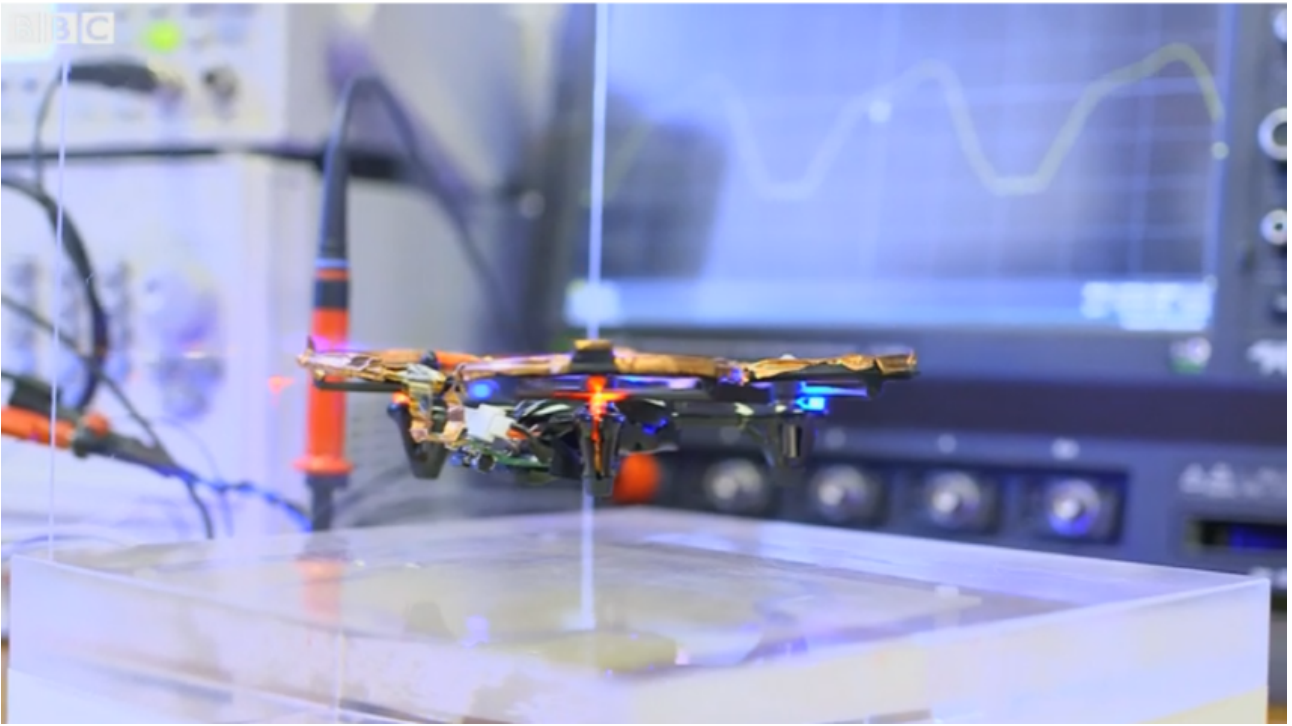


Figure 1.5: Batteryless Drone Powered Wirelessly (BBC)

magnetic exposure to be below the safe level for humans/animals. For near-field systems, the specific absorption rate (SAR) is widely used to evaluate the safety levels, e.g., the International Commission on Non-Ionising Radiation Protection guidelines (ICNIRP) [40]. More information about the EM exposure to living beings can be accessed in [41–44]. When an IPT system could not meet the safety guidelines, it should have a mechanism to detect if humans or animals are reaching the safety distance and pause the charging. Similarly, such a safety mechanism is also needed to detect objects that could be heated up or affect wireless charging when placed close to the IPT system. Therefore, the design and development of such safety systems is the main focus of this PhD thesis.

This thesis primarily focuses on safety system design and development for high-frequency (MHz) IPT systems, it starts with the fundamentals of IPT together with the safety analysis of some existing and potential wireless charging systems. This thesis also presents two end-to-end real-world applications of the HF-IPT system as the test bed for the FOD/LOD systems that explored in the following chapter. The proposed FOD/LOD will then be discussed in detail.

1.1 Background

1.1.1 Inductive Power Transfer

Before discussing the safety systems of an IPT system, it would be useful to start with some of the fundamentals of an IPT system. An IPT system can be described by two key equations: Ampere's law and Faraday's law. Ampere's law states that magnetic fields could be generated by the current in a conductor (Equ. 1.1), and Faraday's law states that voltage can be induced from magnetic fields (Equ. 1.2). By combining them together, one can generate a magnetic field from one conductor and induce voltage in another conductor without a physical connection between them, hence achieving wireless power transfer. By applying these principles, Nikola Tesla demonstrated reportedly the first real-world application of wireless power transfer back in 1905 [2, 3].

$$\sum \mathbf{B}\Delta\mathbf{L} = \mu_0\mathbf{I} \quad (1.1)$$

$$\oint_{\partial\Sigma} \mathbf{E} \cdot d\mathbf{l} = -\frac{d}{dt} \iint_{\Sigma} \mathbf{B} \cdot d\mathbf{S} \quad (1.2)$$

One of the most important measures of an IPT system is its efficiency. From the two equations, it can be observed that the induced voltage on the receive side is proportional to the magnetic field generated by the transmit coil. With a fixed load on the receive side, a stronger magnetic field means higher power on the received side. If the transmit side has a fixed current flow and is placed at a fixed position, a closer relative position of both coils would result in a stronger field received on the receive side and therefore more power is delivered, which results in a higher efficiency of the IPT system. To better characterise this, it is common to use the coupling factor, or k , to represent the relative positioning between the transmit and receive coils of a WPT system. The coupling factor k of two inductors L_1 and L_2 is defined as Equ.1.3, while M is the mutual inductance between the two inductors. k is a number between 0 and 1, a larger k

usually means the two coils are tightly coupled, and vice versa. Certain materials, e.g., ferrite, could also be used to increase the coupling factor by changing the direction of the magnetic fields [19].

$$k = \frac{M}{\sqrt{L_1 \cdot L_2}} \quad (1.3)$$

Apart from the relative position of the transmit and receive coils, another factor that could affect the efficiency of an IPT system is the coil. In practice, both the transmit and receive coils are not perfect conductors, which means they both have losses due to the resistance of the coil, and the resistance of the coil also increases with frequency due to the skin effect [45,46]. If not designed carefully, this could have a significant impact on the efficiency of an IPT system. Q-factor is therefore used to characterise the quality of the coil. Equ. 1.4 is the definition of Q-factor, Where Q_{L_1} and Q_{L_2} are the Q-factors of the transmit and receive coils. Q-factor is defined as Equ. 1.4. L and R are the coil's inductance and resistance, respectively. A higher Q-factor means lower energy loss due to the coil.

$$Q = \frac{\omega L}{R} \quad (1.4)$$

$$\eta_{link} = \frac{k^2 Q_{L_1} Q_{L_2}}{2 + k^2 Q_{L_1} Q_{L_2} + 2\sqrt{1 + Q_{L_2}^2 + k^2 Q_{L_1} Q_{L_2}}} \quad (1.5)$$

Both the coupling factor k and quality factor Q are useful parameters to the efficiency of an IPT system. In fact, the efficiency of an IPT system (coil-to-coil) is completely dominated by k and Q , as concluded in Equ. 1.5 by Robert Puer in 'Inductive Powering: Basic Theory and Application to Biomedical Systems' [7]. It can be seen from Fig. 1.6 that a lower k would cause the efficiency of the IPT system to decrease. However, a higher Q of both transmit and receive coils could compensate such loss.

One approach to increase Q of a coil is to increase the operation frequency of the WPT system,

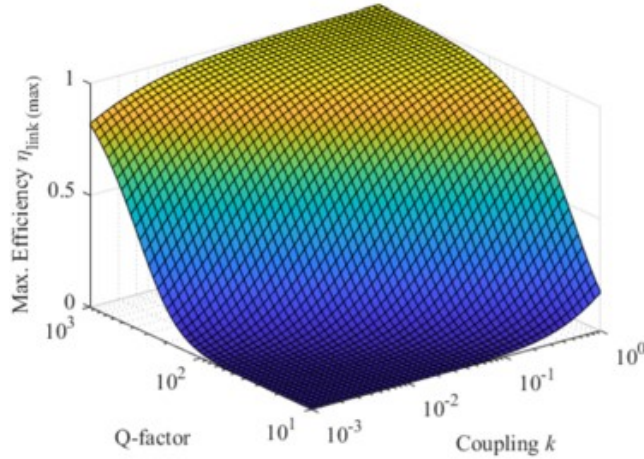


Figure 1.6: The relationship between link efficiency, coupling factor and Q-factor [1]

as indicated in Equ. 1.4. However, it is important to note that a higher operating frequency does not always mean a higher Q-factor. Due to the skin effect, the resistance of a coil would also increase as frequency increases [45]. In addition, depends on the design of the coil, as the frequency increases, the parasitic capacitance of a coil could resonant with the coil (known as self-resonance), and therefore the coil's impedance would increase, thus reducing the Q-factor. For coils that integrated with magnetic materials to increase the coupling, it is important to note that the specifications of such material could also limit a coil's Q-factor. In [47], a datasheet of some common ferrite materials from TDK are presented, it can be noticed that above a certain frequency, the loss in ferrite starts to increase, which could significantly reduce the Q-factor of a coil that is closely coupled to this ferrite material. Fig. 1.7 shows the Q-factor of a typical Qi coil with ferrite material. It can be seen that though the Q-factor increases from 5 to 30 as the frequency goes from 10 kHz to 500 kHz, it starts to decrease after that. Overall, with a careful consideration of these factors, it is possible to design a coil with a much higher Q-factor at higher frequencies [48]. And because of this, many research teams have been focusing on the design and development of high-frequency IPT (HF-IPT) systems, usually in multi-MHz frequency range [49] [50] [51] [52].

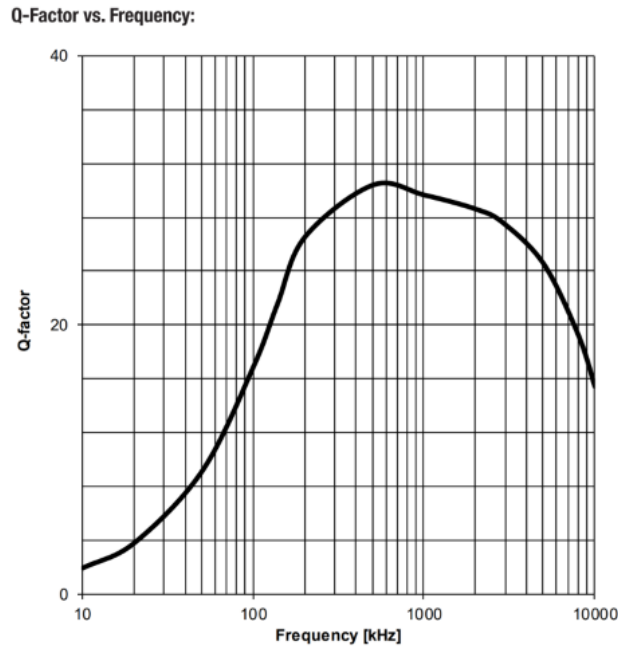


Figure 1.7: Q-factor of a typical Qi-standard coil

1.1.2 High-frequency IPT systems

As previously discussed, high-frequency IPT systems could achieve higher Q coils and therefore a better tolerance to lower coupling between the coils. However, the design of a HF-IPT system has a higher complexity compared to LF-IPT systems. On the inverter side, the increase of the operating frequency would also increase the switching loss in the switching device (typically MOSFET), which limits the number of suitable devices for the HF-IPT design. The traditional inverter topologies may also need to be revisited to further optimise the higher frequency design. Similarly, on the receive side, the traditional rectification design may also not be capable of handling the high frequency operation. The loss in the rectifier diode could be higher than expected due to the capacitance of the diode. Therefore, the receive side also needs to be considered carefully to cope with the higher operation frequency.

The Inverter

On the transmit side of an IPT system, an inverter circuit is used to convert a DC source to an AC current in the transmit coil. Typically, an inverter circuit works by switching on and off transistors in a circuit to change the direction of current flow. The switching loss of

a transistor occurs when the transistor is switched on/off with a voltage across the device, as the voltage across the device cannot change instantly, current could flow before the voltage reaches zero, hence power is dissipated in the transistor. The switching loss of a transistor is proportional to the switching frequency as the number of switches increases for a given period at a higher frequency [53]. As a result, to design a HF-IPT system, the switching loss of the transistor must be considered carefully. There are inverter circuit topologies which implement “soft-switching” techniques to reduce the switching loss of the switching device even at a high switching frequency [53]. However, most soft-switching power converter was designed with an optimal load, that is, the soft switching only occurs at a specific loading condition. Once the loading status changes, the power converter could see a significant efficiency drop. This is undesired for an IPT application as the loading condition varies with the coupling of the Tx and Rx coils [51]. [54] introduced a load-independent inverter design that allows an inverter to operate in soft-switching mode regardless of the (resistive) loading condition. Fig. 1.8 shows a circuit of the load-independent Class EF inverter [52].

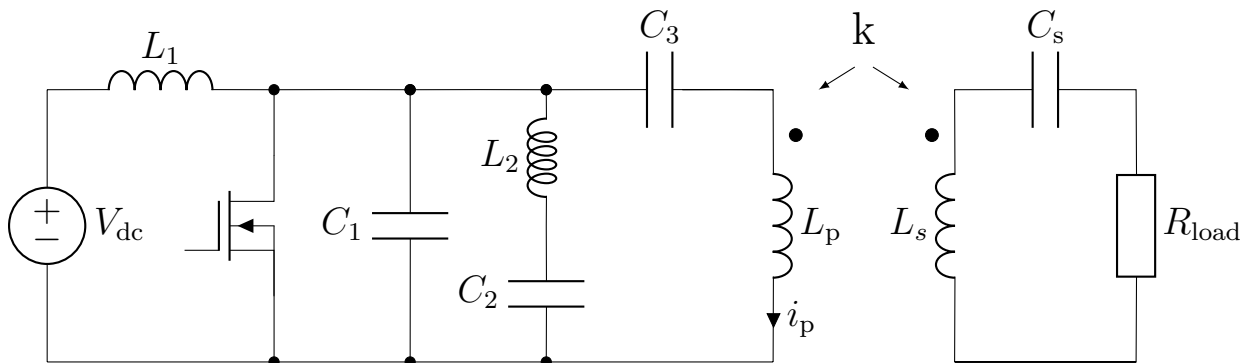


Figure 1.8: Class EF inverter circuit topology

The Switching Device

Typically for low-power electronics, a MOSFET is used as the main switching device, which satisfies most applications. However, for high current, high voltage, and high frequency (MHz) applications, MOSFET might not be the most suitable choice. The Wide-band-gap device, on the other hand, is designed for such use scenarios. Gallium nitride (GaN), for example, can typically handle a drain-source voltage of 650V, and has a very low on-resistance and gate

charge, the switching frequency of a GaN device can easily reach 40 MHz [55]. Silicon Carbide, or SiC, is also a wide-band-gap device, and it can handle 1200V drain-source voltage, which is used in some electric vehicle motor drivers [56]. A comparison of MOSFET, SiC, and GaN is summarised in Fig. 1.9. The rising popularity of wide-band-gap is helping to reduce the difficulty of increasing the switching frequency.

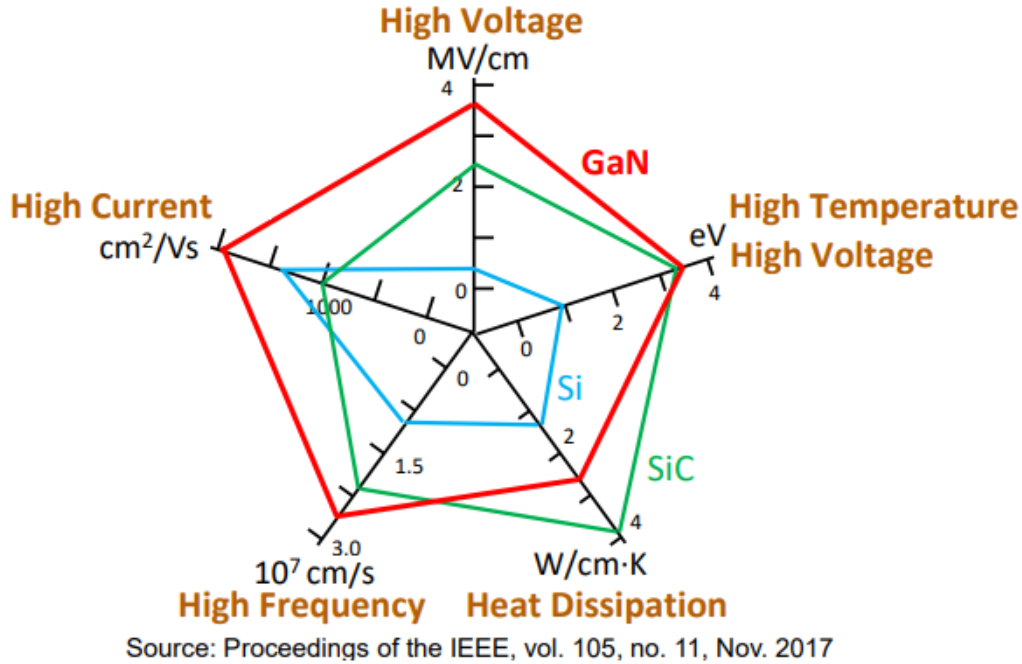


Figure 1.9: A comparison of wide-band-gap devices

The Receiver

The receive side of an IPT system is shown on the right side in Fig. 1.8. k indicates the coupling between the two coils and R_{load} is the load on the receive side. The load on the secondary side of the IPT system, can be modelled as a reflected impedance on the transmitter side, according to the study in [57, 58], where it shows that when the receive side is “tuned”, i.e. L_s and C_s resonant at the operating frequency of the inverter circuit, and the load is pure resistive, the reflected impedance becomes pure resistance. Reference [54] also suggests that circuit in Fig. 1.10 could be configured to achieve load-independent operation. This means the soft-switching or zero-voltage switching (ZVS) could be maintained regardless of the reflected resistance. A tuned receiver with a resistive load could therefore, operate over a range of

coupling values, without affecting the operation of the inverter, therefore achieving a wider range of wireless charging.

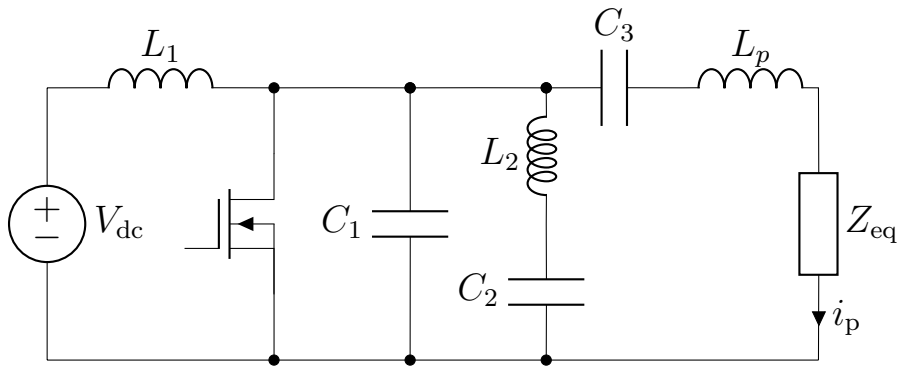


Figure 1.10: Class EF inverter circuit with equivalent load

The Rectifier

A rectifier is typically connected to the receive side of an IPT system to convert the AC back to DC for most applications. Passive rectifiers (half-bridge, full-bridge) are widely used thanks to their simple design and low cost. However, for applications with higher current, passive rectifiers may not be ideal to use due to higher loss in the diodes [59]. To increase the efficiency of rectification, many research teams have shifted to active rectification studies. [60] showcased a hybrid class E rectifier design that arrived 95% efficiency on the receive end.

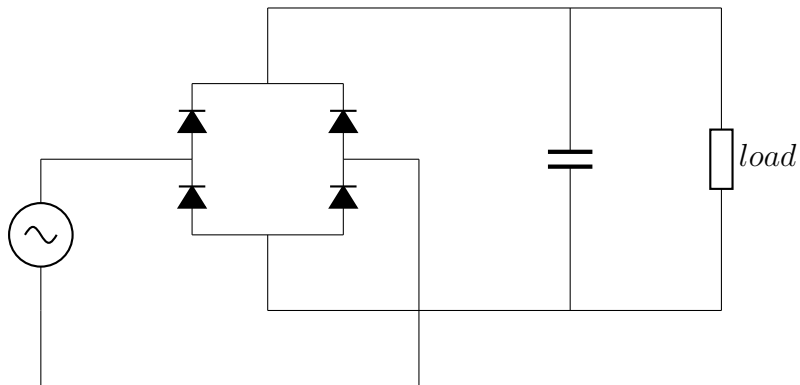


Figure 1.11: A passive rectifier (full wave rectifier)

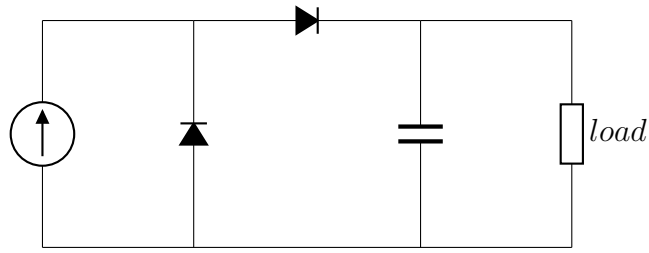


Figure 1.12: A passive rectifier (Class D Half Wave rectifier)

1.1.3 Safety of IPT systems

The safety of wireless power systems is a key consideration in their design and use, which is regulated by institutions and commissions, e.g., IEEE and ICNIRP, and is an often asked question by users of this technology. It is also worth mentioning that the traditional way of delivering power via electric wires also has safety risks. According to [61], electrical hazards cause more than 300 deaths and 4000 injuries each year among the U.S. workforce. It can be argued that the elimination of wires reduces the chance of human/animals' contact with exposed live wires and therefore lowers the chance of electric shock. Moreover, in many scenarios, e.g., under water charging or implanted device charging ranges from difficult to impossible.

The most common concern for safety of near and far-field wireless power systems is the electromagnetic exposure to humans and animals. As for inductive power transfer, the inductive heating of objects nearby should also be considered carefully. Moreover, the IPT system should also protect itself from damage, e.g., overheating due to external interference. These three different types of safety considerations are discussed in more detail in this section.

Electromagnetic Exposure

Since energy can be delivered in air using a wireless power transfer system, it seems natural to worry that if this kind of “energy” that exists through the air could cause harm to humans or animals. Before going deep into this, it is worth mentioning that humans and animals are exposed to many forms of radiation, e.g., light. While some of them have harmful effects on living organisms, others do not. To better distinguish harmful and nonharmful radiation, they are often categorised into ionising and non-ionising radiation depending on the energy

levels they carry. Ionising radiation carries energy more than 10 eV, which is enough to ionise atoms and molecules and break chemical bonds, which is harmful to living organisms [62]. Examples of ionising radiation are X-rays, gamma rays, etc. Non-ionising radiations, on the other hand, do not carry enough energy to “ionise” atoms or molecules of living organisms. In fact, the World Health organisation (WHO) has concluded that “To date, no adverse health effects from low-level, long-term exposure to radio-frequency or power frequency fields have been confirmed” [63]. However, even though non-ionising radiation does not cause direct harm to living organisms, if the energy level is high enough, they cause still cause injury due to excessive heating or nerve stimulation. It is, therefore, important to know the limit level of the acceptable non-ionising radiation of the IPT system. The International Commission on Non-ionising Radiation Protection, often referred as ICNIRP, is an independent organisation that specifically focuses on the safety limitations of non-ionising radiations [64]. The guideline provides some reference levels of maximum electrical field and magnetic field should be exposed to humans. Tbl. 1.1, for example, shows the ICNIRP 2010 E and H-field reference levels between 3 kHz and 10 MHz for the general public and occupational.

Table 1.1: ICNIRP 2010 E- and H-field Reference Level (3 kHz to 10 MHz)

	E-field Strength (V/m)	H-field Strength (A/m)
General Public	83	21
Occupational	170	80

The reference levels of E- and H-field provided by ICNIRP, however, are highly conservative, exceeding the reference levels does not necessarily mean the system is definitely unsafe [65]. In fact, a home induction hob could easily exceed the H-field reference level. Fig. 1.13 shows a typical home induction hob with four cooking zones, each zone is occupied with a IH compatible cooker and filled with water for testing purposes. The four cooking zones are turned up for maximum power. H-field is then measured in around this setup using a NARDA EHP200 probe, as shown in Fig. 1.13.

Fig. 1.14 shows the measurement result when the probe is placed approximately 15 cm from the middle point of the two cooking zones in front of the hob. It can be seen that the maximum magnetic field occurred at the fundamental frequency of approximately 19.5 kHz. The max-



Figure 1.13: Induction Hob H-field Measurement Setup

imum magnetic field strength is 30.69 A/m, which is roughly 50% higher than the reference level, and this value goes higher when placed closer to the hob. Moreover, the distance between the probe and the induction hob can be easily reached by the person who uses the hob during cooking. However, this does not necessarily mean that it is dangerous to use the induction hob, it simply means that further measurements or simulations are needed to better evaluate the safety of such an appliance.

This is when the Specific Absorption Rate (SAR, watts per kg) becomes useful. As discussed before that for non-ionising radiation the safety concern is more on the heating effect rather than the break of chemical bonds and therefore the magnetic and electric field strength may not be the best indicator of the heating effect, as shown in the experiment above. The SAR, on the other hand, specifically indicates the power absorbed by living organisms, which is a more effective indicator about how much energy is delivered over a specific period. Tbl. 1.2 shows

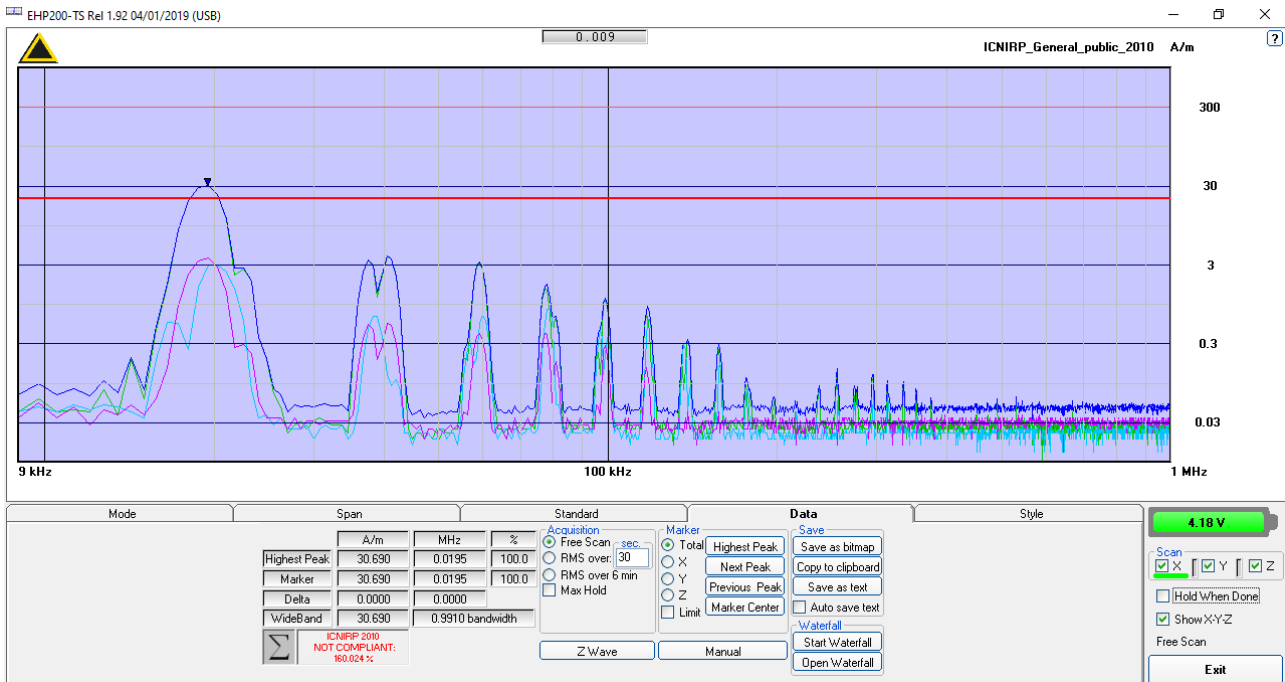


Figure 1.14: Induction Hob H-field Measurement Result

the ICNIRP 2010 SAR basic restrictions for frequencies from 100 kHz to 6 GHz (average over 6 minutes). There are different limit levels for the general public and occupational, with the limit level for the general public higher than that for occupational. The limit is also different for the whole body and for local head/torso and limbs.

Table 1.2: ICNIRP 2010 Basic Restrictions (100 kHz to 6 GHz)

Exposure Scenarios	Whole-body average	Local head/torso	Local limb
General Public	0.08 W/kg	2 W/kg	4 W/kg
Occupational	0.4 W/kg	10 W/kg	20 W/kg

An IPT system is a similar system to an induction hob, and, as discussed, by measuring the E- or H-field, may not be an appropriate indicator about its safety. The SAR can be used instead to see if a IPT system would exceed the safety limits if a human is next to the system, and what's the minimum distance before this happen. While it is difficult to measure SAR inside a living organism, one can use EM simulation software with human body models to evaluate the safety of an IPT system. Reference [37], for example, presented a 100W IPT system for electric scooters, with a human body SAR simulation together with the designed IPT system. From the simulation results (Fig. 1.15), it can be seen that the SAR, when a person is lying down 5 cm next to the IPT system, is at maximum 0.0174 W/kg, which is significantly less than the

safety threshold of 4 W/kg for limbs for the general public. When the simulated human foot is placed 5cm next to the coil, the SAR is 0.00646, which is again, significantly below the limit for the general public. Both SAR values are also below the occupational limits.

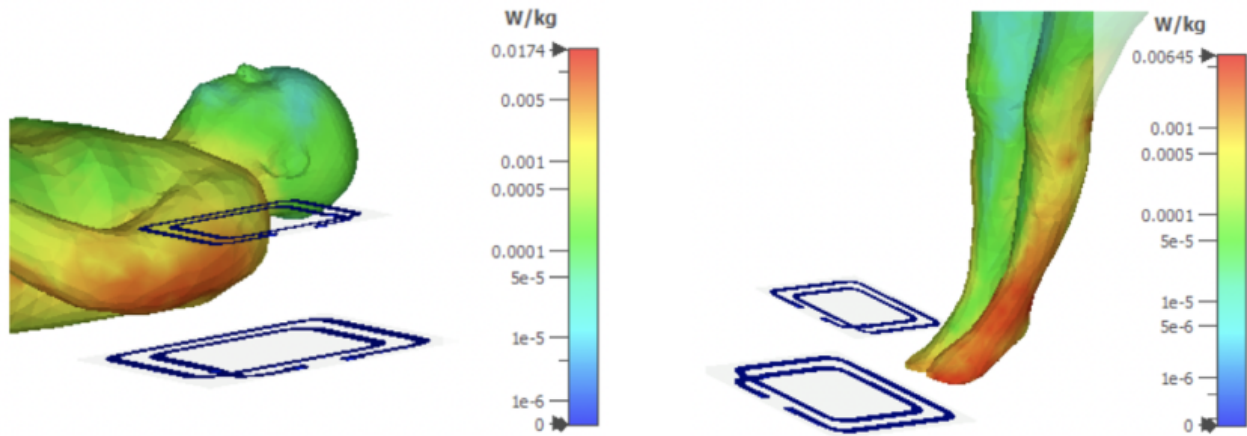


Figure 1.15: SAR human body simulation

In this particular example, the IPT system can claim to be safe to use in terms of SAR limit, with a 5 cm safety distance. However, this may not always be the case, when the power level increases or when the operation frequency changes, the safety distance could also change. And when the safety distance becomes too large to be practical, an additional safety mechanism may be needed to ensure that the SAR does not exceed the limit during the normal IPT operation.

Similar to SAR, the internal E-field should be measured to determine the safety limit of nerve or muscle tissue stimulation if the E-field measure is higher than the reference level in Tbl. 1.1. According to ICNIRP 2010, the internal E-field limit for the general public between 3 kHz and 10 MHz is $1.35 \times 10^{-4} \times f$ (V/m), where f is the frequency of the IPT system in Hz. Since the internal E-field is difficult to measure, the human model EM simulation can be used instead. Fig. 1.16 shows both SAR and E-field simulation results of a hand resting on a 5W 6.78 MHz mobilephone wireless charger [66]. The values are normalised to the most stringent basic restriction levels (ICNIRP internal E-field and FCC SAR). It can be seen that both the internal E-field and SAR were well below the basic restriction levels.

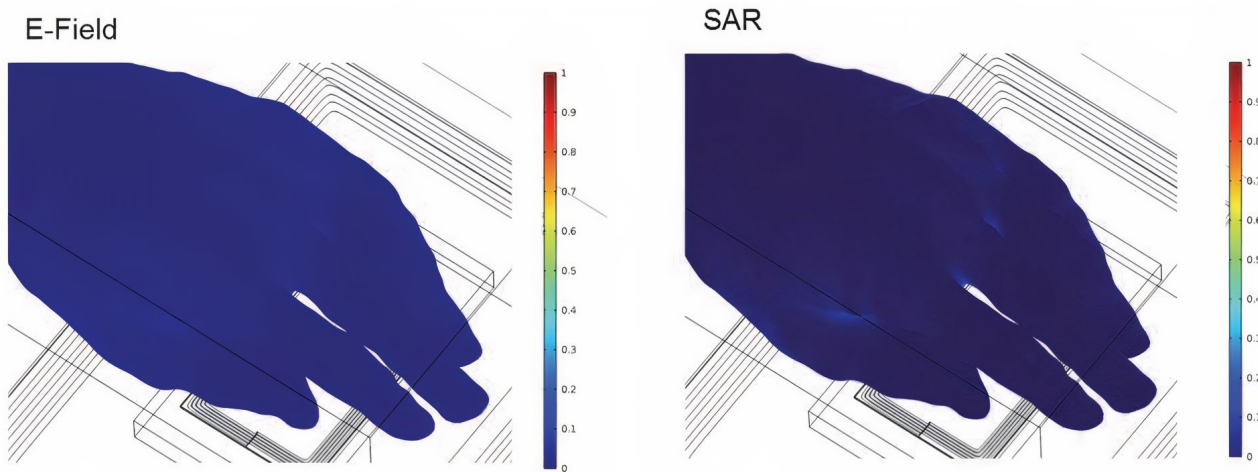


Figure 1.16: SAR and internal E-field Simulation simulation

Inductive Heating of Foreign Objects

In addition to the EM exposures, another safety concern regarding IPT systems is the inductive heating of objects present in the magnetic field. While the magnetic field could induce voltage on the receive coil, it could also induce voltage on other objects and cause current flow, such current is also called eddy current [46]. This current could therefore cause temperature rise of the object due to Joule heating. Metal objects, due to their lower resistance compared to typical nonmetallic objects, can be easier to heat up. In fact, the inductive hob shown in Fig. 1.13 heat up cooking pan because of this effect. A typical Qi-standard mobile phone IPT charger, although has significantly less power compared to an induction hob, is still capable of rising the temperature of small objects, e.g., keys or coins. Fig. 1.18 shows an experiment when a coin is placed on top of a typical Qi-standard mobile phone charger for 10 minutes. It can be seen that the temperature of the coin rose up to 100 degrees, which could already cause injury to anyone touching it. Moreover, when the power and charging distance increase, the safety hazard also increases. Therefore, such safety concern is valid and must be thoroughly assessed when designing a IPT system.

It is also worth noting that the inductive heating effect depends on the frequency of the changing magnetic field, since the impedance of metal objects increases due to the skin effect [46]. Skin effect is the effect that electrons tend to flow on the surface of the conductor as the frequency



Figure 1.17: A coin heating up on a Qi charger

increases. As a result, at higher frequency, the eddy current reduces, which means less joule heating.

The HF-IPT systems - in particular - MHz-IPT systems, show significantly less inductive heating of common metal objects due to the skin effect. Experiment in Fig. 1.18 shows a coin placed on a 13.56 MHz IPT system for 10 minutes. A Flir one thermal camera is used to monitor the temperature and no obvious temperature increase on the coin.

Even though HF-IPT systems tend to show less object heating on metal objects, this does not mean that no object heating would occur. This depends on the structure and material of the objects, some objects could still have a low impedance around the operating frequency of the IPT system. From some experiments done in the wireless power lab, it was observed that a compact disc (CD) happens to be able to non-negligibly load a 13.56 MHz IPT system. Fig. 1.19 shows the temperature of the CD when placed on top of a HF IPT system for 3 minutes. Although it only rose to 45.2 degrees in this particular case, it could go higher if placed on a higher current IPT system. There could also be more objects that can draw power from a HF IPT system, and this should also be considered carefully.



Figure 1.18: A coin placed on a 13.56 MHz IPT system

External Interference to the IPT System

In addition to foreign object heating, another safety concern of an IPT system is the possible damage to the IPT system itself due to external interference, e.g., foreign objects. This is dependent upon the design of the IPT system, some designs are more robust than the others. The load-independent Class EF design from [54], for example, is capable of maintaining optimum operation (low loss in the inverter) regardless of any resistive load. However, the inverter could still shift from optimum operation with a reactive load coupled to it (Fig.?? shows how different types of load could affect a class EF load-independent IPT system). This “detuning” of an IPT system could easily happen with objects as simple as a piece of metal sheet placed on top of the transmit coil. Therefore, if not considered carefully, such a scenario could cause damage to the inverter or even cause a fire due to excessive heat.



Figure 1.19: Induction Heating of a CD

1.1.4 Research Areas and Thesis Outline

This thesis exclusively focuses on high-frequency (MHz) IPT systems. All IPT applications, FOD/LOD systems discussed in this thesis are based on 6.78/13.56 MHz IPT systems. Chapter 1 of this thesis introduces the motivation and aim of this PhD research. Chapter 2 demonstrates two real-world applications of HF-IPT systems and the two applications are also used as benchmarks for the FOD system to be designed in the following chapters. Chapter 3 presents some analysis of FOD/LOD methods and, based on this analysis, two methods were chosen to be explored in detail. Chapter 4 discusses the first FOD/LOD method that based on the reflection of impedance from the Rx side of the IPT system with some experimental results. Chapter 5 shows a completely different approach of detecting and classifying live and foreign objects using a mmWave radar system. For each of the FOD/LOD methods, approaches to implement them on low-cost hardware are also discussed. Finally, an IPT-based localisation technique was also introduced as an alternative safety measure for autonomous wireless charging applications.

Chapter 2

End-to-end HF-IPT Systems

Before the discussion of the safety system design and development, it would be sensible to start with some actual applications of HF-IPT systems, as different applications may have different safety requirements. A real-world IPT application also provides real-world limitations for the safety systems to be designed. This could be the size, weight, dust, cost, etc.. This chapter includes system-level design and development of two end-to-end applications of HF-IPT. One is a 100 W wireless charger for commercial drones, and another is a sensor network wireless charging system. The two real-world HF-IPT applications also provide a good test bed for FOD/LOD systems discussed in the following chapter. The author's contribution in this chapter includes the implementation of the load-independent IPT system on a commercial quadcopter drone, which is a continued work from a previous research effort that demonstrated the capability of the load-independent inverter design based on a small toy drone [67]. The author has successfully developed and demonstrated the drone being able to land and recharge wirelessly on an autonomous surface vessel, with a wide tolerance of misalignment. This work was also reported in [68] and published [38]. Another contribution from the author in this chapter is the design and development of an integrated IPT receiver and a battery management system. Such an integrated system was designed to power various sensors with a battery for a long period of time and can be recharged quickly (from 20% to 80% in half an hour) with an IPT-equipped drone. The designed system can also send useful information, e.g., battery state

of charge, IPT receive side voltage, etc.. to the charging drone via a UWB communication link.

2.1 Design and Development of a 100 W Wireless UAV Charger

Rotary-wing unmanned aerial vehicles (UAVS) are used in a variety of monitoring, search-and-rescue, and surveillance operations [69, 70]. These drones are being equipped with an increasing number of features such as video recording, GPS tracking, etc. Many of the added features facilitate the autonomous operation of drones, reducing direct human intervention and interaction. With the recent increasing interest in space exploration on Mars, alternative power delivery solutions can enable a broad range of possibilities concerning, among others, longevity and longer reach in unmanned exploration missions. Numerous robots have been sent to Mars since 1971 [71], and with gradual advancements in robotics engineering since then, robot visitors have been providing key data about the Red Planet. The Zhurong rover, as part of the Tianwen-1 mission that landed on Mars in 2020, for example, can take high-resolution photographs with a remote electronic camera [72]. The MARS 2020 mission by NASA not only sent a rover, but also a helicopter robot (Fig. 2.1) for aerial exploration of the planet [73].

These state-of-the-art robots also come with limitations. For example, the Ingenuity helicopter only operates every two weeks to make sure its battery is charged to an acceptable degree [74], since it is charged by its small on-board solar panels.

The means for charging a helicopter, as such, from an external charging pad can be comprised of a typical plug-in charger with a robotic arm; however, in such harsh environments, connectors would not be preferred since they could fail in the long run due to the presence of dust, and wear and tear. Wireless charging could also be employed, eliminating many of these issues while still maintaining the crucial lightweight features. An off-the-shelf solution, such as a Qi-standard wireless charger, would require ferrite-based coils (which are heavy) and a precise alignment between the transmitter and receiver to deliver enough power efficiently, which is likely to lead



Figure 2.1: The Ingenuity helicopter

to requiring a mechanical system to align the coils to optimise wireless charging, as showcased in [75]. Therefore, alternatively, HF-IPT systems, which allow for much higher tolerance to misalignment [76, 77] and light weight could pose an interesting solution. In [78], a MHz inductive power transfer (IPT) system was developed to power a small drone with its battery removed, where the benefits of operating an IPT system in the multi-MHz frequency range using lightweight ferrite-less copper coils and load-independent soft-switching power converters (e.g., [54]) with wide-bandgap semiconductor devices were highlighted.

This work presents a wireless charging solution for the DJI Matrice 100, a development drone platform that can be used in a wide range of applications and has a more practical payload of 1 kg (Fig. 2.2). This system has been designed to overcome several technical challenges, such as power electronics to cope with a highly variable coupling factor due to the limited landing precision of the drone and a shielding method to eliminate the effects of the transmit-side inverter detuning when placed in different electromagnetic environments. As a result, the DJI Matrice 100 drone can be charged at a rate of 100 W over a distance of 14 cm with up to 25 cm of misalignment tolerance.



Figure 2.2: A wirelessly charged DJI M100 drone

2.1.1 System Design

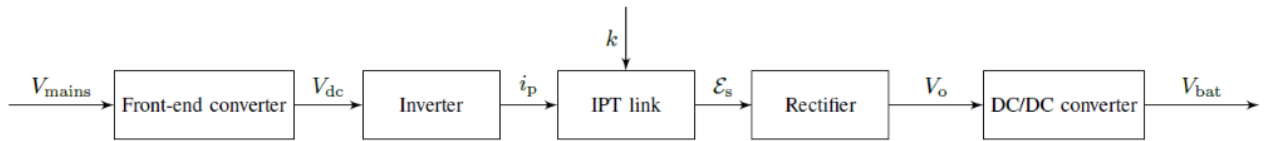


Figure 2.3: High-level system block diagram of IPT system

The drone selected for this work is the DJI Matrice 100. It is supplied with a 22.2 V, 4500 mA h rechargeable LiPo battery (model number TB47D). As the battery charger (model number A14-100P1A) has a maximum power output of 100 W, the wireless power transfer system will be designed to charge the battery at the same rate.

Fig. 2.3 shows a block diagram of the drone wireless charging system. The ‘Mains-rectifier’ and ‘PFC / DC-DC converter’ blocks refer to the power conversion from the ac mains to a dc voltage. The ‘Inverter’ block comprises the load-independent Class EF inverter used to drive the transmit coil with a high frequency current to generate an ac magnetic field. The ‘IPT-link’ block represents the power transferred from the transmit coil inside an enclosure on the ground to the receive coil mounted on the drone through the inductive link, where coupling k is a

variable. In terms of receive electronics on the drone, the ‘IPT rectifier’ block is a full-wave current-driven Class D rectifier and the ‘dc-dc converter’ block consists of a buck converter with a wide input voltage range to cope with variable coupling and an output voltage level suitable for charging the on-board drone battery.

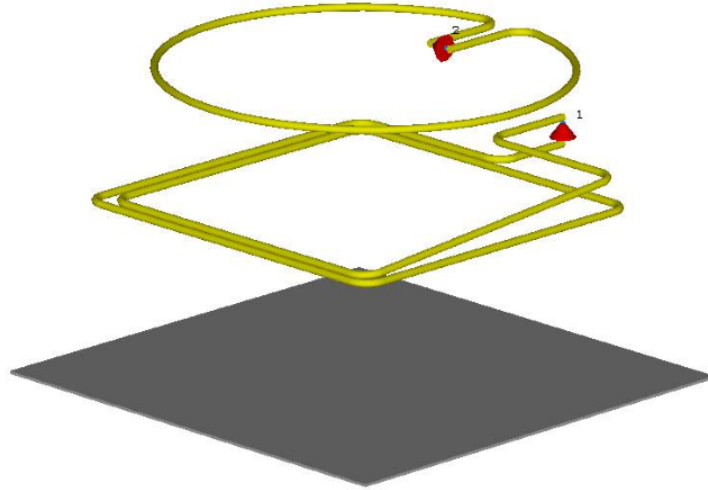


Figure 2.4: Coil and shielding shape and size

Coils, IPT link and Shielding

The transmit coil is a 2-turn square coil made of 8 mm copper pipe, with an inner and outer length of 350 mm and 400 mm, respectively. The receive coil on the drone is a single-turn circular coil (also made of 8 mm copper pipe) with a diameter of 400 mm. The vertical distance between the transmit coil and the receive coil is 14 cm. As there is a one-metre diameter circular landing pad on top of the transmit coil, the maximum lateral misalignment between the receive coil and the transmit coil is 25 cm.

Electromagnetic simulations in CST Microwave Studio were performed to derive the coil and link properties. The receiver coil has a simulated inductance of 1.13 μH and a Q factor of 1143.

To improve the robustness of the wireless charging system, an aluminium sheet was placed 18 cm underneath the transmit coil. This sheet acts as a form of shielding for magnetic fields, so that system tuning and performance is immune to variations in the conductivity and permeability of the surface on which the charging pad is placed. The overall configuration is shown in Fig. 2.4.

Table 2.1: Link parameters for 100 W at minimum coupling with optimal load

Parameter	Value
k	5.1 %
η_{link}	97 %
I_1	5.45 A
I_2	8.46 A
C_S	489 pF
R_L	2.79 Ω
R_{reff}	6.83 Ω

In the presence of the aluminium shield, the transmitting coil's inductance and Q factor are 3.63 μH and 1487, respectively. The coupling factor is 16.7% when perfectly aligned (drone placed on the center of the landing pad) and 5.1% at the maximum lateral misalignment (drone placed on the edge of the landing pad) of 25 cm. Such a large change of coupling allows a wide range of operation, which is difficult to achieve or even impossible with a Qi-standard IPT system. The transmit coil and the aluminium shield are shown in Fig. 2.6.

Using the coils' impedance and the coupling factor at maximum lateral misalignment (i.e., minimum coupling) in the presence of the aluminium shield and assuming series tuning at the receive side, the link parameters corresponding to 100 W received power when the optimal load is used for maximising the link efficiency are given in Tbl. 2.1 (where k is the coupling factor, η_{link} is the link efficiency, I_1 and I_2 are the primary and secondary coil current amplitudes, C_S is the secondary series tuning capacitance, R_L is the optimal load resistance and R_{reff} is reflected resistance seen at the transmit side).

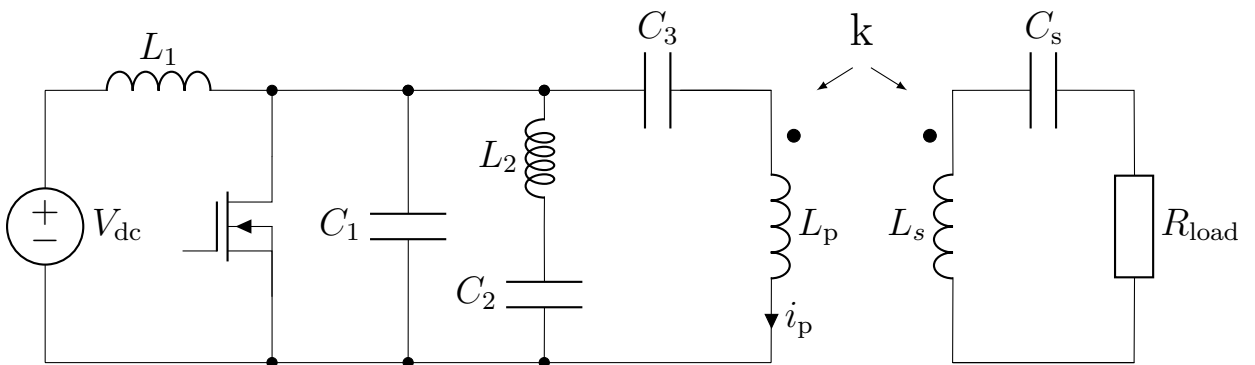


Figure 2.5: Class EF inverter circuit topology

Table 2.2: Component values of load-independent Class EF inverter

Parameter	Value
V_{dc}	100 V
C_1	433.7 pF
C_2	400 pF
C_3	190.48 pF
L_1	80 μ H
L_2	460 nH
L_p	3.33 μ H

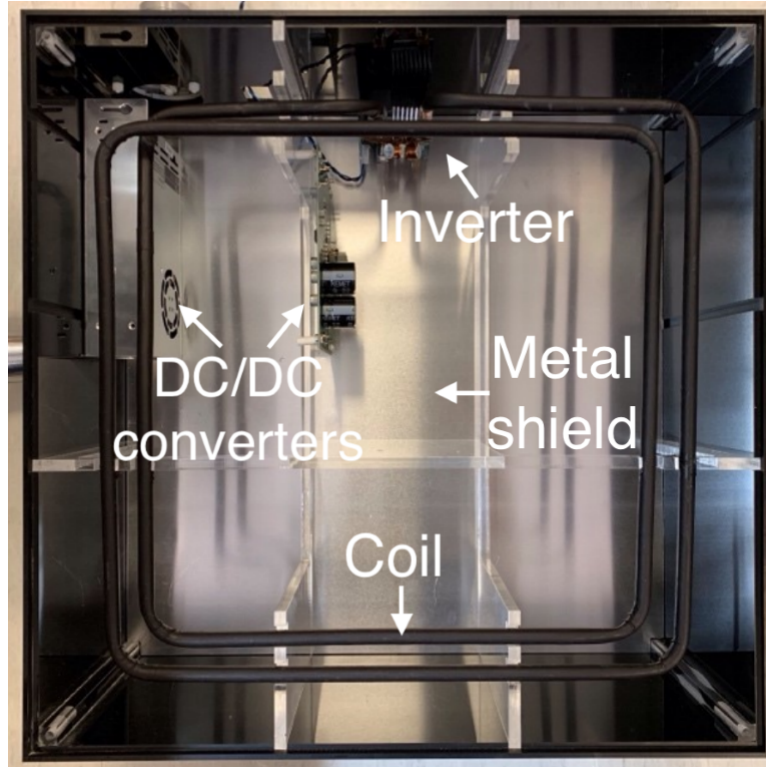


Figure 2.6: The wireless charging transmitter box

The Wireless Power Transmitter

At the transmit side, a load-independent Class EF inverter (Fig. 2.5) was used to drive the coil at a frequency of 6.78 MHz. The design was based on the guidelines in [79], and the component values of the circuit are shown in Tbl. 2.2. The transistor implemented in this inverter was a 30 A 650 V gallium nitride (GaN) transistor (GS66508B) from GaN Systems. One of the key advantages of this topology is that the inverter can maintain zero voltage switching (ZVS) regardless of the reflected resistive load from the receive side, so that the load and coupling variations between the transmit and receive coils do not affect the soft-switching operation of the inverter. The construction of the transmitter is shown in Fig. 2.6.



Figure 2.7: DJI M100 on the edge of the charging pad

Finally, as shown in Fig. 2.7, a one-metre diameter acrylic landing pad was placed on top of the IPT transmitter, where the biggest challenge lies in the ability of the system to operate efficiently independent of the drone's position on the landing pad. The separation of the coils and the size of the landing pad dictate the range of coupling for the drone to land and recharge. As this system relies on variable coupling, it was designed considering the spatial distribution of coupling as in [80] from simulations but also from measurements.

The Wireless Power Receiver

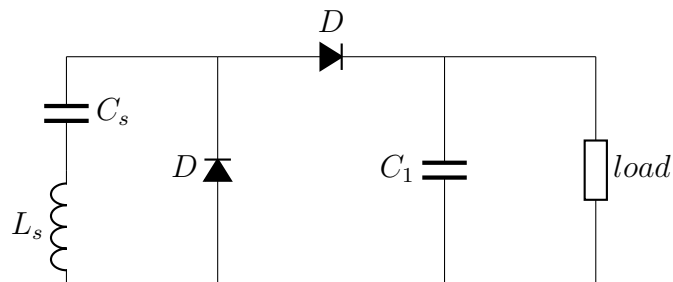


Figure 2.8: Class D rectifier

The receiver side consists of a rectifier and a DC-DC converter to provide a constant output voltage to charge the TB47D battery of the drone. Two common rectifier topologies used in IPT applications were considered during the design process: a class D, and a full-wave rectifier [81].

Circuit simulations were used to determine a suitable topology for this application. The rectifier circuit and component values can be found in Fig. 2.8, Fig. 2.9 and Fig. 2.3, where L_s is the receive coil and C_s is the resonant capacitor.

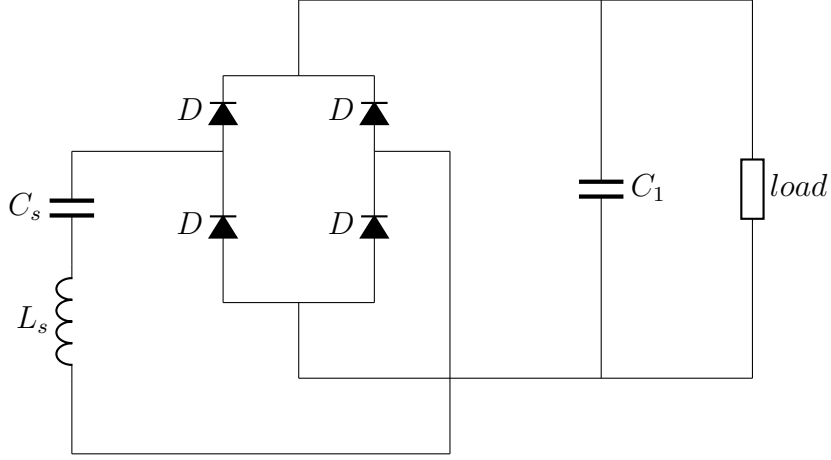


Figure 2.9: Full-wave rectifier

A configuration of high-impedance load ($10\text{k } \Omega$) and maximum coupling (16.7%) was used to determine the maximum voltage at the output of the two rectifier topologies. It can be seen from Fig. 2.10 and Fig. 2.11 that over the full coupling range, class D rectifier topology has an output voltage range between 55 V and 200 V , while full-wave rectifier is between 25 V and 100 V . Since a wider output voltage range would add significant complexity for the design of the next stage DC-DC converter, the full-wave rectifier topology was used for this application.

Silicon carbide (SiC) Schottky diodes (Wolfspeed C3D04060E) were implemented instead of typical chottky diodes, as SiC diodes in general have a higher breakdown voltage tolerance and lower junction capacitance, which could be a major source of energy loss at multi-MHz operating frequency.

Table 2.3: Component values of the rectifier

Parameter	Value/Part No.
L_s	$1.13\ \mu\text{H}$
C_s	$465\ \text{pF}$
C_1	$1\ \mu\text{F}$
D	Cree C3D04060E

As a final power conversion stage, the battery charger for the drone's battery is required to have a wide input voltage range (25 V to 100 V) since the induced voltage on the receive coil

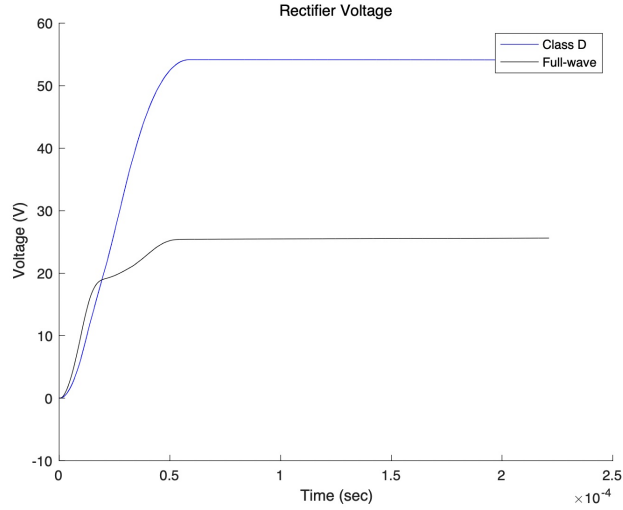


Figure 2.10: Rectifier output voltage at minimum coupling (5%)

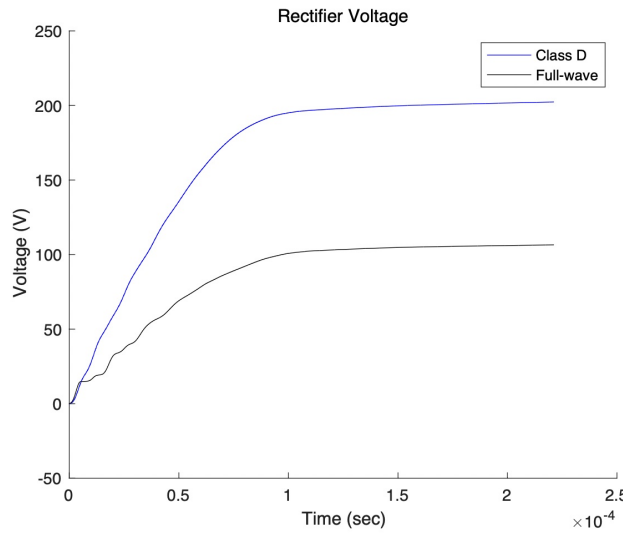


Figure 2.11: Rectifier output voltage at maximum coupling (16.7%)

depends on the coupling, i.e. on the landing position of the drone. The charger should also be capable of handling 100 W to charge the battery within the coupling range. Based on these specifications, a DC/DC converter based on Analog’s LTC3895 chip (datasheet can be accessed at [82]) was developed to perform the last power conversion stage of the system.

The final receive board was designed to integrate both the rectifier and the DC-DC converter electronics, as shown in Fig. 2.12 and Fig. 2.13. The rectifier side (the right side of Fig. 2.12) was designed to leave room to mount heatsinks if necessary. A thermal test was also conducted in the following section to test its thermal capabilities.

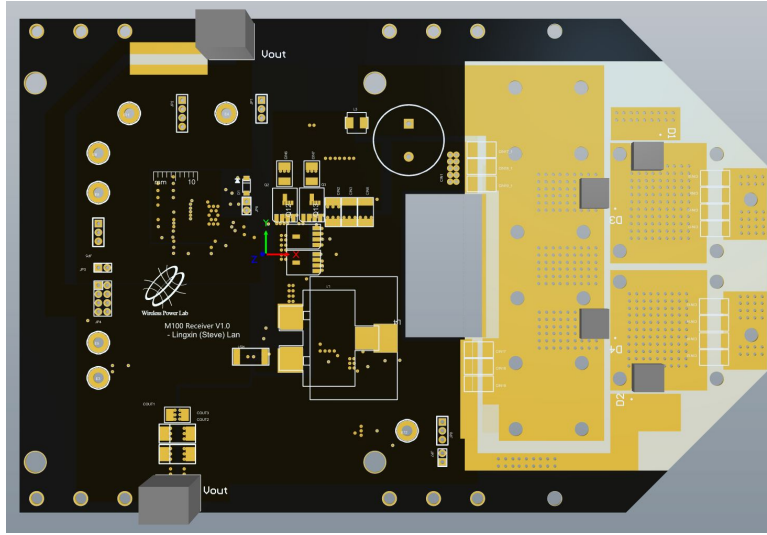


Figure 2.12: Receiver side PCB rendering

2.1.2 Testing

A crucial feature of using high frequency IPT systems for wireless charging of autonomous drones is that these can be designed for a wide range of misalignments and independent of angular orientation [80]. Thus, the drones to be charged do not require a millimetre precise landing system. This section reports on the final testing of the system in the laboratory and how it was later deployed in a real-world scenario.

System Testing in the Laboratory

Using a WT332E and a WT310 digital power meter by Yokogawa, it is measured that the input and output power to determine the average efficiency of the IPT system as the alignment of the coils changes. The proposed IPT system was tested to be capable of delivering 100 W to the drone either at the centre or at any edge of the charging pad without the angular orientation of the drone having any impact on the performance (Fig. 2.7). The system was tested by performing a full charge of the battery several times at different alignments, and the results show that the average mains-to-battery efficiency was 70 % (It changes slightly with the alignment of the coils and the state of charge of the battery). Interestingly, as the drone was moved further from the centre, the output power increased slightly (around 10 W maximum) due to the control configuration of the dc-dc converter after the rectifier.

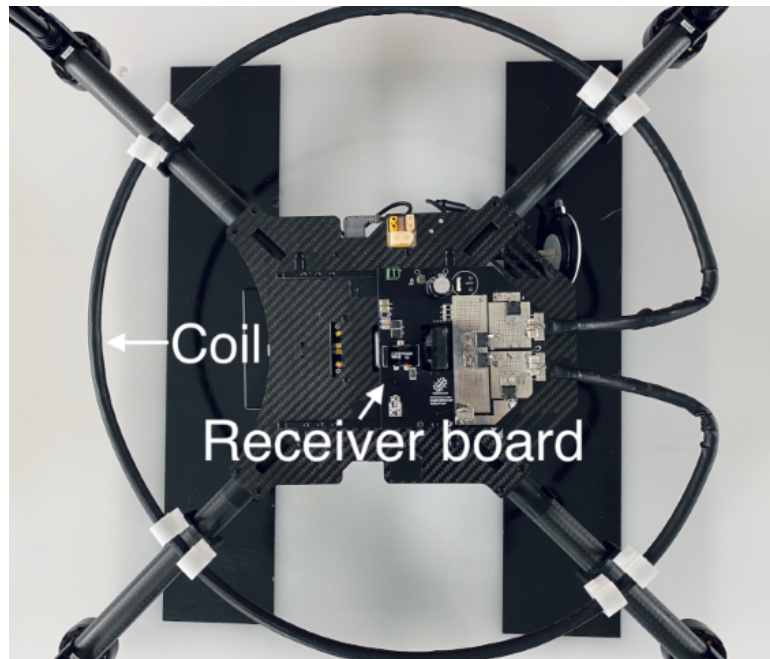


Figure 2.13: The wireless power receiver on the drone

An additional thermal test is also needed to ensure that the system does not overheat while operating for a long period of time during real-world operation. In the lab experiments, the highest temperature was measured at the receive side of the IPT system. The heating was primarily due to the rectification diodes, especially when the drone is placed on the edge of the charging pad. This is as expected since lower voltage is induced at lower coupling, and to ensure the same output power, a higher current is drawn from each diode, therefore, resulting in higher loss in each diode. With proper heatsinks mounted on the receive board, the temperature of the diode settles down well before its limits. Fig. 2.14 shows the thermal test of the receive board at the lowest coupling over 30 minutes. The current in each diode reached 4.49 A during this test. It can be seen that the temperature rose from 25 degrees up to and settled at 80 degrees during this test.

Given the positive outcome of the laboratory tests, the system was then trialled in a real-world scenario.

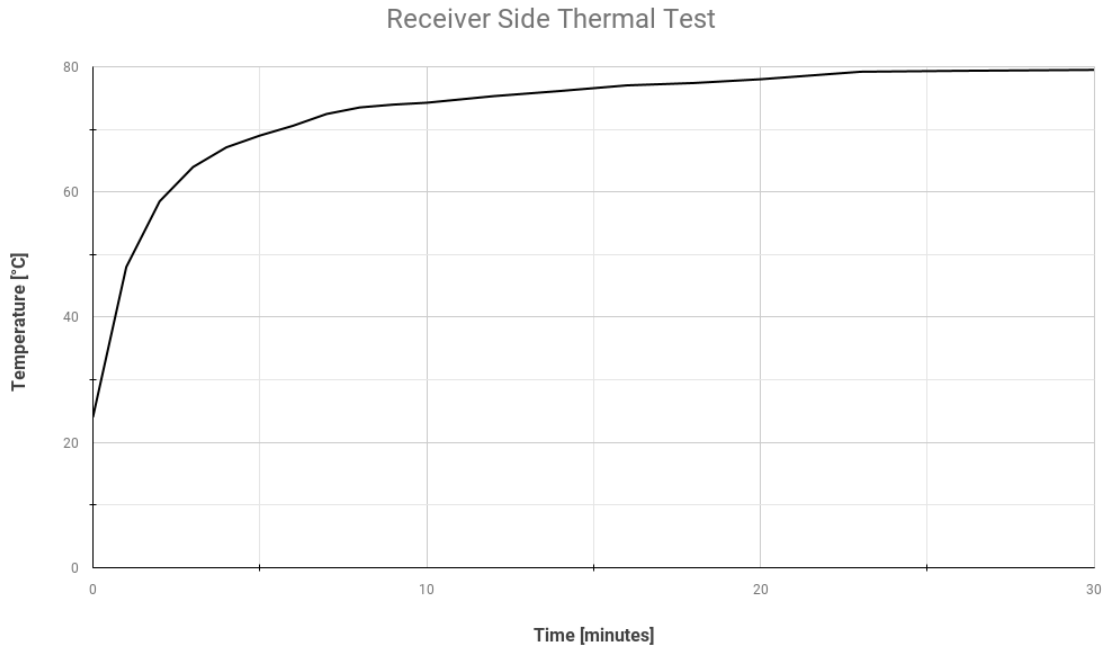


Figure 2.14: IPT receive-side thermal test

Deployment of the Wirelessly Charged Drone in a Real-case Scenario

While the developed system works as expected in the laboratory environment, the robustness of the system still needs to be evaluated as a real application. This was also an opportunity to test if the 6.78 MHz IPT system interferes with the operation of the drone itself when it approaches the charging pad.

A flight-land-charge test was demonstrated in conjunction with Thales on the Halcyon—Thales’s autonomous surface vessel. The challenges involve connecting the system to a power outlet of the ship instead of a controlled AC source (an AC6802A AC supply by Keysight is used) and dealing with environmental conditions, e.g. vibrations from the engine of the vessel, motion due to waves and manoeuvring, wind, humidity, etc. IPT was performed in various scenarios including whilst driving the vessel at a constant speed. In these tests, one could only verify that the battery was being charged by the indicators on the drone and the controller, and an AC power meter was used in the power supply to make sure that the input power of the system was congruent with that measured in the laboratory.

The drone landed on the charging pad several times (2.15) and was charged successfully. There



Figure 2.15: DJI M100 approaching the charging pad on the Thales ASV

was no sign of interference during the entire operation. The complete operation video can be accessed at [83]

2.1.3 Summary

Overall, this work showcased the design and development of a wireless charging system for large-size UAVs which meets the rate of charge of the corresponding plug-in chargers. The system is based on a high frequency inductive power transfer system built with lightweight air-core coils at both ends, a Class EF inverter at the transmit side, and a full-wave Class D rectifier at the receive side. The developed system is capable of delivering 100W to a Matrice 100 drone by DJI when it lands at any position and alignment on a one-metre wireless charging platform. The system has an average mains voltage source to the drone's battery efficiency of 70% and enables hopping and recharging autonomous missions since it eliminates the need for human interference for battery recharging or swapping.

2.2 Building an IPT System for Sensor Network Recharging

While the previous HF-IPT system focuses on charging autonomous drones for autonomous missions, the following application works the other way around: the drone is acting as the charger and used to deliver power to charge other devices to be charged. This work is a collaboration between the Electrical and Electronic Engineering and the Dyson School of Design Engineering in Imperial College London. The author's main contribution in this work includes integrating the IPT transmit side into the DJI MATRICE 100 drone to act as a wireless charger. And the design and development side of the integrated power electronics printed circuit board that contains the battery cells, the IPT receiver side, the rectifier, and a battery management system for battery recharging.

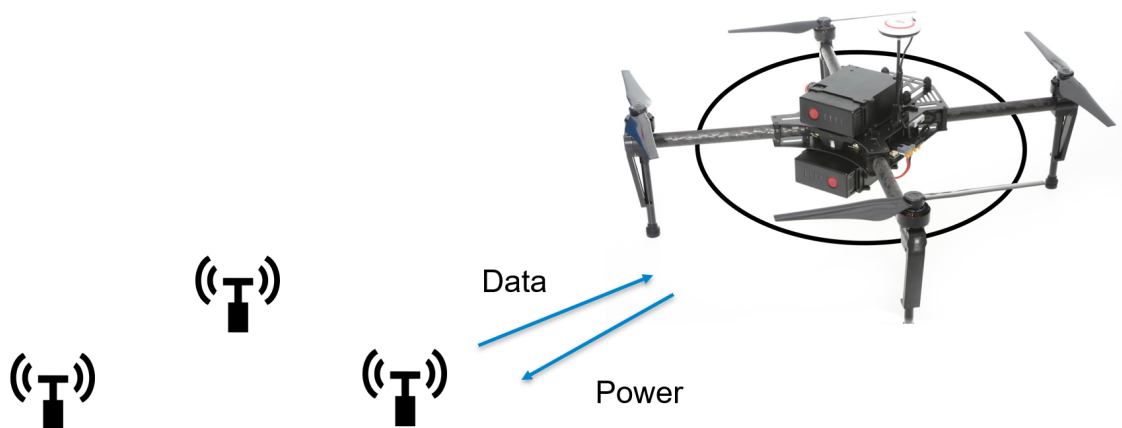


Figure 2.16: System Overview

The basic concept of this work is to allow the deployment of wireless sensors into environments where human access to the sensors for recharging or battery swapping is not appropriate. The objective is to allow unmanned aerial vehicles (UAVs) to locate deployed sensors, supply them with power, and exchange data with them, forming a synthetic sensor network.

To charge the sensor nodes from an UAV (in this case a drone) using physical connectors or contact-based charging would require a precise alignment technique, which is difficult or not possible for most UAVs. Wireless charging could be an alternative solution to this. However,

the widely used Qi-standard wireless charging technologies, although better than physical connectors, still require a rather strict tolerance of misalignment for it to operate normally, as discussed in chapter 1. From the previous chapter, it can be seen that high-frequency IPT system, on the other hand, could achieve a significantly higher tolerance of misalignment, compared to the Qi-standard charger, and therefore, is also used for this application.

2.2.1 System Overview

The system can be divided in to three parts as the following:

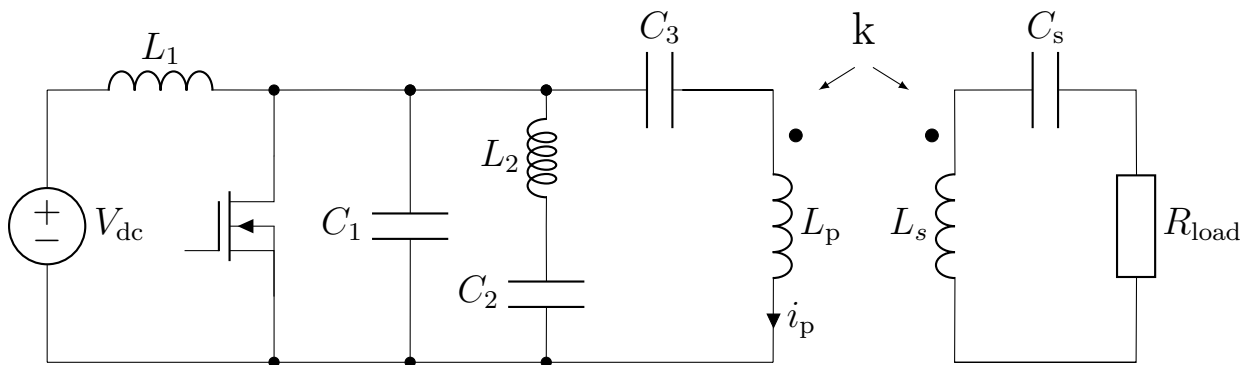


Figure 2.17: Class EF inverter circuit topology

Part 1: The integration of IPT transmit coil into the DJI Matrice 100 drone platform – unlike the previous drone charging application, an IPT transmit unit is mounted to the bottom side of the drone and powered by its battery.

Part 2: The High energy and charge rate receiver and RX side power electronics – to provide a fixed 5 V rail to a load and allow a lithium battery to be rapidly charged. The sensor nodes in this case will be based on state-of-the-art, lower power, higher memory, multi-radio system-on-chip implementations.

Part 3: User Interface – A basic user interface (web app) to facilitate control of the system, including navigation, data collection, and charging information, will be developed in support of the overall system.

2.2.2 The Integration of IPT Transmitter into a Drone

The wireless power transfer system in this work is used to charge the batteries of the sensor nodes and assist the drone to locate the sensor nodes. The wireless charging system is a HF-IPT system that uses a 13.56 MHz load-independent inverter topology designed by the Wireless Power Lab, Imperial College London. The system consists of two major parts, the wireless power transmitter and the receiver.

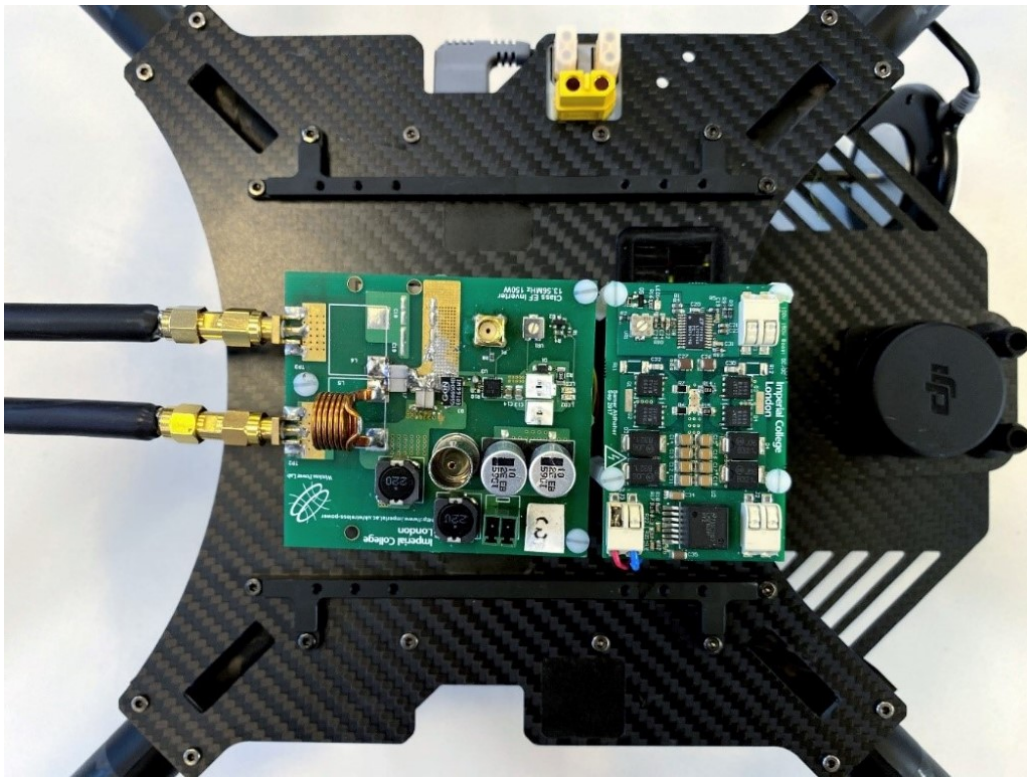


Figure 2.18: Inverter (left) and DC/DC converter (right) hardware

The wireless power transmitter unit is mounted on the centre of the drone, connecting to the transmit coil mounted under the four “arms” of the drone, as shown in 2.19. The transmitter unit consists of a boost DC/DC converter to step up the voltage from the drone’s battery to power the inverter. The inverter therefore converts the DC voltage to AC current in the coil. Each individual part of the wireless power transmitter is described as follows.

The DC/DC Converter

A DC/DC converter was used to provide two voltage sources to the inverter. A 5 V DC voltage to supply the gate driver and other low-power electronics. For this particular design, A 80 V DC voltage is used as the input to the inverter.

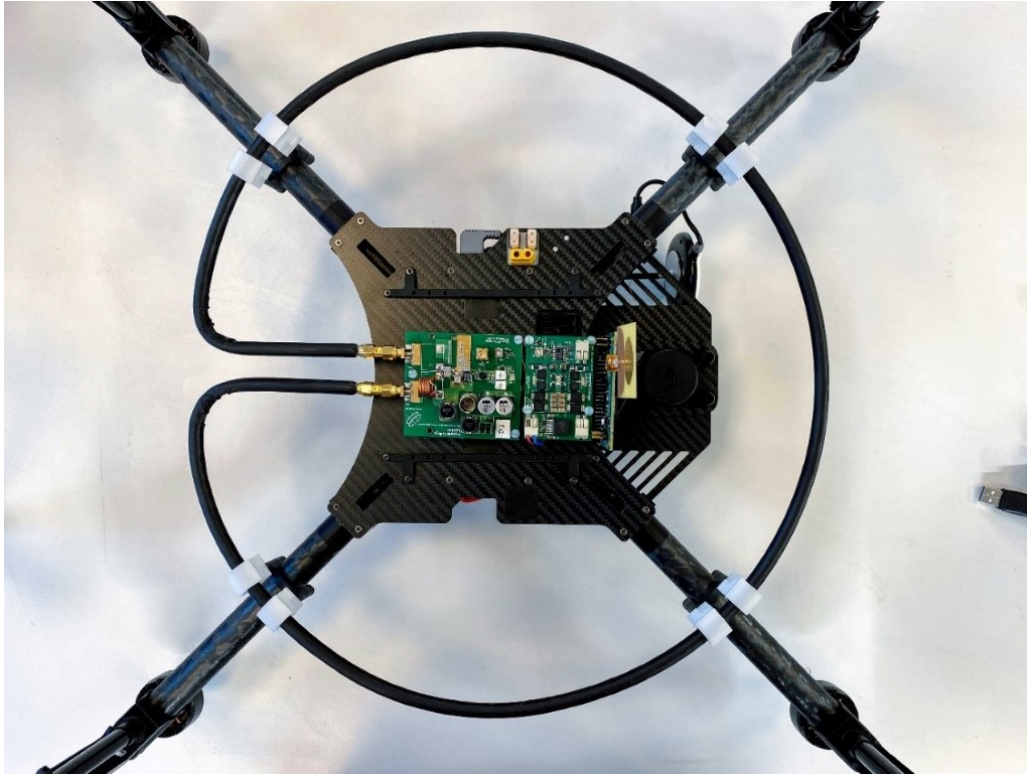


Figure 2.19: Transmit coil attached to the drone

The DC/AC Inverter

In this work, a 13.56 MHz Class EF inverter is used. This particular design is load-independent, low-weight, and high power (rated at 150 W), which is ideal for this application. The circuit topology of this inverter can be found in Fig. 2.17. The actual hardware is shown in Fig. 2.18

The Transmit Coil

As shown in Fig. 2.19, a copper pipe-based coil is designed to mount on the frame of the DJI Matrice 100 drone, which improves the robustness of the IPT system. Such a mounting method

could reduce the difficulty of aligning the transmit coil with the receive coil using point-to-point localisation technique, e.g., UWB. The coil is wrapped with a heat shrink for safety purposes. The diameter of the coil is also designed to maximise the tolerance of misalignment.

2.2.3 The IPT Receive-side Electronics and Sensor Node



Figure 2.20: receiver side power electronics

A PCB is designed to integrate all separate modules on the sensor node side. This integrated board includes connectors for the IPT receive coil, a rectifier, a DC/DC converter, a battery management system module, a battery holder with up to two 18650 type cells and finally an interface to power and communicate with the sensor node. The complete PCB plus the IPT

receive coil is shown in Fig. 2.20.

The IPT Receive Coil

The wireless power receive coil designed is a single-turn rectangular copper pipe-based coil, as shown in Fig. 2.20. One advantage of such a coil design is the flexibility of reshaping. The size of the coil is maximised for better tolerance of misalignment with the transmit coil. Like the transmit coil, it is also wrapped with heat shrink for safety protection.

The Rectifier & DC/DC Converter

Both the rectifier and DC/DC converter were integrated, together with the battery management, into the same receive side PCB. The rectifier is a common full-wave rectifier with four SiC diodes (Wolfspeed C3D04060E, datasheet can be accessed at [84]). The bulk DC/DC converter is designed based on Analog's LTC3895 chip (datasheet from [82]). The converter takes the rectified DC voltage as input (up to 140 V) and outputs a constant 5 V to charge the 18650 battery cells with a max current of 5 A.

The Battery Management System

In addition to the rectifier and DC/DC converter, the integrated receive board also includes a battery management system (BMS), designed based on TI's BQ25895 chip (datasheet at [85]). The BMS is able to charge single or multiple lithium battery cells with a maximum current of 5 A. Another use of this BMS is to check the status of the battery cells and report to the sensor node via an I2C communication link.

The Battery Cells

The battery cell selected for this work is the Panasonic NCR18650B 18650 lithium cell with a capacity of 3400 mAh [86]. This cell also supports fast charging with a peak charging current



Figure 2.21: Panasonic 18650 cell (www.nealsgadgets.com)

of 4 A, which allows it to be charged from 20% to 80% in less than 30 minutes.

The Sensor Node

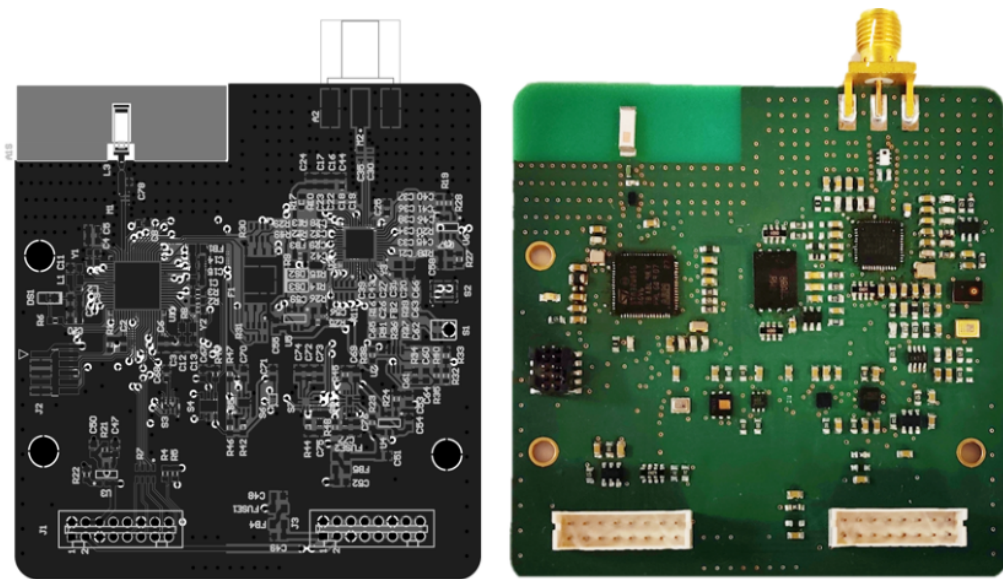


Figure 2.22: the sensor node board (Tommaso Polonelli)

A sensor node board has been designed and developed in collaboration with the Dyson School of Design Engineering, Imperial College London. The board was designed to transmit and record data from the various sensors attached to it. The sensor node has I2C, SPI, and analogue interfaces for different sensor connections. With an audio sensor attached, the node can be configured to be audio-triggered wakeup for event recording, which also saves power and storage.

The sensor node communicates with the drone via the UWB antenna, which can achieve up to 6.8 Mbps bit rate.

2.2.4 The User Interface

With both the IPT transmit and receive units designed and developed, a basic web-based user interface (UI) has also been designed and developed for users to understand the status of the system and access the collected data from the sensor node. This work was accomplished in collaboration with Niall Woodward. The UI is based on a map that displays the current deployment of the sensor nodes. A click on each sensor node would display the latest sensor information collected from the drone. The sensor node also displays the battery status of the sensor node and can be used to initial the “recharging” process when necessary. A demonstration of the UI is shown in Fig. 2.23, where four sensor nodes were deployed.

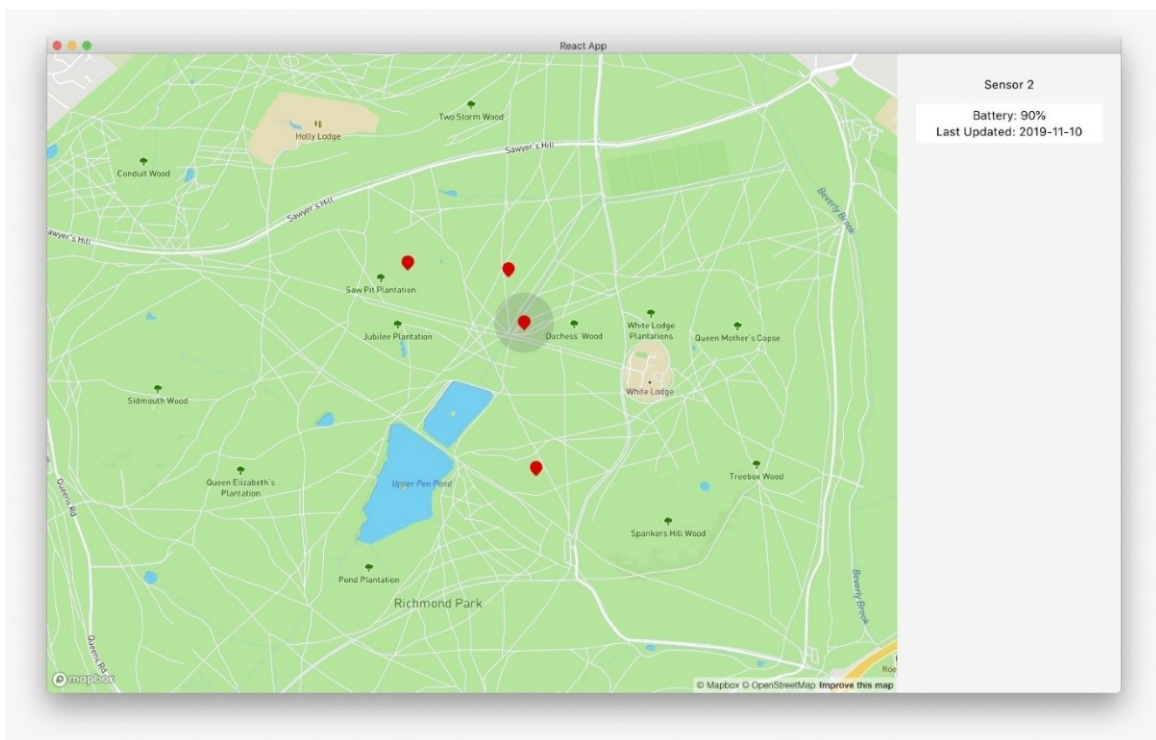


Figure 2.23: A web-based UI

2.2.5 Summary

Overall, this work showcased the potential of HF-IPT, especially its tolerance of misalignment, which is crucial for this application to work. The typical Qi-standard wireless charging solution would require the transmit and receive coils to be aligned in centi-meter level to start charging. The demonstrated IPT systems could allow sensors to be deployed to places where human or energy access is difficult.

Chapter 3

Analysis of Foreign/ Living Object Detection Methods

The two IPT systems showcased in the previous chapter demonstrated the potential of HF-IPT systems. It can be seen that a wider charging range and higher power level could enable a significantly wider range of applications, compared to the Qi-standard solution. However, before such technology can be implemented on everyday electronic devices or electric transport vehicles, the safety of it must be assessed and ensured. Chapter 1 has discussed some of the common safety concerns of IPT systems in detail. In this chapter, the primary focus is to analyse some of the safety systems that have already been applied to the commercial IPT system, as well as some methods proposed in recent research. A number of existing and potential FOD/LOD solutions are benchmarked with various numbers of parameters. Depending on the application, the most suitable FOD/LOD solutions are then explored further to evaluate their performance. While some proposed FOD/LOD methods can be applied to both LF-IPT and HF-IPT, some methods that work on LF-IPT may not be applicable to HF-IPT and vice versa. The analysis in this chapter could be used as a reference for designing FOD/LOD systems for HF-IPT systems.

3.1 Properties Definition

Before analysing any FOD/LOD method, it would be sensible to start with the basic principles of such a safety system. Regardless of which FOD/LOD method is used, the detection workflow is essentially the same. At the start the wireless charging process, the FOD/LOD checks for the safety status, and based on the result of this process, it decides whether to start the charging or repeat the detection. A simple workflow of such a system is shown in Fig. 3.1. During the charging process, the FOD/LOD system continues to monitor the status and pause the charging if unsafe operation is detected.

To better evaluate different FOD/LOD implementations, it is useful to first define some relevant properties that can be used to represent the performance of those methods. There is no rank for the properties defined below, as their importance may vary depending on the application.

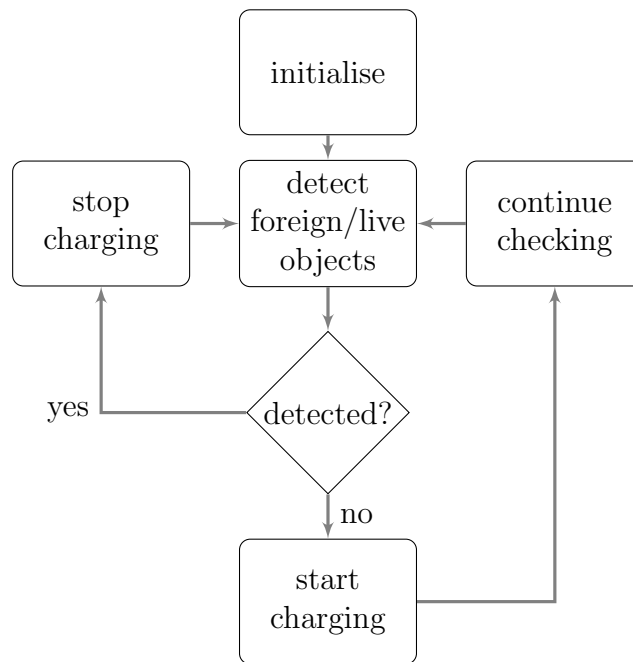


Figure 3.1: FOD/LOD workflow

- Accuracy

The detection accuracy describes how accurately can a FOD/LOD system detect the objects. For FOD/LOD, a high accuracy means an unintended object has a high chance to be detected

by the system. An accurate system should also be capable of distinguishing between the wireless power receiver and foreign/ living objects to reduce false positive detection.

- Speed

The detection speed describes how fast the system can detect unintended objects. Depending on different scenarios and safety requirements, the required detection speed may vary. In the case of induction heating of foreign objects, for example, the time of detection could be relatively long before the objects heat up to a dangerous level. This time could also vary depending on the power level of the IPT system, the material of the objects, or the size of the objects.

Regarding the EM exposure, the ICNIRP 2010 recommended SAR level is based on an average value over 6 minutes, which means a higher SAR is acceptable for a short period of time. In general, a higher detection speed is always desired to minimise potential risks.

- Range

The detection range describes how far the FOD/LOD system can effectively detect the objects without losing many of the other performance benchmarks. This property may not be essential for low power level or short range IPT systems. However, for IPT systems that have a higher charging power and range, e.g., an electric vehicle wireless charger, the detection method may need a wider detection range to avoid unintended objects.

- LOD

This feature specifically describes the performance of detecting live objects, including humans and animals. While some FOD systems can accurately detect other objects, e.g., metal, it may fail to sense the presence of live objects. A live object detection is not needed if the IPT system itself is intrinsically safe based on the guidance from IEEE or INCIRP or other authorities.

- Robustness

The robustness of a FOD/LOD system describes the reliability of the system under different circumstances. A robust FOD/LOD system should be resisted to the environment change, e.g., change of loading conditions, change of weather condition, temperature, humidity, sun light, etc. A self-calibration could also increase the robustness of a FOD/LOD system.

- Sensor Integration Type

The integration method of the sensor is also important as this could affect the deployment of a wireless charging system. An easy-to-integrate sensor could reduce the complexity of the installation process of an IPT system. The integration of the sensor could be classified into two categories. One type can be easily integrated inside the IPT system, the other type is an external sensor, which means the sensor has to be mounted/installed in addition to the IPT system and can work as a standalone system. A simple example of an external FOD/LOD sensor is a camera.

- Cost

The cost of the FOD/LOD system should be kept as low as possible for it to be practical. A thermal imaging device could easily detect objects that are heating up, but it could be significantly more expensive to implement compared to other methods. In addition to the cost of the sensor itself, the cost of implementation should also be considered. For example, a camera sensor would also require a processor unit to perform the detection.

3.2 Analysis of Existing and Potential IPT FOD/LOD Implementations

With those properties of interest defined, it would be useful to use them to analyse the FOD/LOD methods that are already being used in commercial IPT products, as well as those being proposed in research papers, or similar techniques that used in different applications. The

Q-factor and efficiency measurement FOD/LOD methods are the ones that already are used in the Qi-standard wireless chargers [87]. Ultrasonic and visible light based FOD/LOD methods are also benchmarked here as they are common object detection methods and are used in a wide range of applications. Finally, a mmWave radar-based solution was also examined as such technology has been gaining popularity in various fields over recent years. Based on the result of the analysis, one or more methods that show good potential will be explored in more detail.

3.2.1 Q-factor measurement method

As the most widely used wireless charging standard, it is not surprising that the Qi standard requires a certified Qi charger to have a FOD/LOD system built-in. One of the suggested FOD/LOD methods by Qi is the Q-factor measurement method [87, 88]. This FOD/LOD method is primarily used to detect foreign objects before initialising the charging. The theory behind the Q-factor measurement method is that the Q-factor of a coil changes when foreign objects are coupled to the coil (being loaded). One way to interpret the quality factor of a resonant tank is how many cycles can the energy oscillate within the tank before it dissipates, the higher the Q, the higher the number of oscillations before significant energy decay. However, when foreign objects, especially metal objects, are coupled to the coil, it consumes the energy as the eddy current in the foreign objects and therefore the energy within the resonant tank decays faster and therefore the Q decreases, as shown in Fig. 3.2. By comparing the measured Q-factor with the predetermined unloaded Q-factor, it is possible to detect the existence of objects that could affect the Q-factor of the coil.

Accuracy- For objects that could be heated up by the IPT system, they could also change the Q-factor of the transmit coil, therefore this method can be accurate. However, this method is not able to detect objects that do not affect the Q-factor of the coil. In addition, since the Q-factor is also affected by the IPT receiver, and the Q-factor is difficult to measure whilst power is being transferred, this method could not perform accurately during power transmission [87].

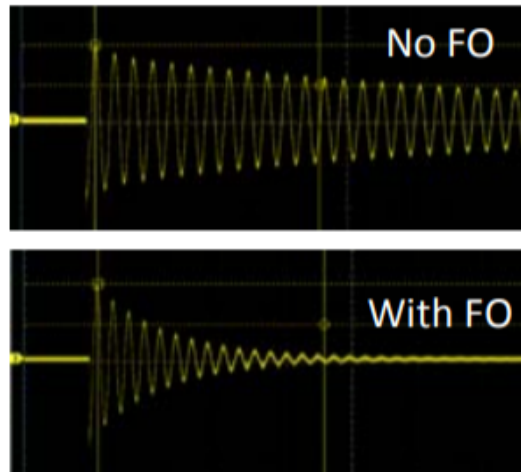


Figure 3.2: Q-factor change with foreign objects (wirelesspowerconsortium.com)

Speed- The detection speed of this method depends on the measurement method used to measure the Q-factor. One example of this method uses a microprocessor to excite the transmit coil with a signal generator and determine the Q-factor by measuring the peak and average voltage across different frequencies [89]. The speed of this measurement is determined by the clock speed of the MCU, which can easily be changed. In addition, if this method is only used before the initialisation of charging, the speed of detection could be flexible without any safety risks.

Range- The detection range of this method is completely dependent on the foreign objects. The size, shape, and material of foreign objects could all affect the Q-factor of the coil differently at a given position. This flexible range makes such FOD/LOD/LOD method ideal to prevent accidental induction heating of foreign objects. However, for objects that do not load the Q-factor of the coil and still need to be detected, the range of detection could be too smaller.

Robustness- If only used to detect unintended objects without the receiver, this method is considered robust since the environment change, e.g., temperature, humidity does not affect the coil's Q-factor significantly compared to foreign objects e.g., metal. However, with the presence of the receiver, the Q-factor of the transmit coil could also be changed due to the IPT receiver,

which would impact the performance of this FOD/LOD method.

LOD- Since this FOD/LOD method only detects objects that could noticeably change the Q-factor of the coil, this usually means objects that have relatively low impedance at the operating frequency of the IPT system e.g., metal objects. The impedance of human arm is approximately 300 ohm at 100 kHz according to [90] while a thin piece of copper only has approximately 1.5 ohm. Therefore, this method is not suitable for detecting live objects at this particular frequency. However, since the impedance could change with frequency, it is possible that live objects could be picked up at a different operating frequency.

Integration type- built-in, no external installation is required for this FOD/LOD method.

Cost- An accurate measurement of Q-factor could be expensive to implement. In this scenario, the precision is not the priority and therefore simpler methods could be used to measure the Q-factor of a coil. [89] showcased a method of measuring Q-factor using a microcontroller. Overall, this FOD/LOD method does not require any external sensor, which also saves the implementation cost.

3.2.2 Efficiency measurement method

Another method recommended by Qi is the efficiency comparison (or loss balance) method [87]. This method is designed to work during the wireless power transmission and the idea behind this method is rather straight forward: the IPT transmit side constantly monitors the power sent from the transmit side and the power received from the receiver side (via a communication link), and comparing the difference to a predetermined threshold. This method assumes foreign objects are the only cause of the efficiency loss and therefore stops charging when the loss exceeds a predetermined threshold.

Accuracy- If foreign objects were the only cause of the efficiency loss, this FOD/LOD method could achieve almost 100% detection accuracy. However, as discussed in the previous chapter, the efficiency of an IPT system depends on both the coupling factor k and the quality factor Q (Equ. 1.5), which means the relative position of the transmit and receive coils could also affect the efficiency of the system, especially when the Q of both coils are low. Therefore, when the loss threshold is set too low, this FOD/LOD could be triggered by a slight displacement of the transmit and receive unit and limiting the range of wireless charging. Fig 3.3 and Fig 3.4 both show a mobile phone placed on top of a Qi compatible charger, however only the left one shows successful charging because it is perfectly placed on top of the charger. On the right hand side, when the device is placed slightly (1 cm) off the centre of the charging pad, it stops the charging process. This is an example showing how easily the efficiency difference threshold can be reached by misalignment. One could increase the threshold to increase the tolerance of misalignment, however, this also increases the chance of heating up foreign (especially metal) objects to a higher temperature, as small metal objects could miss the detection and still heat up slowly. This problem can be more severe for higher power IPT systems because even a small change of efficiency could mean a high loss of energy. In addition, when objects do not draw enough power from the IPT system and still need to be detected (e.g., to meet ICNIRP SAR limit), this method may not be acceptable.

Speed- Since the detection is simply a comparison of the efficiency, the detection speed is primarily dominated by the communication link between the transmit and receive side. Since the information transmitted is extremely small (a number showing the power transmitted/received), this transmission should be quick for any communication link.

Range- Similar to the accuracy part, the range of this FOD/LOD method would depend on the loss threshold, when set lower, this method should be able to detect objects further. Again, this lower threshold could affect the accuracy of detection.

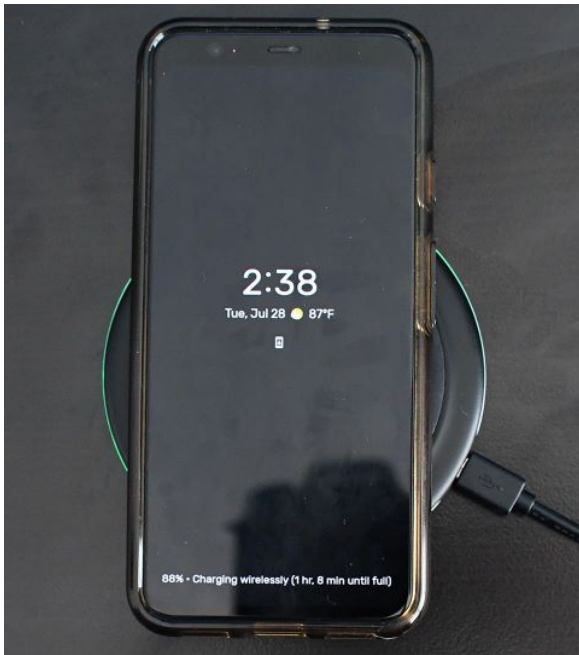


Figure 3.3: Phone Charging

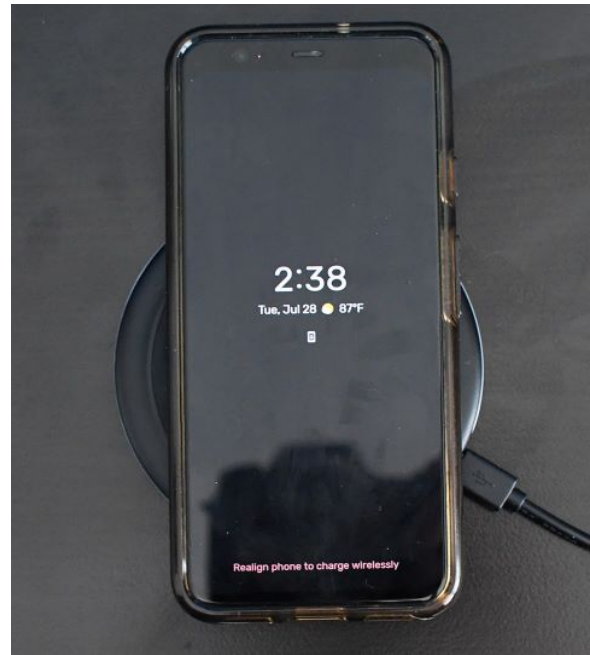


Figure 3.4: Phone NOT Charging

Robustness- Since this method only measures the transmitted and received power, which does not easily affected by environmental changes, e.g., temperature, humidity, etc., this method is relatively robust.

LOD- Since this method could only detection objects that draw power from the IPT system and human bodies or animals do not draw power from an IPT system within the common IPT frequency range (kHz to MHz) due to its high impedance at these frequencies [90], this method struggles to differentiate live objects from other objects.

Integration type- Partially built-in, no external installation is required for this FOD/LOD method. However, an external communication link between the wireless transmitter and the receiver is needed for this detection to work.

Cost- As the detection was done by basic calculations, no expensive sensor processing unit is required, the cost of implementation is relatively low.

3.2.3 Ultrasonic



Figure 3.5: A ultrasonic sensor (sparkfun.com)

Ultrasonic sensors are commonly used in industry or consumer applications [91] [92]. Ultrasonic sensors detect objects by measuring the sound wave reflected from the objects. Accurate distance between the sensor and the object can be calculated by the time interval and the speed of sound. While the field of view of an ultrasonic sensor is limited, multiple sensors can be used to increase the angle of detection, a good example is the parking assist system commonly seen on modern vehicles (Fig. 3.6). There are many advantages of an ultrasonic sensor-based FOD/LOD system, e.g., accurate distance measurement, relatively low cost and flexible configuration, etc. However, the disadvantages are also obvious, for example, such a system is unable to differential different materials, and the ultrasonic wave can be easily reflected even with a single piece of paper. In addition, the mounting of the sensor could be another challenge for a compact IPT system to detect objects with a wide angle of view. A more detailed analysis of this ultrasonic based foreign object detection system is presented below.

Accuracy- The ultrasonic sensor is capable of detecting anything that reflects the transmitted



Figure 3.6: Automobile parking assist system based on ultrasonic sensors

ultrasonic wave, within a few cm accuracy [93]. This makes such FOD/LOD system capable of detecting any unintended objects within a certain range. However, this also means that ultrasonic based FOD/LOD can be triggered by intended objects, e.g., the wireless power receiver or objects that do not cause any safety hazard, e.g., a piece of paper. Overall, the ultrasonic FOD/LOD is an accurate FOD/LOD system except it could not distinguish between foreign objects and the wireless power receiver.

Speed- the detection time of an ultrasonic sensor depends on both the speed of sound wave and the processing speed of the MCU. Certainly the speed of sound is significantly slower than light, the ultrasonic based FOD/LOD is still a fast detection system.

Range- The range of typical ultrasonic sensors can easily outperform the charging range of the IPT system itself with a range up to 10 meters [94]. However, this is the detection range when objects are placed within the field of view of the sensor, which can be limited to only a few degrees for some sensors, e.g., in Fig. 3.8. However, this can be addressed by either larger field of view sensors or multi-sensor configuration (Fig. 3.7). Overall, the range of ultrasonic based FOD/LOD can be flexible.

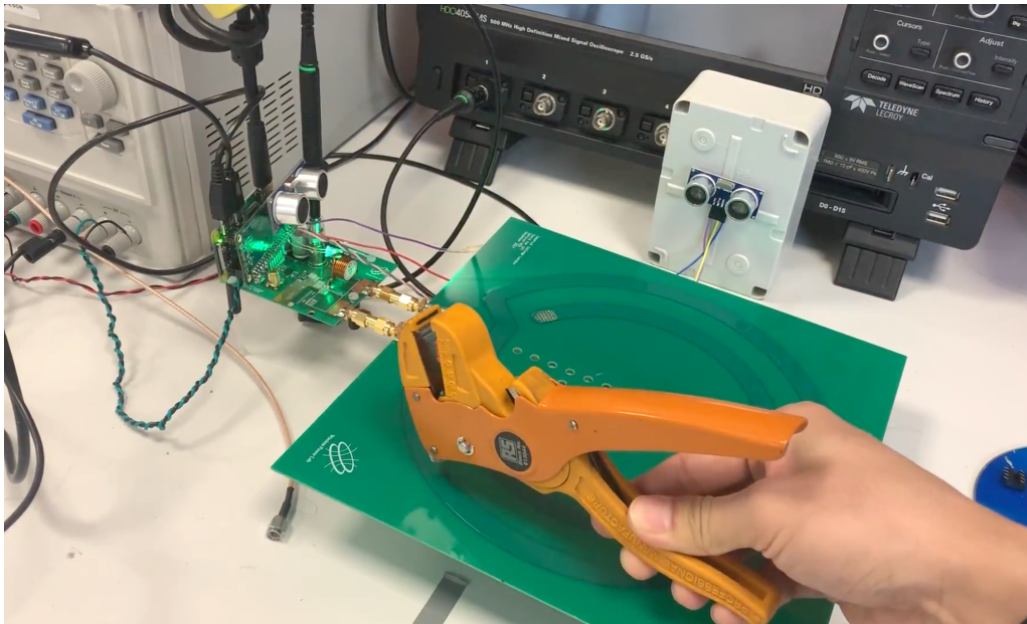


Figure 3.7: Object detected on an ultrasonic-based FOD/LOD system

Robustness- because most materials could reflect sound waves. Ultrasonic sensors could make false detection due to heavy rain or snow. The sensor itself could also fail with a coverage of dust or snow. Therefore, the robustness score of ultrasonic FOD/LOD is low.

LOD- Similar to the robustness, both living or other foreign objects could reflect sound waves, which means the sensor is unable to differentiate between live and foreign objects.

Integration type- For a better angle of view, an external mount would be more practical for the ultrasonic FOD/LOD system

Cost- For a better detection range, multiple sensors may be needed, which would increase the cost. The external installation also increases the implementation cost, hence the cost performance is rated “medium”.

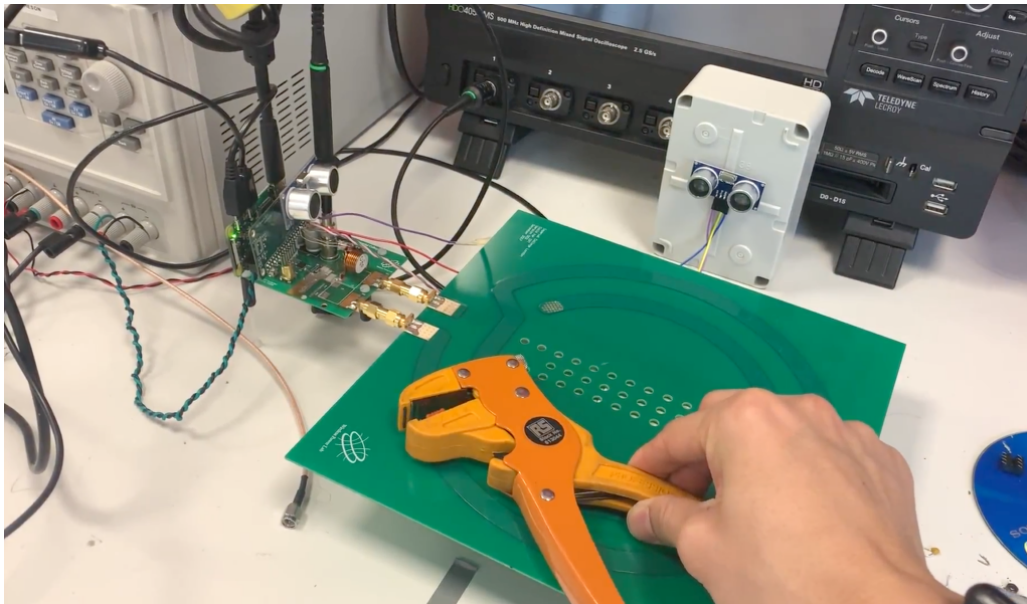


Figure 3.8: Object not detected on an ultrasonic-based FOD/LOD system

3.2.4 Visible Light

Detecting objects using visible light, e.g., camera sensors, has been getting popular over recent years, thanks to the advancement of machine learning technology [95–97]. In the automobile industry, for example, cameras are used in cars to detect other vehicles, cyclists, pedestrians, traffic lights etc [98]. Such a detection method usually requires additional hardware, e.g., microprocessors to perform object detection/classification algorithms.



Figure 3.9: A camera module for Raspberry Pi (raspberrypi.org)

Thanks to the rapid development of vision-based machine learning algorithms, detecting objects

using cameras has become easier and cheaper [99]. Fig. 3.10 shows a real-time object detector app (iDetector) that runs on a mobile phone. The app runs on a trained model that is capable of detecting up to 80 different object classes at 30 frames per second. With sufficient training, such a method can be used to recognise objects that are concerned by IPT systems.

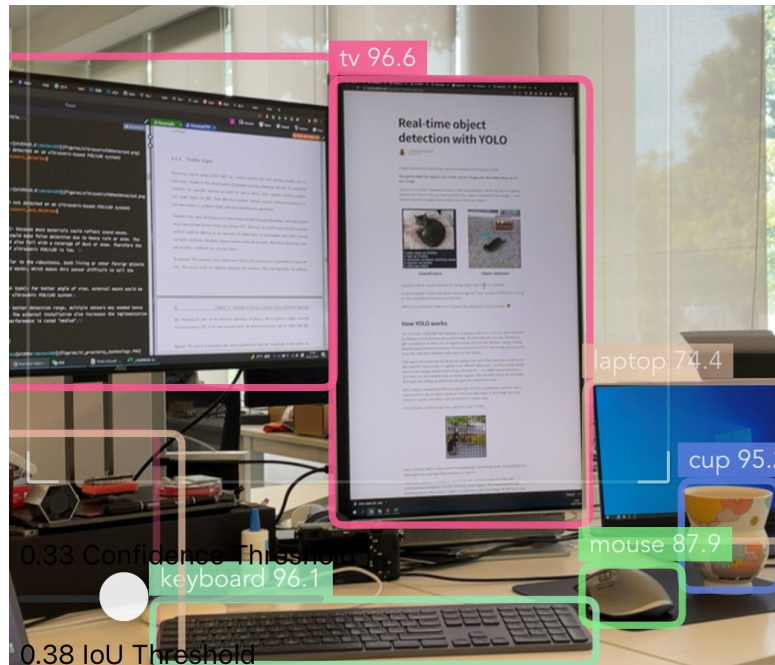


Figure 3.10: A real-time object detector using YOLO (ultralytics.com)

However, the performance of such a detection method could be affected by the intensity of visible light; its performance may reduce during low-light conditions. Similarly, camera sensors could also be easily affected by dust/snow cover and weather conditions, e.g., rain and snow. A more detailed analysis of such object detection methods is shown below:

Accuracy- The accuracy of an vision-based object detection system depends on many factors. The sensor itself, the lighting condition, the hardware that runs algorithm, the software, the “training process” of the detection algorithm all plays a role to achieve a highly accurate detection system [99]. If all done appropriately, the detection accuracy can be rather high [100].

Speed- The speed of detection also varies significantly with the complexity of the model, the speed of the processor that runs the model. This means the speed of detection can be increased, but with the increase of cost and possibly the size.

Range- Depending on the camera system and the application, one could increase the detection distance by using different type of camera lens or with extra lighting, while for IPT FOD/LOD system a wider field of view is more useful, which could be achieved with a wide angle lens. This makes vision-based FOD/LOD rather flexible in terms of range.

Robustness- the performance of a vision-based detection could be affected by the lighting condition. The same detection model may perform much worse in the dark than in bright sunlight. Extra care is needed to improve low-light detection, e.g., adding light compensation to the system or using extra camera sensors, e.g., infrared sensor. In addition, a camera sensor covered with dirt or snow would also not function properly. This makes vision-based FOD/LOD a noise sensitive detection method.

LOD- Like any other object, a vision-based detection can also be 'trained' to detect a live object, e.g., a human being or a cat. This could easily make vision-based detector a rather a live object detector [101].

Integration type- For a better detection range, external installation would be more practical for a vision-based FOD/LOD method.

Cost- The cost of an overall vision-based detection system is heavily dependent on the actual application. If the detection accuracy and speed requirement is high, it could significantly increase the cost due to the better quality sensor and faster processing unit. Likewise, a low-cost solution is also possible if lower accuracy and speed can be accepted.

3.2.5 Radar

Recent years have seen increasing applications of radar sensors in various industries. In the automotive industry, millimeter-wave (mmwave) radars are used as a common sensor to enable self-driving capabilities [102]. A radar detects objects by transmitting a signal across a certain frequency range, and by processing the signals reflected back to the sensor, the range, direction, and even speed of the objects in the sensor's view can be calculated [103].

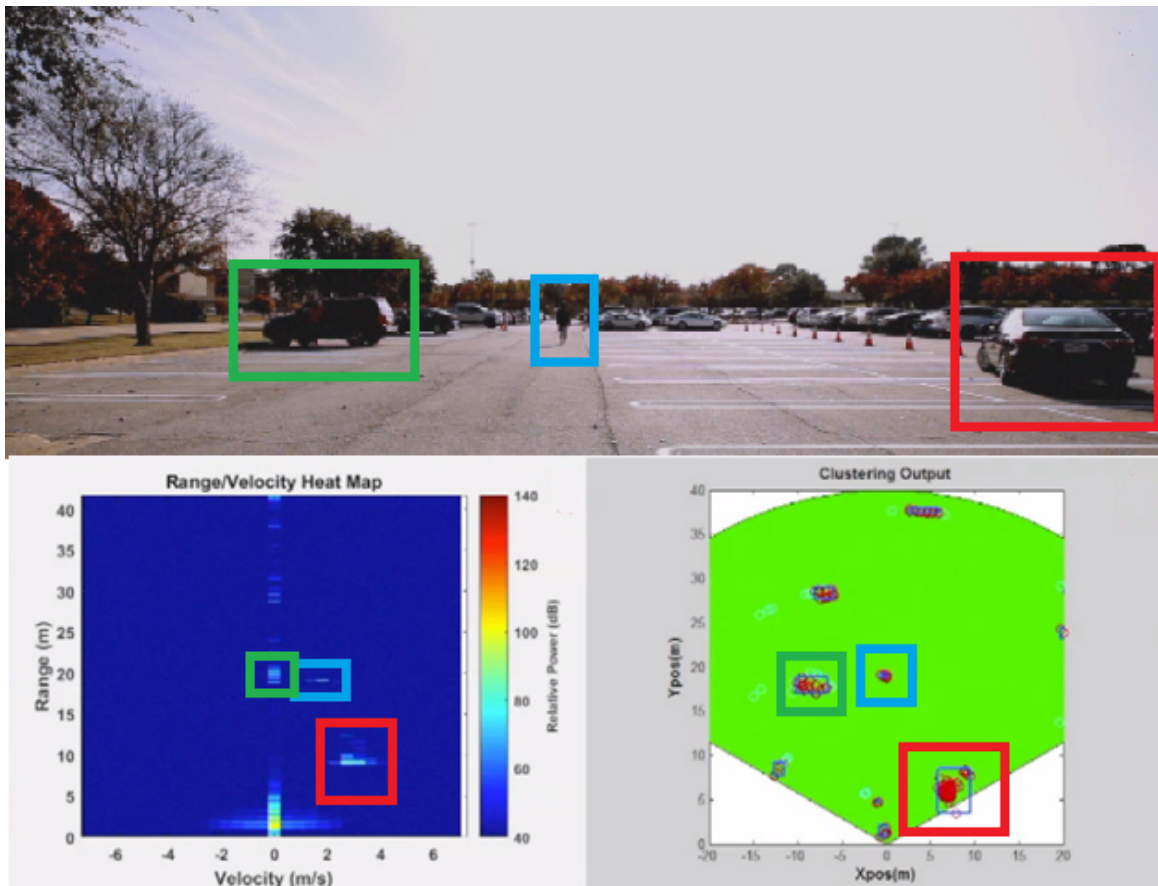


Figure 3.11: A mmWave radar demo (ti.com)

The performance of a radar is determined by various factors, frequency, antenna design, etc. Radar can be used as a method to detect foreign objects for IPT systems [104]. A mmWave radar sensor from Texas Instruments, for example, could detect objects as small as a coin within a few meters range [105]. Such setup could be suitable for FOD/LOD, a demo of mmWave radar detects objects is shown in Fig. 3.11.

Accuracy- Depending on the frequency and antenna design, a radar system can provide ac-

curate detection for various applications. Reference [105] shows a mmwave radar can detect a coin within a few meters. However, this also means mmWave radar is sensitive to small objects or small movement of objects. Additional data processing, e.g., object classification for the sensor can be used to better detect objects of interest.

Speed- Similar to vision-based object detection, the detection speed of a mmWave radar sensor is dependent on the sensor itself and the processing unit. Higher detection speed is achievable if better hardware is used [106].

Range- The detection range of a radar system can be customised based on the applications. There are radar systems focusing on long distance detection and there are ones for short range but wider detection angle of view [105].

Robustness- A suitable selection of radar frequency could allow the system to see through dust and snow. Radar systems could also function regardless the lighting conditions. This is one of the reasons automotive industry uses mmWave radar on vehicles to detect other vehicles ahead [107]. Therefore, a mmWave radar-based FOD/LOD is also relatively robust.

LOD- Thanks to the advancement of machine learning in recent years, there has been an increasing interest in performing object classification based on mmWave radar. [101] has shown an application of using mmWave radar to classify human objects. This makes it possible to design a LOD system for IPT system using mmWave radar sensor.

Integration type- For better detection range, an external installation method would be practical for a radar-based FOD/LOD system.

Cost- traditional radar system requires complicated hardware setup, which also means a higher

cost. Recent years, however, have shown the progress of integrating a complete radar system into a single chip, which brings down the cost significantly [108]. However, the average cost of a single-chip radar is still higher than other sensors, e.g., ultrasonic. [107].

3.2.6 Overview of FOD/LOD Implementation

A direct comparison of the FOD/LOD solutions can be seen in Tbl. 3.1. It is noticeable that the overall performance of the Qi-standard FOD/LOD system is relatively low compared to other solutions, however, it does have the advantage of easy integration and low cost because it can be part of the IPT system. The low charging power (typically 5-10 W) also allows it to have a less accurate system. For IPT systems designed for higher power and range, it is therefore important to have a more advanced FOD/LOD system. From the table, it can be noticed that the radar-based FOD/LOD offers an overall good performance compared to other external FOD/LOD solutions, especially in terms of robustness. A further investigation of a radar-based FOD/LOD system will be presented in the following chapter.

Table 3.1: FOD/LOD methods comparison

Methods	Accuracy	Speed	Range	Robustness	LOD	Integration	Cost
Q-factor	Low	High	Small	High	✗	Built-in	Low
Efficiency	Low	High	Small	High	✗	Partially built-in	Low
Ultrasonic	Medium	High	Medium	Low	✗	External	Medium
Camera	High	High	Wide	Low	✓	External	Medium
Radar	High	High	Wide	High	✓	External	Medium














TI's proximity sensing technology		Ultrasonic	Optical ToF	mmWave
				
Detection range		0.1 to 10 m	0.01 to 20 m	0.04 to 100+ m
Resolution		Few mm (transducer dependent)	Few mm (optics dependent)	Few mm (range dependent)
Field of view	Narrow to wide	5° to 120°	.15° to 120°	5° to 160°
TI IC current consumption	Active	72 mW to 336 mW	100 µW to 200 mW	0.5 W to 1.5 W
	Standby/sleep	2-9 mW	~80 µW	N/A
Solution/module size		Medium	Small	Large
Aesthetics		Exposure to medium for longer range	Hidden behind dark glass	Penetrates most materials (not metal)
Measuring Medium Speed		Sound	Light	Light
Single sensor system cost (US\$)		\$1.00 - \$3.00	\$1.50 - \$4.00	\$18.00 - \$26.00
Reliable environments	Sunny 	★★★★★	★★★★★	★★★★★
	Smoke/gas 	★★★★☆	★☆☆☆☆	★★★★★
	Pressure 	★★★★☆	★★★★★	★★★★★
	High temperature 	★★★★☆	★★★★★	★★★★★
Target characteristics	Transparent surface 	★★★★★	☆☆☆☆☆	★★★★★
	Liquid/fluid 	★★★★☆	★★★☆☆	★★★★★
	Irregular shape 	★★★★★	★★★★★	★★★★☆
	Light 	★★★★★	★★★★★	★★★★★
	Dark 	★★★★★	★★★☆☆	★★★★★
	Soft 	★★★☆☆	★★★★★	★★★☆☆
Key differentiation		<ul style="list-style-type: none"> • Lowest cost proximity and obstruction detection solution • Effectively detect solid and transparent glass surfaces • Able to detect objects in a smoke/gas-filled environment 	<ul style="list-style-type: none"> • Target localization (up to 3 zones of detection) • Precise long-range distance measurements • External optics enable a highly customizable solution 	<ul style="list-style-type: none"> • Provides range, velocity and angle data • Can penetrate non-metal materials • Intelligent object differentiation • Not effected by environmental conditions

Figure 3.12: TI's Proximity Sensors (ti.com)

Chapter 4

Impedance Reflection FOD/LOD

In the previous chapter, various FOD/LOD methods were discussed and benchmarked. The Q-factor and efficiency measurement FOD/LOD method, although having some advantages of easy integration and relatively low-cost, they also have some limitations, e.g., the FOD could cause false-positive detection and therefore restrict the IPT system's tolerance to misalignment, and the challenges to scale to higher power IPT systems. The other FOD/LOD methods that use sensors, e.g., ultrasonic radar, visible light, also showed some potential to address the limitations of the Qi-standard FOD/LOD methods, however, require externally mounted sensors for the best results. In this chapter, an alternative FOD/LOD method that does not require external sensors is proposed. Such a method is designed to detect foreign objects by only reading the voltage waveform information from the inverter on the transmit side. No communication between the transmit and receive side is required. The author's main contribution in this chapter is the first (based on the author's best knowledge and patent search) mention of using such voltage waveform information to perform object detection on a wireless power system, and the first to develop a FOD/LOD system that demonstrates the capability of the proposed system. The further exploration of reflected impedance estimation using machine learning was also the first publication [109].

The design of an IPT system that operates at MHz frequencies often relies on soft-switching resonant converters at both ends to achieve good end-to-end efficiency. The behaviour of these

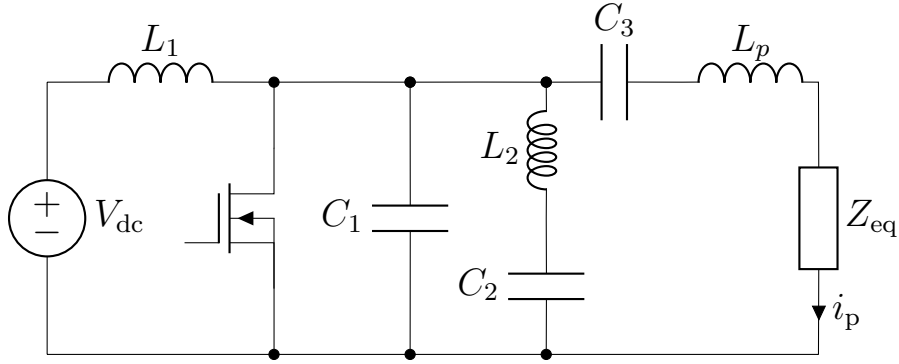


Figure 4.1: Class EF inverter circuit topology driving an inductively coupled reflected impedance (Z_{eq}).

converters depends on how the two ends of the system are coupled. Often, the receiving side is modelled with a voltage or current source representing the effect produced by the alternating magnetic field on the receive coil; and similarly, a reflected load models the effect produced by the receive side on the transmit side.

Employing this modelling principle, broadly described for WPT in [7], allows defining a range of operations for both the reflected load at the transmit side and the voltage (or current) source at the receive side. Defining this range of operation allows the system to be optimised for variable coupling and loading conditions [80]. An example of a multi-MHz IPT system that is optimised for variable coupling and load can be found in [78], where a drone without a battery was wirelessly powered at a broad range of coupling and loading conditions by designing the resonant converters at both ends of the system for those ranges. Knowledge of the reflected impedance was key in that work to allow for spatial freedom and variable power demand since the reflected impedance, not always purely resistive, had to be confined to the range of tolerance of the inverter. The work presented here investigates changes in the drain-source voltage waveforms of the inductively coupled circuits under different operating conditions, i.e., the wireless power receiver and foreign objects loading conditions.

4.0.1 Load-independent Class EF Inverter

The Class EF inverter, a single-switch resonant topology shown in Fig. 4.1, allows for load-independent tuning by selecting the values of the passive components following the guidelines

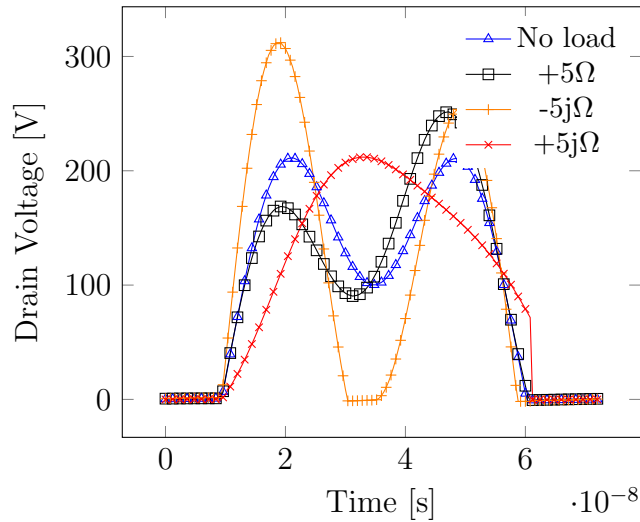


Figure 4.2: Theoretical drain-source voltage waveform under various loading conditions

formulated in [79]. The solutions that are considered load-independent, achieve zero-voltage switching (ZVS) over the entire resistive load range, and in addition, when employed on an IPT system, the amplitude of the transmit coil current is load-independent and defined by V_{dc} .

The load-independent feature can be noticed in the drain voltage waveforms in Fig. 4.2. For the cases of no-load and maximum resistive load ($+5\ \Omega$), the turn-on voltage inherently converges to zero and therefore achieves ZVS. Reflected reactances, however, detune the inverter and affect the load-independent operation. As can be seen in Fig. 4.2, the shape of the waveform changes depending on the type of load coupled. Inductive, capacitive and resistive loads affect the waveforms in different forms which are identifiable. A perfectly tuned wireless power receiver seen on the transmit side is equivalent to a series resistive load, while a de-tuned receiver, or other objects that are coupled to the transmit coil would reflect either capacitive or inductive impedance back to the transmit side.

4.0.2 Reflected Impedance Estimation

The drain voltage waveforms in Fig. 4.2 suggest the possibility of estimating the reflected impedance on an IPT transmitter that uses the load-independent Class EF inverter. The drain voltage is the signal chosen in this study not only because of its clear load dependence, but also

because, first, ZVS (or non-ZVS) operation can be identified; and second, the topology has a capacitance between the drain and the source of the transistor which absorbs the capacitance of the probe, making it relatively easy to measure without affecting the tuning of the system.

The proposed method consists of gathering the drain voltage waveform signals with different and well-characterised loads, to then train a regression model that can recognise these loading conditions. The performances of the model are evaluated by using untrained data. To verify the proposed method, a circuit simulation model is built to gather the waveform data, and to train the estimation model. The component values for the circuit simulation as well as the actual circuit for later verification are shown in Tbl. 4.1.

Circuit Simulation

The proposed technique was first verified by simulating a load-independent Class EF inverter operating under different loading conditions. The parameters used are described in Tbl. 4.1.

The inverter was simulated with a reflected resistance ranging from 0 to 10 Ω , and a reflected reactance from -5 to 5 Ω , both with steps of 100 m Ω . The drain-voltage waveforms were recorded when the system reached a steady state for each reflected load and then labelled accordingly. These data were then used to train and verify the model.

Table 4.1: Simulation and Experimental Component Values

Parameter	Value (simulation)	Value (experiments)
V_{dc}	100 V	100 V
C_1	279 pF	156 pF + C_{Oss}
C_2	214 pF	176 pF
C_3	143 pF	130 pF
L_1	80 μ H	80 μ H
L_2	231 nH	267 nH
L_p	1130 nH	1118 nH

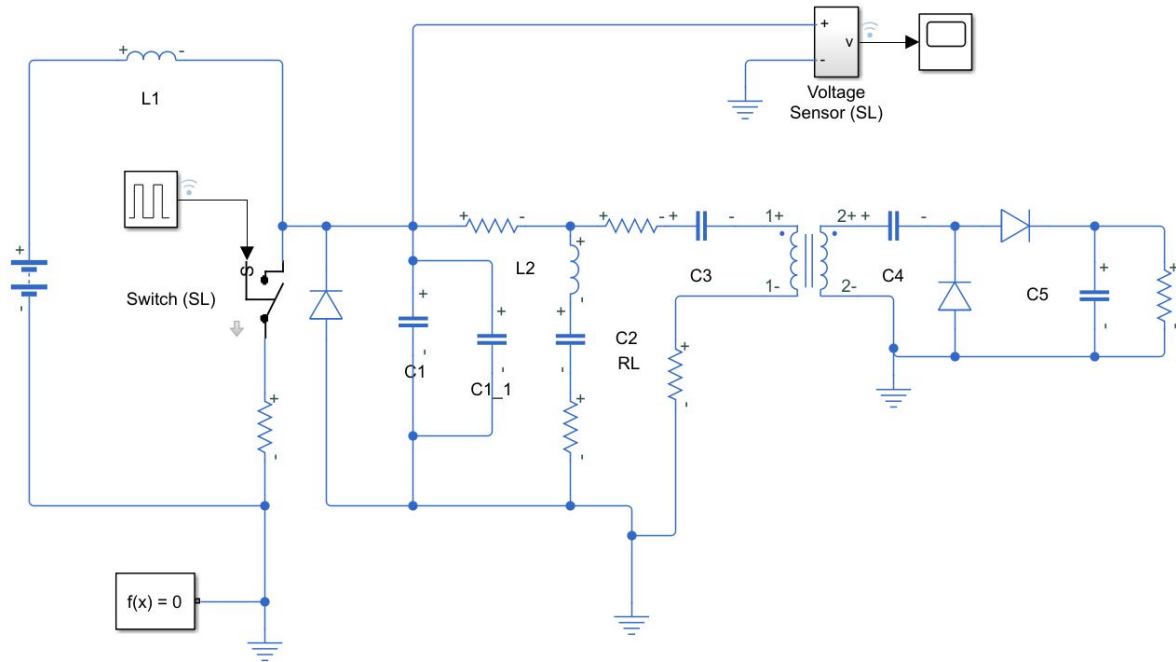


Figure 4.3: Class EF circuit simulation on Matlab Simulink

Data Acquisition and Augmentation

Before the training process, data were required to be prepared and configured. A MATLAB simulink circuit is used to collect the drain-source voltage waveform data, as shown in Fig. 4.3. The result output setting was used to select the sampling rate and data resolution. To compare the simulation and the experimental results, the sampling rate and resolution of the simulations were configured to be the same as the Teledyne LeCroy HDO4034 oscilloscope, which is 2.5 GSPS, and 12 bit respectively. A full cycle of the drain voltage waveform was captured one hundred times for each value of equivalent reflected impedance. Additionally, random phase shifts ($0 - 2\pi$) and noise sources ($\pm 1\%$, as observed from the oscilloscope) were added to the simulated waveform signals. The reason for applying random phase shift to the signals is to simplify the data capturing process for future implementation, especially with low-cost hardware. The extra noise added was to improve the robustness of the trained model.

Model Training and Evaluation

For simple estimation problems with a small number of independent variables, one can use linear or other regression methods to build a statistic model, and to infer the results for future data. However, for this particular problem, since the number of variables is relatively large (a full cycle of the waveform has approx. 185 data points) and some of them can be dependent to each other, a statistical regression method can be difficult to implement and may not be the most suitable approach to the problem. Thanks to the ever-growing computing power of the silicon chips, the long proposed but not widely implemented “machine learning” techniques have been resurfaced over the recent years [110] [111]. Unlike typical statistical methods that focus heavily on the logical relationship between the input data and the inference results, machine learning techniques utilise the data and computing power to “train” a model with an ultimate goal of achieving highest accuracy. Though such techniques has only been widely used in recent years, it has gained its credibility of solving many real-world problems that are regarded as “impossible”. For example, it is arguably easy (with enough data and computing power) to train a machine learning model to recognise an object or human face. However, such problem would be extremely complicated or even impossible to use traditional statistical models, given that the number of variables in a simple 1920*1080 pixel RGB image can easily exceed 6 millions. Even if one has managed to build statistical model to recognise an object from an image, it may not be able to recognise again if the image is somehow distorted (e.g. cropped/rotated/translated etc.). Similarly, for this problem, since ideally the waveform should be obtained with low-cost hardware that could not ensure the sampled waveform is always triggered at the exact same time, and typical regression models would have weights assigned specifically to each data points of the waveform, which makes traditional statistical models difficult to perform prediction without any post-processing of the sampled data. Even some machine learning techniques (e.g. SVM) are not able to handle waveform data with random phase shifts. It is, however, possible to approach this problem from the frequency domain, which is then possible to use typical statistical methods to make a prediction model based on the harmonic components of the signal. Such an approach has also been researched by members of the Wireless Power Lab in Imperial College London [112]. This thesis mainly

focuses on the time-domain analysis of the problem, and therefore machine learning techniques are used instead.

Over the recent years, one of the machine learning tools - neural network, especially deep neural network - haven shown its capability of recognising patterns of images or other forms of data, regardless of the pattern's position, scale, rotation or other forms of data distortion [113] [114]. One classic and popular example of this is the hand written digit recognition based on the Modified National Institute of Standards and Technology (MNIST) database [115,116]. With numerous methods in [115], the Convolutional Neural Network (CNN) showed the highest accuracy of recognising those hand-written digits. And because of this, CNN is chosen as the candidate to estimate the reflected impedance. Based on examples in [115], a customised regression CNN model was designed, as shown in Tbl. 4.2. The number of layers and their configurations were tuned manually to achieve a higher estimation accuracy, with numerous train-and-test cycles.

Table 4.2: Network Layers

Layer No.	Layer Name	Details
1	Image Input	15x15x1 images with 'zerocenter'
2	Convolution	9 6x6 convolutions with stride ones and padding ones
3	Batch Normalisation	Batch normalisation
4	ReLU	ReLU
5	Max Pooling	2x2 max pooling with stride ones and padding zeros
6	Convolution	9 3x3 convolutions with stride ones and padding ones
7	Batch Normalisation	Batch normalisation
8	ReLU	ReLU
9	Max Pooling	2x2 max pooling with stride ones and padding zeros
10	Convolution	12 3x3 convolutions with stride ones and padding twos
11	Batch Normalisation	Batch normalisation
12	ReLU	ReLU
13	Convolution	12 3x3 convolutions with stride ones and padding twos
14	Batch Normalisation	Batch normalisation
15	ReLU	ReLU
16	Convolution	9 3x3 convolutions with stride ones and padding ones
17	Batch Normalisation	Batch normalisation
18	ReLU	ReLU
19	Max Pooling	2x2 max pooling with stride ones and padding zeros
20	Fully Connected	1 fully connected layer
21	Regression Output	mean-squared-error

Based this CNN model, the training dataset were reshaped into 15*15 matrix padded with

zeros. The dataset were also divided into three subsets: 85 % of the training data were used to train the CNN model, 10 % as the validation data set during the training process, and the last 5 % as the final test to evaluate the performance of the trained model.

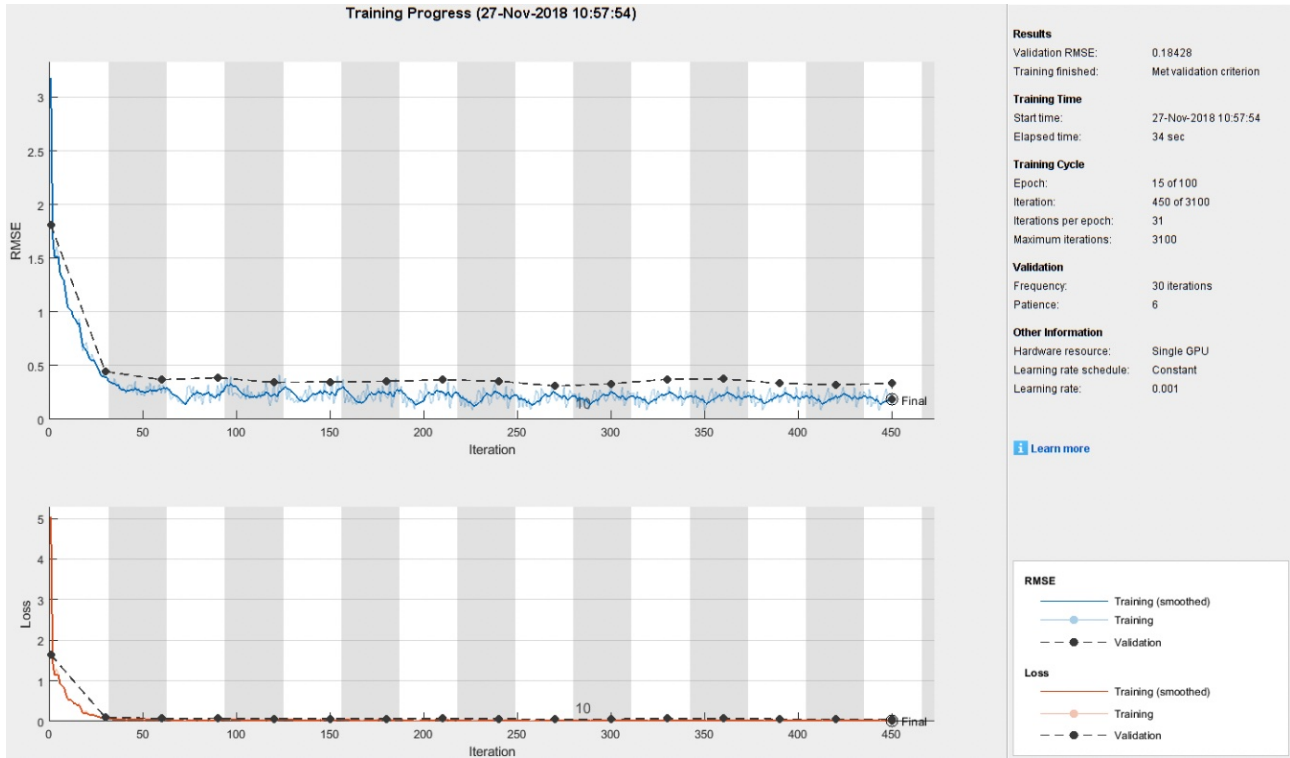


Figure 4.4: CNN estimation model training process

The training configuration and training process are shown in Fig. 4.4. The trained model reported a root-mean-square error of 0.18428 based on the validation dataset. By implementing this model, the estimation results of the test dataset and the actual results can be seen in Fig. 4.6. The estimation accuracy (coefficient of determination) is 0.9942 for the real part of the impedance, and is 0.9905 for the imaginary part, which indicates that such impedance estimation method purely based on the switching device’s voltage waveform is possible. Though with such high accuracy, there are still many improvements can be made to increase it’s accuracy and to reduce the complexity of the model. Since the main focuses of here is to prove the suggested estimation method, and the performance of the trained model is satisfying for its purpose, let’s continue to test it with a real-world IPT system.

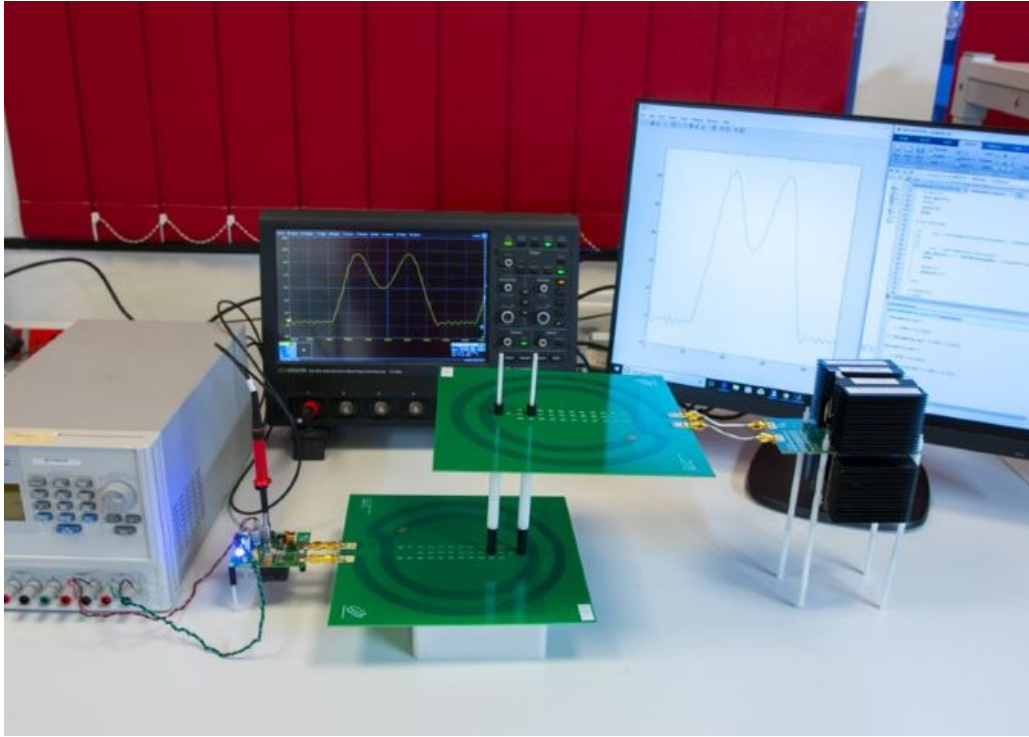


Figure 4.5: Photograph of the experimental setup.

4.0.3 Experimental Verification

Having gained the confidence from the simulated circuit that with machine learning techniques it is possible to estimate the reflected impedance solely based on the drain-source voltage waveform, it would be interesting to see how this model performs with a real-world IPT system. To do this, a similar approach was done on a real IPT setup capable of powering a load of up to 150 W at 13.56 MHz. A photograph of the experimental setup can be seen in Fig. 4.5 and the design values of the inverter implemented can be found in Tbl. 4.1. The coils and the inductively coupled load that used to train the model are described in [117].

The reflected load on the transmit side was altered by changing the coupling and the receive side capacitance that resonates with the coil. As can be seen in Fig. 4.5, this systems allows for a precise separation and alignment, which was characterised in [117]. Data were obtained for coil separations of 12-20 cm with steps of 1 cm, and the tuning of the receive side was changed as done in [117]. Four loads which reflect a negative reactance and three which reflect a positive reactance were used at the coil separations mentioned. The reflected reactance allowed by this setup was roughly from -2 to 2Ω , and the reflected resistance from 0 to 8Ω .

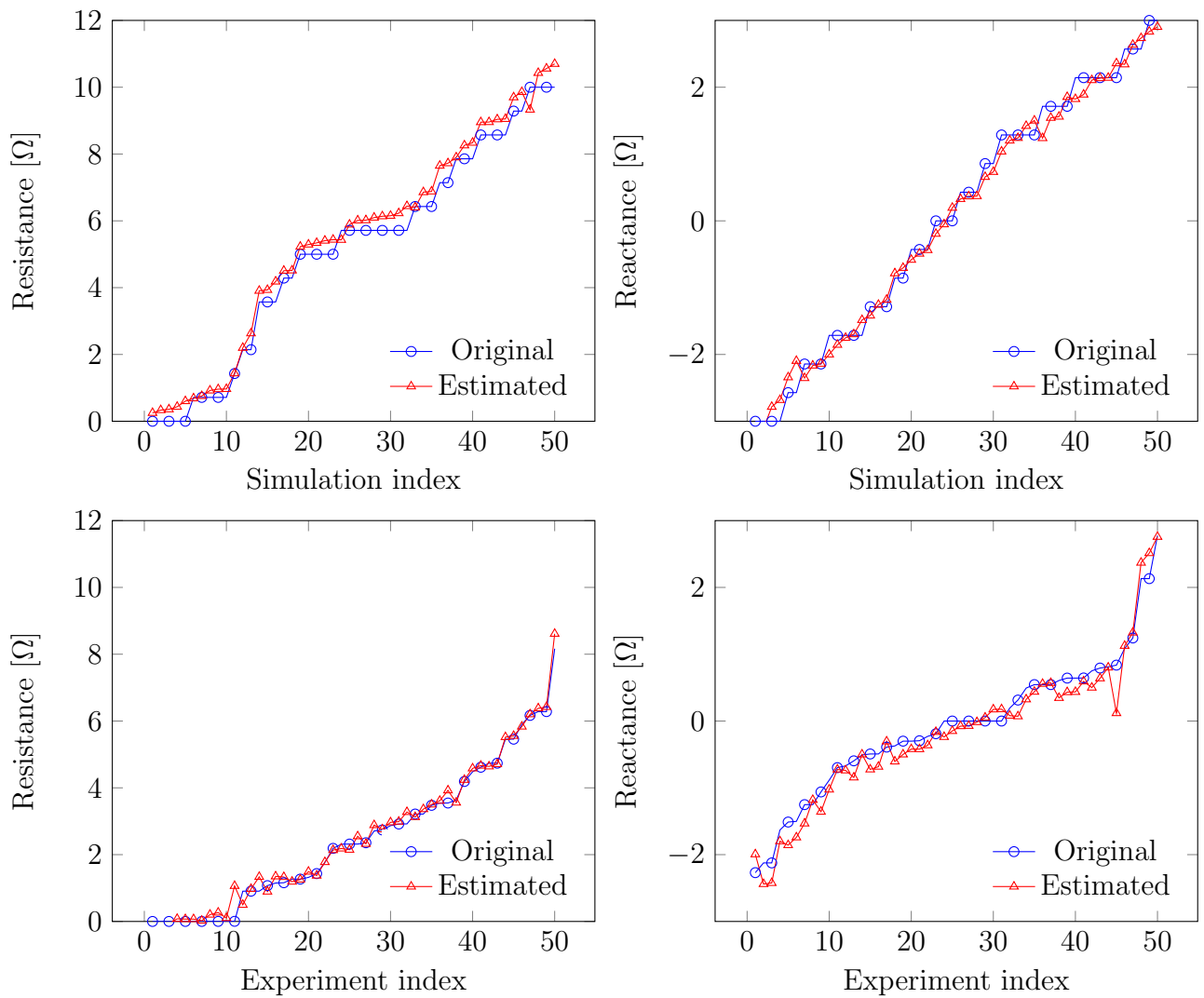


Figure 4.6: Impedance estimation model results from a simulated and an experimental environment.

The load estimation results are shown in Fig. 4.6. The estimation accuracy (coefficient of determination) is 0.9899 for the real part of the impedance, and is 0.9743 for the imaginary part.

4.1 Impedance Reflection FOD/LOD

With this reflected impedance estimation tool, it is then possible to perform object detection based on the reflected impedance, completely on the transmit side of an IPT system. As discussed in chapter 1, a perfectly tuned wireless power receiver with pure resistive load would only reflect the real impedance or resistance on the transmitter side. Foreign/ living objects are not tuned to the operation frequency of the IPT system, therefore, are more likely to reflect reactance back to the transmit side. By using the reflected impedance estimator, this reflected reactance value can be easily determined and compared with a predefined threshold to detect foreign/living objects. Tbl. 4.3 shows the estimated impedance of some common objects including the IPT receiver placed 5 cm away from the transmit coil. When there's nothing placed on the coil, both reflected resistance and reactance stays around zero, while a tuned receiver with an AC load only reflected resistance back to the transmit side, which is as expected. The slight increase in reactance (from 0.05Ω to 0.09Ω) could be caused by the imperfect tuning of the IPT receiver, or due to the error of the estimation model. The other foreign objects, in general, reflected more reactance than resistance, since they are not "tuned" to the operating frequency of the IPT system. Depends on the dimension and the material of the objects, some objects would behave more inductively while others are more capacitive, as shown in the table. Metal objects tend to reflect negative reactance when coupled to the IPT system, and the larger the objects, the higher the reflected value, which is as expected. The minimum reflected resistance of the metal objects also agrees with the observation that common metal objects do not heat up when placed on a high-frequency IPT system, as discussed in Chapter 1. The most interesting object tested was the compact disc, since it actually heats up on a high-frequency IPT system. From Tbl. 4.3 it can be seen that a CD would reflect both resistance and reactance, which explains the observation. Overall, from the test objects, it is possible to set a threshold of the absolute value of the reactance to distinguish between an IPT receiver and other objects. And the value of this threshold can vary to change the sensitivity of detection for different applications.

It would be interesting to see how such an FOD method compares to the other FOD/LOD

Table 4.3: Estimated Impedance of FO and IPT Receiver (5 cm to the coil)

Coupled objects	Estimated Resistance	Estimated Reactance
No load	0.02 Ω	0.05 Ω
IPT receiver (AC load)	5.20 Ω	0.09 Ω
Copper sheet (5*5*0.01 cm)	0.10 Ω	-0.81 Ω
Key	0.05 Ω	-0.24 Ω
50p coin	0.04 Ω	-0.19 Ω
Compact disc	0.45 Ω	0.34 Ω

methods discussed in the previous chapter. Tbl. 4.4 shows how this FOD/LOD method is positioned in the same chart as the one in chapter 3. Comparing with the FOD methods implemented in the Qi-standard, the proposed method performs better or the same in every metric except cost. This is because such a method relies on a high-speed oscilloscope and a computer that runs MATLAB to perform object detection. The next section, therefore, discusses approaches to replace such a setup with lower-cost hardware.

Table 4.4: FOD/LOD methods comparison

FOD/LOD	Accuracy	Speed	Range	Robustness	LOD	Integration	Cost
Q-factor	Low	High	Small	High	✗	Built-in	Low
Efficiency	Low	High	Small	High	✗	Partially built-in	Low
ultrasonic	Medium	High	Medium	Low	✗	External	Medium
Camera	High	High	Wide	Low	✓	External	Medium
Radar	High	High	Wide	High	✓	External	Medium
Proposed	High	High	Medium	High	✗	Built-in	High

4.2 Implementation on Low-cost Hardware

While the proposed reflected impedance FOD technique has shown some promise in terms of detection accuracy, the hardware used in the test were based on expensive oscilloscope and a desktop computer, which is not practical to be used in real-world applications. Therefore, the work reported in this section proposes some techniques to reduce the implementation cost of the FOD method introduced above. The implementation cost can be divided into two parts:

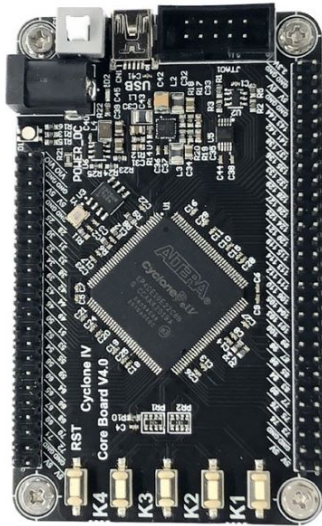


Figure 4.7: Altera EP4CE10 EVM



Figure 4.8: AD9226 ADC Module

the data acquisition part; and the data processing part. An approach to reduce the cost for each part is discussed as following.

4.2.1 Sub-sampling

The data capturing process for the previous FOD experiments were implemented with a 2.5 GS/S oscilloscope. A higher sampling rate generally increases the quality of data, but it also increases the cost and implementation complexity of the hardware. A slower sampling rate could be used to reduce the cost of the ADC. However, lowering the sampling rate means fewer data points collected per cycle of the waveform, which would cause the prediction accuracy to decrease further. One solution is to implement a “sub-sampling” technique, that is, to sample a signal at a frequency that is less than the Nyquist rate [118]. Since the signal of interest has a fixed frequency, it is possible to sample the signal at a frequency that is close but not equal to the signal frequency, and by selecting the frequency carefully, it is possible to combine the sampled data points to reconstruct the original signal shape. By implementing this technique, a lower-cost ADC could be used while still obtaining a reasonable number of data points to reconstruct the drain-source voltage waveform. To verify this idea, an experiment is showcased in the following section.

Experiment Setup

For demonstration purposes, the selected hardware for this experiment is chosen to be simple to implement and could be further developed to be integrated into the IPT system. The data processing unit chosen for this experiment is an Altera Cyclone IV EP4CE10 FPGA development module, as shown in Fig. 4.7. The reason for using FPGA instead of MCU is only to simplify the development process as it is easier to configure different clocks for various ADC interfaces. The debugging tool also offers a simple way to visualise the sampled data from the ADC, as will be presented in the result section. The ADC module (Fig. 4.8) is based on AD9226 chip from Analog Devices [119]. The ADC has a maximum sampling rate of 65 MSPS at 12 bit. Note that in this experiment, the sampling frequency is changed to a lower value to verify the sub-sampling idea. The input voltage range for the ADC module is between -5 V to +5 V.

The experiment setup is shown in Fig. 4.9. The ADC module is connected to the FPGA development board. A Tektronics signal generator is used to generate the desired frequency for testing. The ADC and the signal generator are connected via a SMA to BNC cable. Quartus II V13 software is running on a desktop computer to communicate with the FPGA device via an USB interface. a 12 V power cable is used to power the FPGA development board.

Two types of signals are generated from the clock generator for testing: a 6.67 MHz sine wave signal with 9 V amplitude, 0 V offset (Fig. 4.10), and a 6.67 MHz square wave with 9 V amplitude, 0 V offset (Fig. 4.11). The input range of the ADC module is between -5 V and +5 V so the signals are within the operation range of the ADC module. The ADC sampling rate is configured on the FPGA at 6.78 MHz. The signals captured are showing in Fig. 4.12 and Fig. 4.13 respectively.

Results and Next Steps

The result of the ADC captured data is displayed using the Signal Tap II Logic Analyser, which is part of the Quartus II V13 software package. Fig. 4.12 shows the captured waveform from

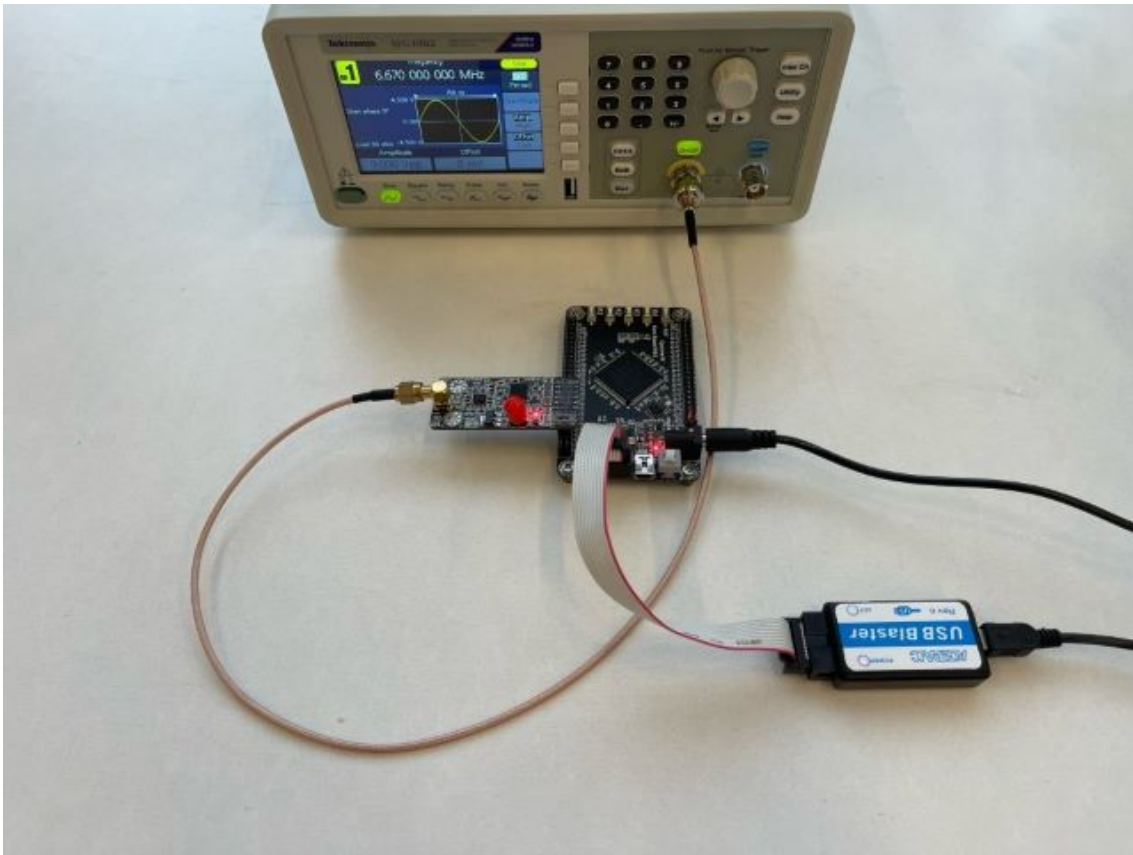


Figure 4.9: Sub-sampling Test Setup

the Signal Tap II Logic Analyser, it can be seen that although the sampling frequency is almost the same as the signal's fundamental frequency, the original shape of the waveform can still be reconstructed. Fig. 4.13 shows the captured square wave using the same technique. Although with some distortion, the original information of the square wave is mostly restored.

In summary, the purpose of this work is simply to suggest a possible approach to reduce the hardware requirement for the FOD/LOD method based on the drain-source waveform information of the inverter. By implementing the sub-sampling technique, the sampling hardware cost can be reduced significantly than high-speed instrumentation methods. However, to eventually implement such a method would require the actual HF-IPT system and an additional circuit design (e.g., a compensation network) to scale down the drain-source voltage signal before feeding directly into the ADC. Additional filters may also be used to reduce noise and interference.

With the limited resources due to COVID-19 interruption, this experiment could only be done without accessing to the IPT system, which leaves the remaining part of this work for future

Pi Zero board does not have an ADC, an external ADC module was designed to perform the sampling. The ADC chip selected is the ADC12010 from Texas Instruments, the data sheet can be accessed from [121]. The separate ADC module is shown in Fig. 4.14. The module was also designed to have the same dimensions as the Raspberry Pi Zero itself for easy integration. The signal to be captured is transmitted to the ADC module via a SMA cable, this makes it easier to test with a signal generator during development.

With the hardware setup ready, the rest of the development was completely on the Raspberry Pi. To avoid permission issues in Linux, all processes described below were coded as a Linux kernel module. Before heading straight to disable all interrupts of the Raspberry Pi and perform the sampling, some preparation work is needed to ensure the “real-time” operation. Like most modern computers, the Raspberry Pi also has automatic throttling to reduce energy consumption and therefore avoid overheating of the device itself [122]. This throttling process would adjust the CPU clock frequency based on the CPU usage and temperature of the device. If the frequency change occurs during the sampling process, it could cause wrong data to be captured. It is therefore, necessary to configure a constant CPU clock during the capture process.

With the CPU clock configured, the next step is to disable all interrupts, including system interrupts, e.g., I/O, file system, network tasks, etc.. This step can be done by executing the following code.

```
local_irq_disable()  
local_fiq_disable()
```

To start sampling, a sampling clock is needed for the ADC. This step is done by using the phase-lock loop module of the Raspberry Pi. This can be done with the following code.

```
//Set a clock signal on Pin 4  
struct bcm2835_peripheral *p=&myclock;  
p->addr=(uint32_t *)ioremap(CLOCK_BASE, 41*4);
```

```

INP_GPIO(4);
SET_GPIO_ALT(4, 0);

int speed_id = 6; //1 for 19Mhz or 6 for 500 MHz
*(myclock.addr+28)=0x5A000000 | speed_id; //clock off

//Wait untill clock is no longer busy (BUSY flag)
while (*(myclock.addr+28) & GZ_CLK_BUSY) {};
//Set divider //divide by 50
*(myclock.addr+29)= 0x5A000000 | (0x32 << 12) | 0;
*(myclock.addr+28)=0x5A000010 | speed_id; //Turn clock on

```

More details regarding the ADC module and the triggering of the sampling process are well documented in [120]. With the sampled data captured, gnuplot, a Python data plotting tool, is used to display the data on a Raspberry Pi. Fig. 4.15 shows an example of a 50.01 MHz sine wave captured by a Raspberry Pi using a 10 MHz ADC. It can be seen that the original waveform shape is well reserved on this plot.

Overall, this work is merely to demonstrate another potential technique to reduce the implementation cost of the FOD/LOD method introduced in this chapter. Similar to the sub-sampling technique, the final integration of this work into the IPT system was not completed due to the lack of lab access.

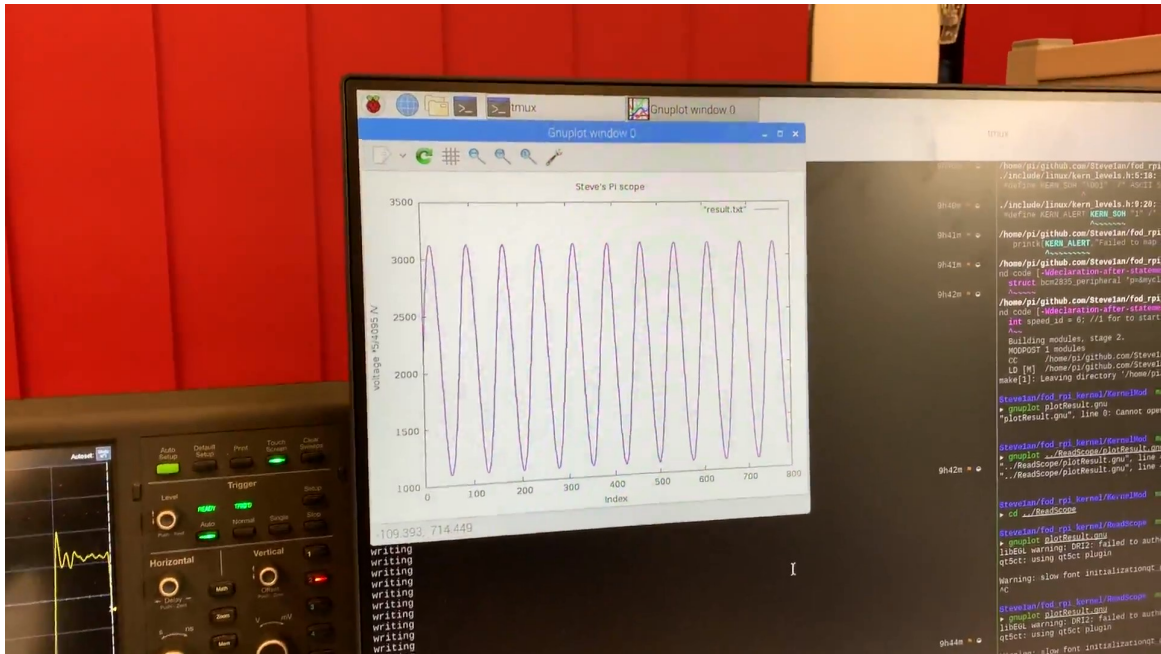


Figure 4.15: Sub-sampling a 50.01 MHz Signal with a 10 MHz ADC

Chapter 5

mmWave Radar-based FOD/LOD System

Although the reflected impedance-based object detection technique introduced above outperforms some of the methods used by Qi-standard in terms of accuracy, range, etc., it is still not a perfect system as it is not able to detect live objects. For some high-power IPT applications, LOD may be required to ensure the EM exposure does not exceed the safety limits. Optical-based detection systems, as discussed in chapter 3, could be used to recognise humans or other live objects. However, it also suffers from poor robustness as the sensor could easily fail due to dust/snow cover. In this chapter, a mmWave radar-based FOD/LOD technique is introduced as an alternative solution to fill the gap. Thanks to its particular frequency range (GHz), the mmWave radar sensor is able to see through various types of materials (e.g., plastic, dry wall, etc.) and still sensitive enough to detect thin and small objects e.g., a piece of paper [103]. Moreover, with a multi-Tx and Rx design, a mmWave radar sensor could also detect the angle of the object, and even to perform object classification [123, 124]. In this chapter, a mmWave radar-based FOD/LOD system is designed and developed. The author's contribution in this chapter includes a foreign/ live object recognition method by using the state-of-the-art mmWave radar sensor. To the author's best knowledge, such application was the first mentioned FOD method for HF-IPT systems. With sufficient data and appropriate training, the

proposed method is able to recognise six different charging scenarios with an accuracy up to 96%

5.1 Sensor Selection

To design a mmWave radar-based FOD/LOD system, a suitable radar sensor is needed. In the automobile industry, long range mmWave radar is commonly used to measure the distance of vehicles in front and provide collision warnings [102]. However, for wireless charging applications, the mmWave radar does not need to detect objects over a hundred meters away. Instead, the field of view, size and cost are more important. Based on various mmWave radar sensors available, the TI IWR6843AOP is selected as this module has a wide field of view angle of 130 degrees, and its integrated antenna-on-package design could also help reduce the cost of the final application [125]. The evaluation module (Fig. 5.1) of this mmWave radar is used to simplify the development process [126].



Figure 5.1: IWR6843AOP Evaluation Module (ti.com)

5.2 General Object Detection

Before developing the FOD/LOD system for the IPT system, it is necessary to evaluate the basic object detection of the mmWave radar sensor. TI's mmWave radar sensor typically requires a

configuration before running, the configuration tells the sensor what kind of information needs to be obtained and how fast does it need to output the information etc [127]. An example of this configuration in TI's mmWave demo visualiser is shown in Fig. 5.2. This configuration requests various types of information from the sensor including: scatter plot, range azimuth heat map, range profile, etc. This information was obtained at 5 frames per second. The frame rate is limited by the bandwidth of the serial interface between the sensor and the host computer, higher frame rate is possible by using a faster interface or if less information is requested from the sensor.

The image shows a web-based configuration interface for a mmWave sensor. It is divided into three main sections: Setup Details, Scene Selection, and Plot Selection.

Setup Details:

- Platform: xWR68xx_AOP
- SDK version (*): 3.5
- Antenna Config (Azimuth Res - deg): 4Rx,3Tx(30 Azim 30 Elev)

Desirable Configuration:

- Best Range Resolution
- Frequency Band (GHz): 60-64
- Calibration Data Save/Restore: None (with a value of 0x1F0000)

Scene Selection:

- Frame Rate (fps): Slider from 1 to 30, set to 5.
- Range Resolution (m): Slider from 0.039 to 0.047, set to 0.044.
- Maximum Unambiguous Range (m): Slider from 3.95 to 18.02, set to 9.02.
- Maximum Radial Velocity (m/s): Slider from 0.21 to 6.39, set to 1.
- Radial Velocity Resolution (m/s): Dropdown menu set to 0.13.

Plot Selection:

- Scatter Plot
- Range Profile
- Noise Profile
- Range Azimuth Heat Map
- Range Doppler Heat Map
- Statistics

At the bottom, there are three buttons: SEND CONFIG TO MMWAVE DEVICE, SAVE CONFIG TO PC, and RESET SELECTION.

Figure 5.2: mmWave configuration (dev.ti.com)

With the configuration information sent, the sensor then returns the detection results in various formats. The most straightforward result is the 3D scatter point plot, which is the detected

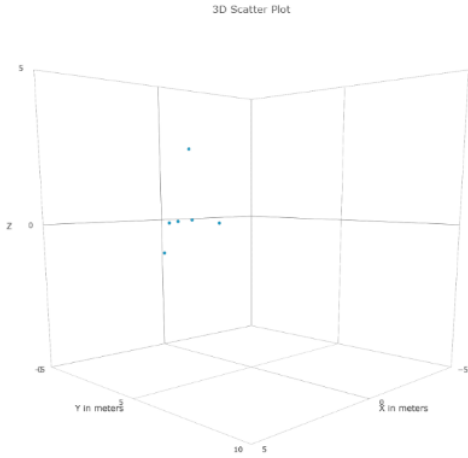


Figure 5.3: 3D Scatter Plot

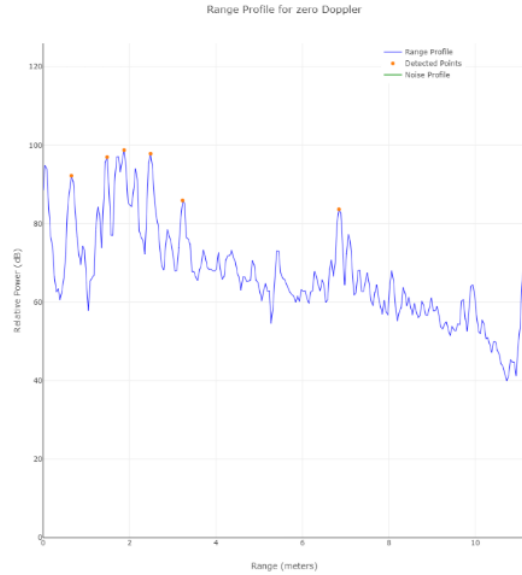


Figure 5.4: Range Profile Plot

points with 3D coordinates, as shown in Fig. 5.3. Another useful information that can be obtained from the sensor is the range profile (Fig. 5.4), which shows the radar reflection strength against distance. The mmWave radar could also capture the motion of objects in the detection range, as shown in Fig. 5.5. Moreover, with some data processing, a heat map could also be generated to indicate the reflection strength at different distances and angles, as shown in Fig. 5.6.

While all information obtained from the mmWave radar can be used to detect foreign objects, some are more sensitive to static objects while others may be more sensitive to motion. The most suitable method would depend on the actual application. In this chapter, a real-world IPT application is used as the test setup for the FOD/LOD system to be designed.

5.3 System Overview

In this chapter, an 110W e-scooter wireless charging system developed by the team from the Wireless Power Lab, Imperial College London is used as the target application for the mmWave FOD/LOD system. More details of this IPT system can be accessed in [128]. The setup of this e-scooter IPT system is shown in Fig. 5.8. This system is capable of delivering 110W

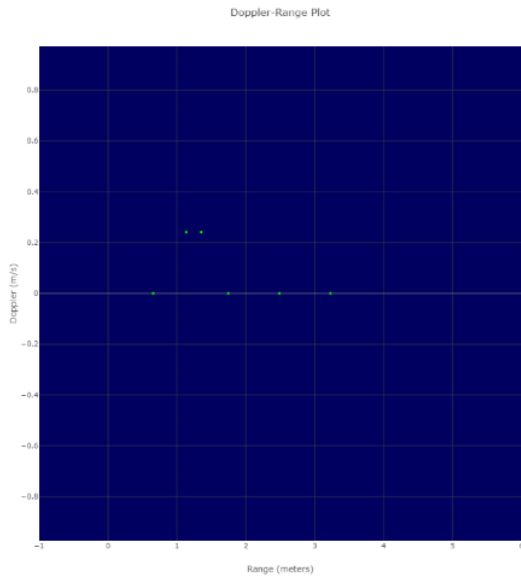


Figure 5.5: Range Doppler Plot

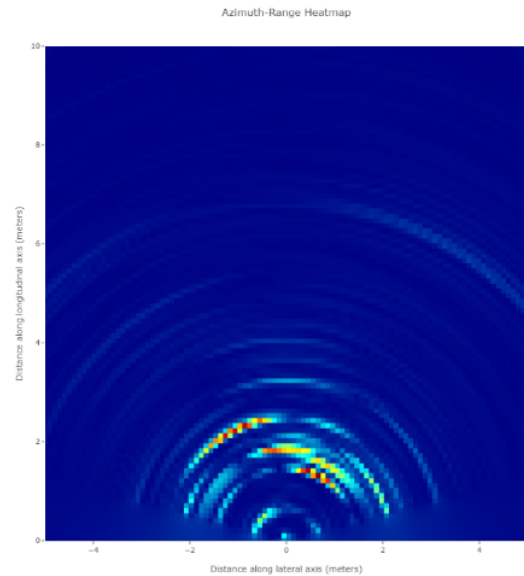


Figure 5.6: Azimuth-Range Heatmap Plot

power to charge the e-scooter with a tolerance to misalignment of 20 cm. With these technical specifications determined, the safety requirements of such a setup could then be measured or simulated based on the IEEE or ICNIRP safety guidelines, as discussed in chapter 1. As such safety requirements could vary based on different standards or guidelines, the detection range of the safety system designed should be easy to configure.

The overall system design of the mmWave-radar based FOD/LOD system together with the IPT system is shown in Fig. 5.7. It can be seen that the mmWave radar-based FOD/LOD system is an external system to the IPT system and can operate and to be developed independently.

5.4 FOD/LOD by Zone Occupancy

Based on the e-scooter IPT application, one approach to perform live/foreign object detection is to mount the mmWave radar sensor to the docking frame on the side of the e-scooters, where the sensor faces the e-scooters to detect live/foreign objects. Since both scooters and other objects can be detected by the mmWave radar sensor, some postprocessing is needed to distinguish them. The 3D scatter plot result provides the location information of the detected objects, one could define a zone of interest using 3D coordinates to exclude the scooter while

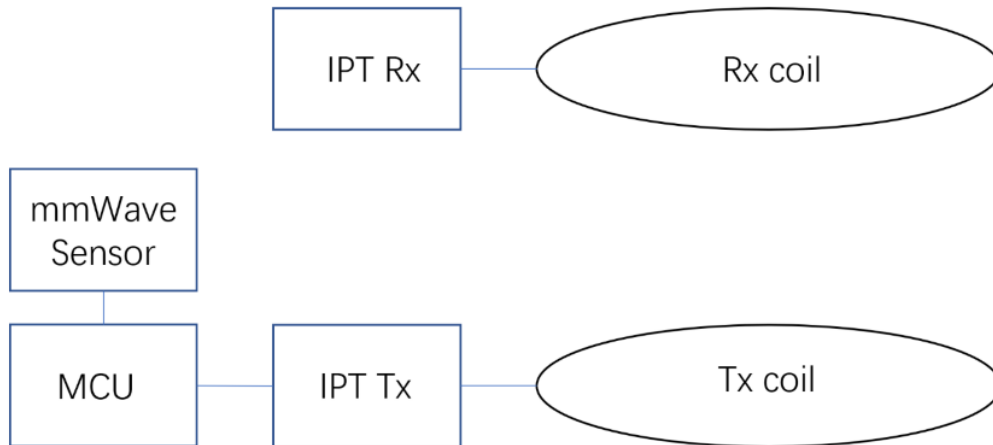


Figure 5.7: System Overview

still be able to detect objects within the zone of interest.

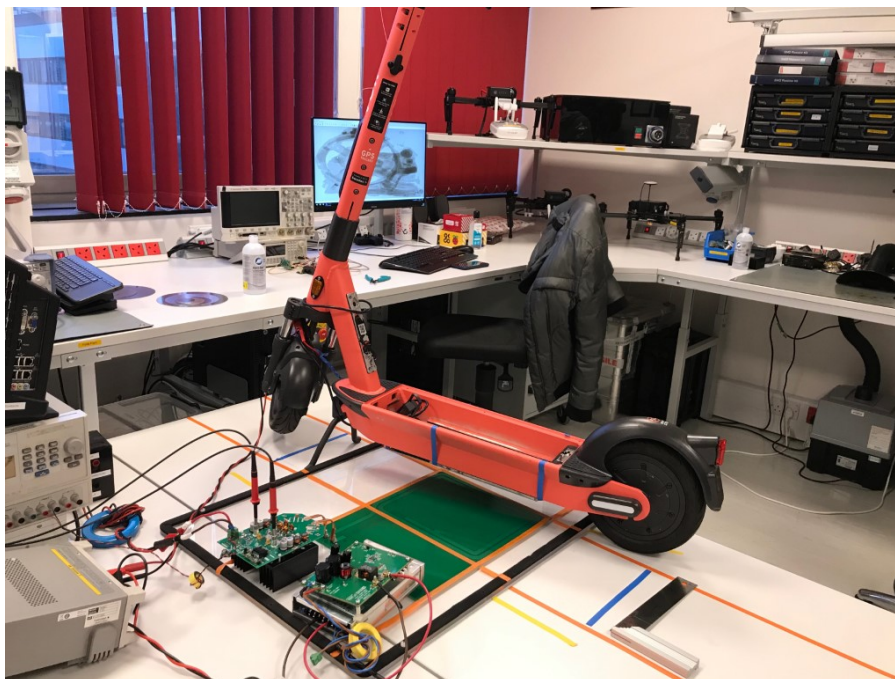


Figure 5.8: E-scooter IPT setup (Christopher Kwan)

To indicate the detection results, a Raspberry Pi 4 is used to process the detection results from the mmWave radar sensor, a LED light is used when objects are detected within the zone of interest. Fig. 5.9 shows when nothing is detected, with a green LED light as the indicator. Fig. 5.10 shows that the sensor is seeing a person approaching to the detection zone with a blue LED light. Fig. 5.11 and Fig. 5.12 both detected the person in range, even when the person is



Figure 5.9: Nothing



Figure 5.10: A person approaching

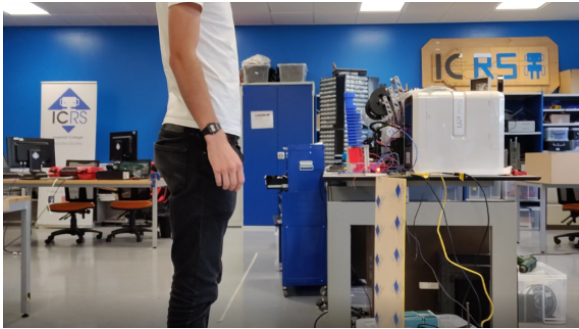


Figure 5.11: A person in detection range

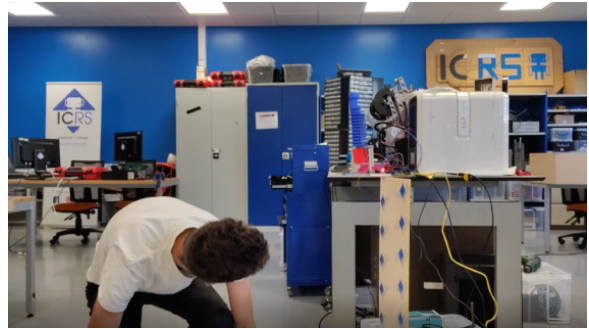


Figure 5.12: A person squatting down

squatting down (Photo taken by Alexander Aujla-Jones). A test video can be viewed at [129], credit to Alexander Aujla-Jones.

This FOD/LOD method by zone occupancy shows a simple but fast FOD/LOD implementation using a mmWave radar sensor. However, this FOD/LOD method does have some disadvantages, e.g., it is unable to distinguish between intended objects (e-scooters) and unintended objects. This method could also be triggered by unharmed foreign objects, e.g., a piece of paper. The following section will discuss a more sophisticated detection method based on the mmWave radar sensor.

5.5 Object classification

The FOD/LOD by occupancy method is a rather basic FOD/LOD method and it might not be sufficient for many IPT applications. This section explores a more advanced detection method by implementing object classification based on mmWave radar sensors. By classifying different objects, the system could better instruct the IPT system to turn off and turn on the wireless

charging. Performing object classification based on mmWave radar sensors is not originated from this work, there have been various publications of implementing for applications, e.g., self-driving vehicles [123] [130]. However, to the author's best knowledge, at the time of writing this thesis, there had been no publication of implementing mmWave radar classification for wireless charging applications. In addition, with the price of single chip radar being more and more friendly [125], such sensor is becoming more practical for lower cost applications.

To simplify the development, only one e-scooter IPT system is used, and the sensor is mounted closer to the scooter to better see if there is anything between the Tx and Rx coils, as shown in Fig. 5.13.

5.5.1 Data Capture and Preprocessing

One of the most important things for a good classification is good-quality data [95]. As for the mmWave sensor, the most information rich data that can be readily obtained is the heatmap plot, as discussed in the previous section. The Azimuth-Range heatmap plot contains the reflection strength at different distances and angles. The experiment below shows how the heatmap information reflects the real-world objects within its detection range. Fig. 5.13 shows how an e-scooter looks like in a heatmap generated by the mmWave sensor and Fig. 5.14 shows the same plot with a tea can instead. It can be seen that the two objects have shown some noticeable differences in the heatmap plot, which means it could be distinguished with an appropriate classification algorithm.

To better evaluate the possibility of object classification based on mmWave radar heatmap data, six different category heatmap data were recorded:

- Background
- Scooter Only
- Human only
- Human lying down

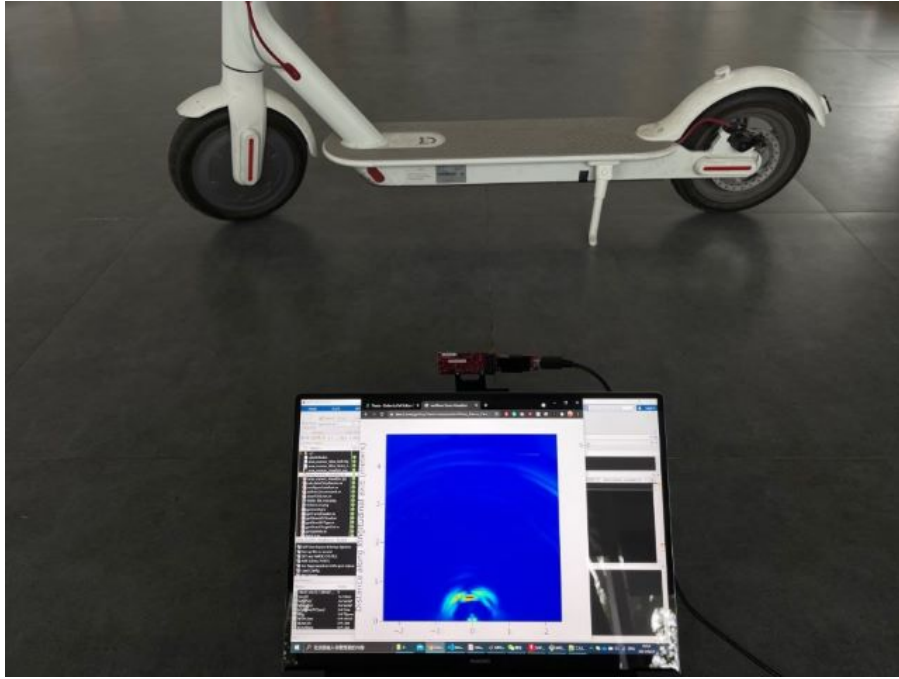


Figure 5.13: mmWave heatmap plot with an e-scooter

- Human Standing next to Scooter
- Human lying next to Scooter

The heatmap data were captured with some deliberately noise (some random movements of the scooter and human) to avoid overfitting and therefore increase the robustness of the trained model.

To simplify the training process and the trained model, the heatmap data were converted to 8-bit grey-scale PNG image format. Since the reflection strength of the original heatmap plot has a much wider dynamic range, the data were compressed to fit the 8-bit image format, which means a reduced resolution from the original data format. This leaves some room for future improvement by using a higher bit-rate format. In addition, since the detection zone of interest is limited for the target application, the heatmap plots were cropped to a smaller range of approximately 2 by 2 meters, which significantly reduces the training complexity of using the full resolution heatmap data. The final data that would be used for the classifier training are 1500 63-by-63 1D grey-scale PNG images that were labelled with six different categories accordingly. One example process of capturing and preprocessing the “human only” category

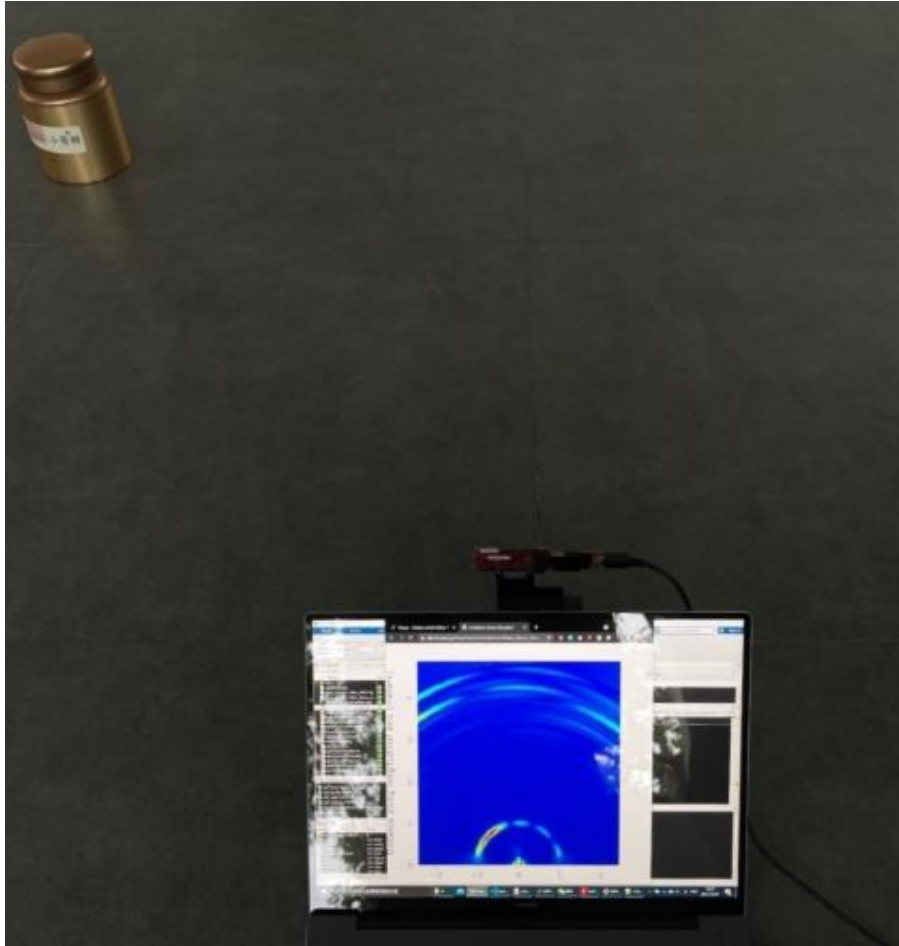


Figure 5.14: mmWave heatmap plot with a tea can

data is shown in Fig. 5.15. The same process is repeated for the other four categories.

5.5.2 Neural Network Configuration and Classifier Training

With the training data gathered, the next step is to configure an appropriate machine learning algorithm to train a classifier. Since the heatmap plot is essentially an image, this makes the problem now an image classification problem. There has been an increasing amount of research in this field in recent years, with the most commonly used neural network being the convolutional neural network (CNN) for image recognition [111].

For the initial proof-of-concept, implementing the existing CNN layer configuration would be sufficient. The network configuration (Tbl. 5.1) used in this chapter was fine-tuned based on a classic handwriting digit recognition from MATLAB [131]. Depending on the hardware used

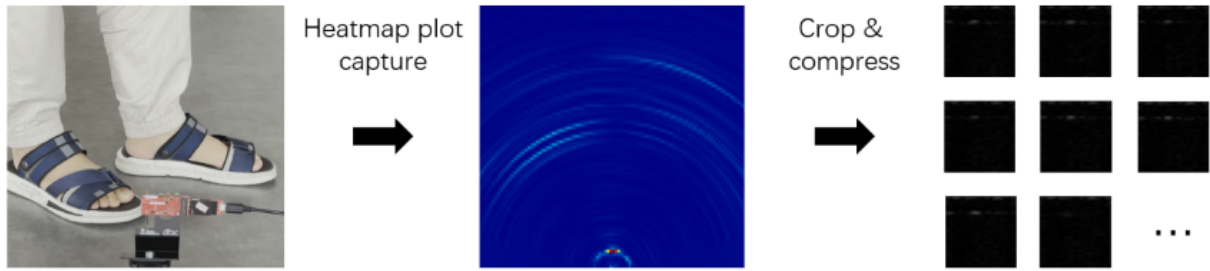


Figure 5.15: mmWave heatmap data processing

to perform the classification, the network layer can be reconfigured to lower the hardware requirement or to increase the classification accuracy.

Table 5.1: Network Layers

Layer No.	Layer Name	Details
1	Image Input	63x63x1 images with 'zerocenter'
2	Convolution	20 5x5 convolutions with stride [1 1] and padding
3	ReLU	ReLU
4	Max Pooling	2x2 max pooling with stride [2 2] and padding
5	Fully Connected	6 fully connected layer
6	Softmax	softmax
7	Classification Output	crossentropyex

With the data labeled and the network layer configured, the training process is done automatically by using MATLAB's "trainnetwork" function from Deep Learning Toolbox. For testing purposes, 5% of the data was not used for training and will be used to evaluate the performance of the trained classification model. The remaining dataset was divided into a 2:8 ratio for cross-validation. With such a relatively small dataset and a simple network layer structure, the training process finished rather rapidly by 3 minutes on a 6-core CPU. The cross-validation accuracy is approximately 96%, as shown in Fig. 5.16.

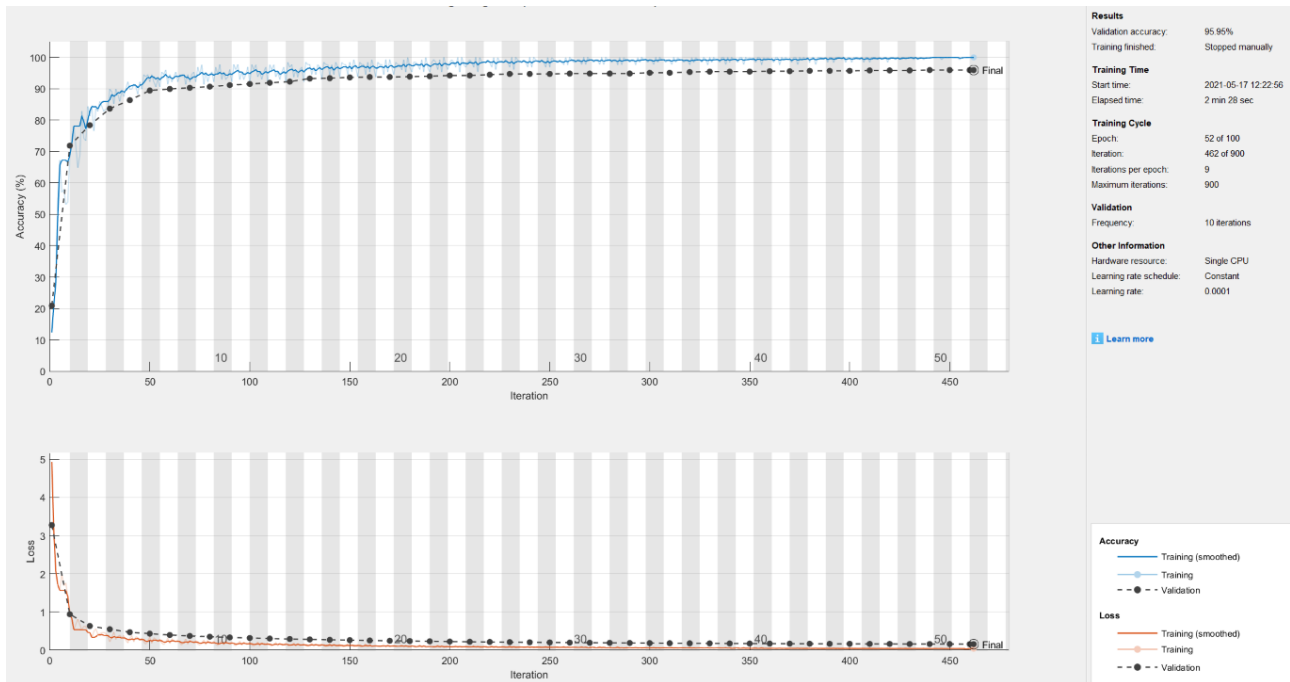


Figure 5.16: CNN training process

5.6 Performance Evaluation

The cross-validation accuracy is calculated based on the 20% training data used during the training process, therefore is not the most reliable measure of the actual performance of the model. Typically, a small set of data is reserved and not used for training, but is used to finally test the performance of the trained model. By using this set of data, the classification result is calculated as shown in Fig. 5.17. The average classification accuracy of all classes is approximately 96%. A video demonstration of this can be seen in [132].

5.7 Implementation on Low-cost Hardware

To implement this mmWave radar-based live/foreign object detection method into real-world applications, a low-cost hardware should be used instead of a full-size computer. The hardware should also have sufficient computing power to perform neural network classification. One of the most popular low-cost computer hardware is the Raspberry Pi. In this section, the MATLAB trained classification is converted into an universal format (ONNX) so that it can

True Class	huma&scooter	human	human_lying_down	nothing	scooter	scooter&human_lying
	166	1	1		9	
	1	379	16		1	
	1	3	152		9	
		1	3	435		
	31		11		305	2
						162
	huma&scooter	human	human_lying_down	nothing	scooter	scooter&human_lying
	Predicted Class					

Figure 5.17: Result confusion matrix

be implemented on other platforms, e.g., Raspberry Pi 4.

A Python script is used to communicate with the mmWave radar sensor to gather the heatmap data via a serial interface [133]. By implementing TensorFlow Lite plus ONNX extension, it is then possible to perform the same classification on a Raspberry Pi 4. The setup of the mmWave sensor is the same as before. The only difference is that instead of connecting the sensor to a computer, it is now connected to a Raspberry Pi via a USB cable. The initial result has shown similar performance to when run on a computer, which is as expected. The detection speed, however, has shown a significant drop from approximately 10 frames per second when running on a laptop to about 3 frames per second on the Raspberry Pi. Some screen shots of the testing results are showing in Fig. 5.22 and Fig. 5.23.

With the mmWave classification method being implemented on Raspberry Pi, it would be interesting to compare this FOD/LOD method compared to the ones discussed in the previous

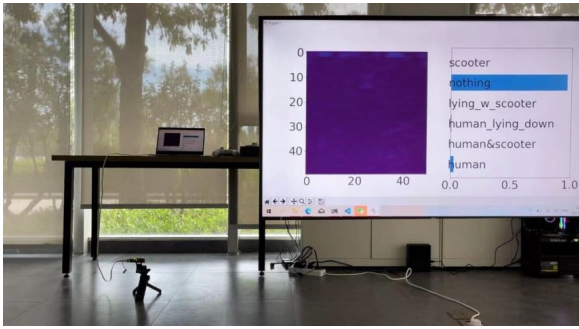


Figure 5.18: Background Only

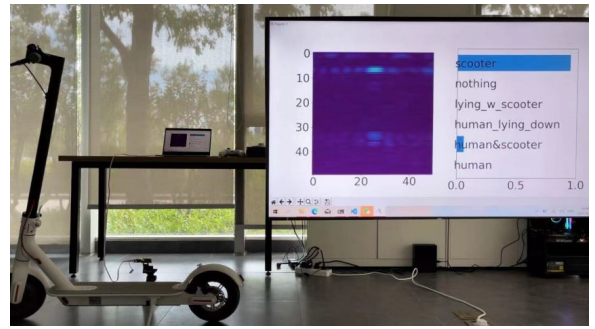


Figure 5.19: Scooter Only

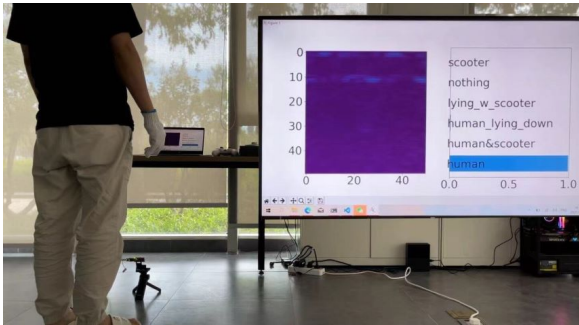


Figure 5.20: Human Only

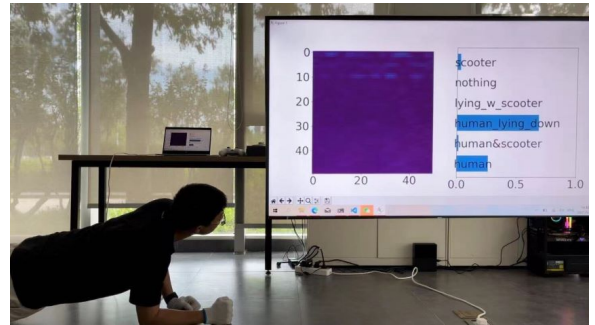


Figure 5.21: Human Lying Down

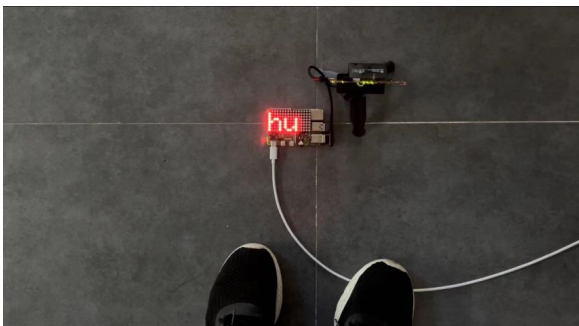


Figure 5.22: Human Only

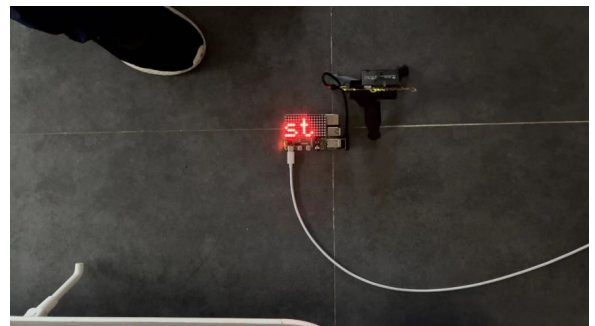


Figure 5.23: Scooter Only

chapters. As shown in Tbl. 5.2, The mmWave-based FOD/LOD method achieves the highest score except the cost section. This is primarily due to the cost of the mmWave radar sensor. Overall, the mmWave radar FOD/LOD could be suitable for applications that are less sensitive to cost, e.g., EV or e-bike wireless charger.

Table 5.2: FOD/LOD methods comparison

FOD/LOD	Accuracy	Speed	Range	Robustness	LOD	Integration	Cost
Q-factor	Low	High	Small	High	✗	Built-in	Low
Efficiency	Low	High	Small	High	✗	Partially built-in	Low
ultrasonic	Medium	High	Medium	Low	✗	External	Medium
Camera	High	High	Wide	Low	✓	External	Medium
Radar	High	High	Wide	High	✓	External	Medium
D-S voltage	High	High	Medium	High	✗	Built-in	High
mmWave	High	High	High	High	✓	External	Medium

5.8 Recommendations

This chapter has demonstrated the capabilities of the mmWave radar-based FOD/LOD systems, especially the ability for such a technique to perform object classification, which is essential to LOD. The proposed technique, however, does have its limitations, e.g., having to be externally mounted for the best results. While some FOD/LOD shown in Tbl. 5.2 could be built into an IPT system, they could not detect live objects. Although it seems like there is no FOD/LOD method that could perfectly detect both foreign and live objects while can be easy-to-integrate and low-cost, the actual applications may not need such a "perfect" detection technique. The 6.78 MHz mobile phone charger in [66], for example, does not exceed even the most stringent basic restrictions (both internal E-field and SAR), would not require a LOD system. Instead, other low-cost FOD methods could be used instead. For other applications where the safety requirement is more strict, one or more of the FOD/LOD methods in Tbl. 5.2 could be combined to achieve the best detection results.

Chapter 6

An IPT-based Localisation Technique

The previous chapters focused on safety systems that detect unintended or live objects around the IPT system. While this is important for most consumer-facing IPT applications, it may not be needed for applications that are under well-controlled environments, e.g., industrial wireless charging applications. Instead, an autonomous system that guides the to-be-charged devices to the IPT transmitter could be used as the safety system. With such a localisation system, human's involvement in the charging process can be eliminated.

In this chapter, an IPT-based localisation technique is introduced. The development of such a technique is based on the drone-related IPT applications discussed in chapter 2. The DJI Matrice 100 drone and the sensor node in chapter 2 is used as the development setup. This work was done in collaboration with the Dyson School of Design Engineering, and the Wireless Power Lab of Imperial College London. The author's contribution is primarily the IPT-related design and development, this work is also published in [134]. The complete localisation process of the drone to locate the target sensor node consists of three stages. The first stage uses GPS to guide the drone to the approximate location, then starts the second stage localisation that uses UWB ranging to further approach the target. Finally, when the IPT receive unit starts capturing the induced voltage, the last stage of localisation based on the induced voltage initiates to guide the drone to land on top of the sensor node.



Figure 6.1: UWB hardware

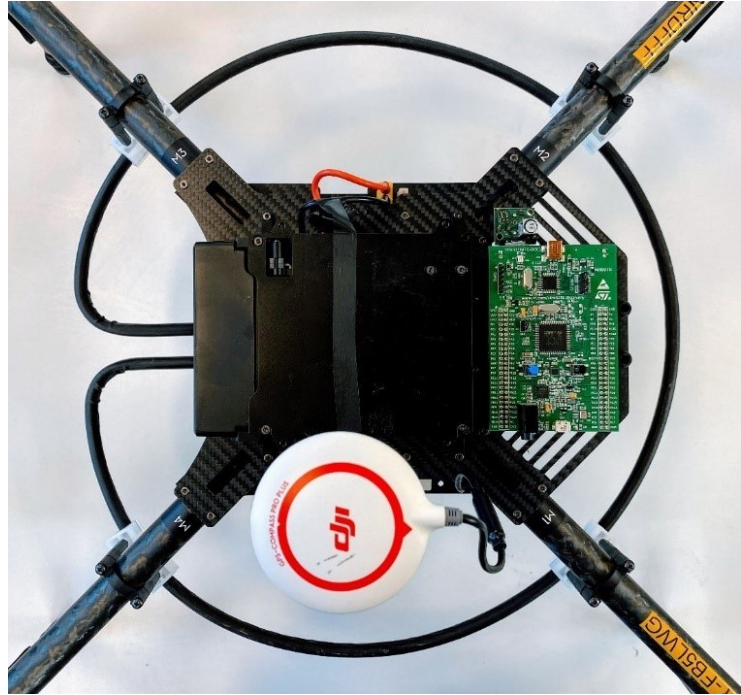


Figure 6.2: flight control hardware

6.0.1 Automated Flight Control

Before developing the localisation system, the flight control of the drone would need to be automated so that it could take the localisation data as input and to control the drone. This is achieved with additional hardware and DJI's onboard software development kit (OSDK) software [135]. The hardware chosen is the “Discovery Kit” development module (Fig. 6.2) of the STM32F4, which can be accessed in [136]. The Discovery Kit takes input from GPS, UWB, ultrasonic and remote sensor node, and process the related ranging data to generate a control command that will send to the drone's flight controller. An overview of the flight control interfaces is shown in Fig. 6.3.

GPS

GPS is used as the first stage of locating the sensor node, the accuracy of GPS would guide the drone to approximately 10 meters range of the sensor node. However, such accuracy is not enough for the drone to land within the charging range of the IPT system. Additional localisation technique is required to improve the accuracy.

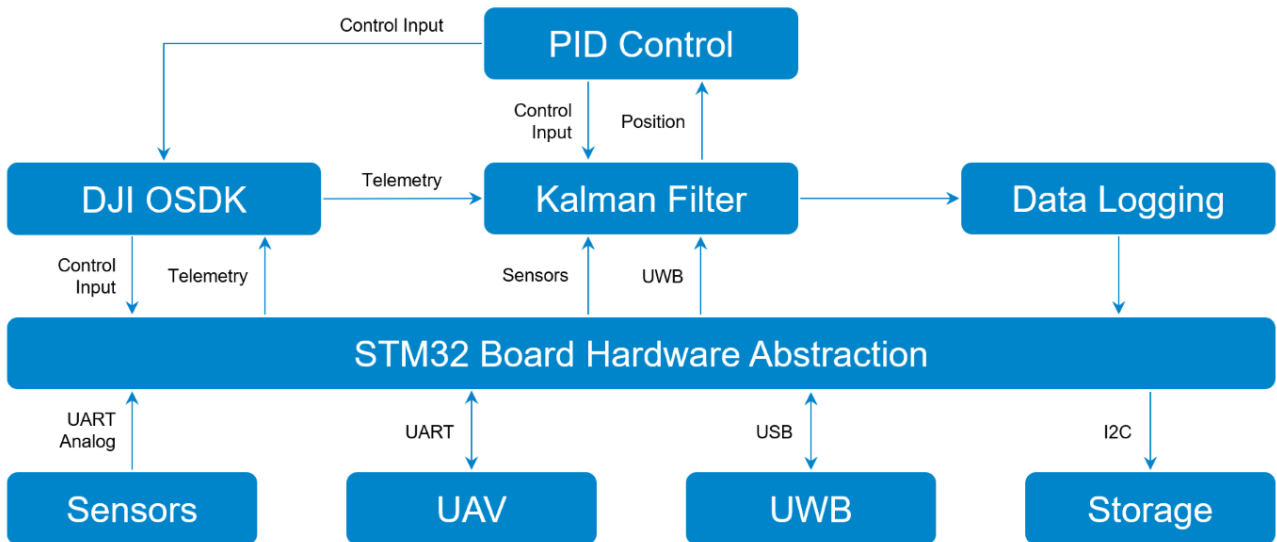


Figure 6.3: flight Control Software Implementation

UWB & Ultrasonic

Ultra-wideband (UWB) is a radio technology for ranging and communication. With proper implementation, UWB could achieve a ranging error to be below 10 cm [137]. This is significantly better than the GPS accuracy. However, the UWB range is an absolute distance between the drone and the sensor, which does not provide direction information for the drone to locate the target. Further calculations are needed. To simplify the calculation, an additional ultrasonic sensor is used to measure the height of the drone, which can be used to derive the horizontal distance between the drone and the sensor. This technique is illustrated in Fig. 6.4. With the GPS, UWB, and ultrasonic, the drone can locate the sensor more accurately. Once the drone approached in the range for IPT systems to receive the induced voltage, the IPT-based localisation stage would take over. The design of such a system is now discussed.

6.0.2 IPT-based Localisation

The proposed last stage localisation method is based on the IPT system. Such a method relies on the induced voltage at the receiver side of the IPT system to estimate the distance between the IPT transmitter and receiver. Depending on the relative position between the receiver and the transmitter, the induced voltage generally increases as the two coils approach each other.

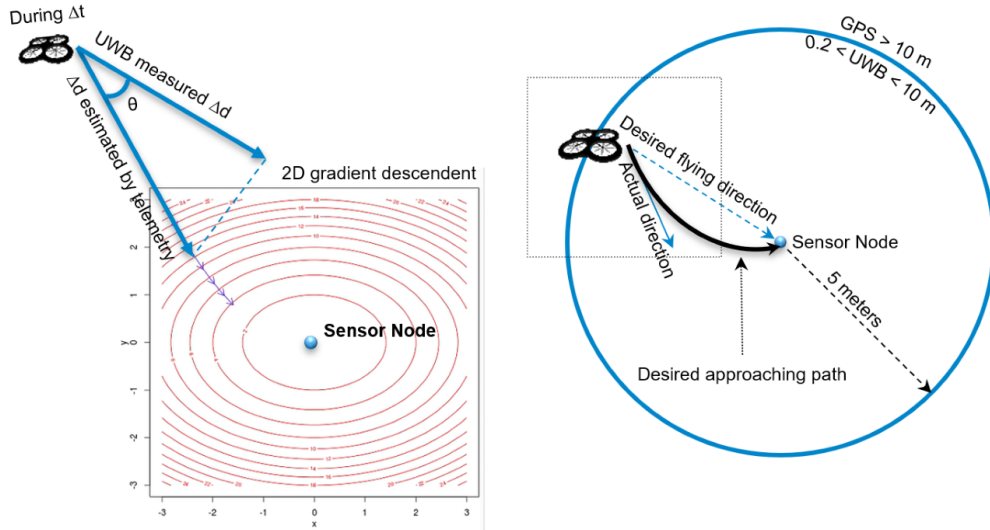


Figure 6.4: localisation using GPS, UWB & ultrasonic

One condition for such a technique to work is that the magnetic field generated from the IPT transmit coil remains constant amplitude during the localisation process. The load-independent class EF IPT design is, therefore, used for this work.

IPT System Setup

The IPT system used in this work was the same system as the 100 W IPT system for autonomous drones [38]. The Class EF inverter (Fig. 6.5) allows for load-independent tuning by selecting the components as in [79]. The solutions that are considered load-independent, achieve zero-voltage-switching (ZVS) over the entire restive load range, and in addition, when employed in an IPT system, the amplitude of the transmit coil current is load-independent.

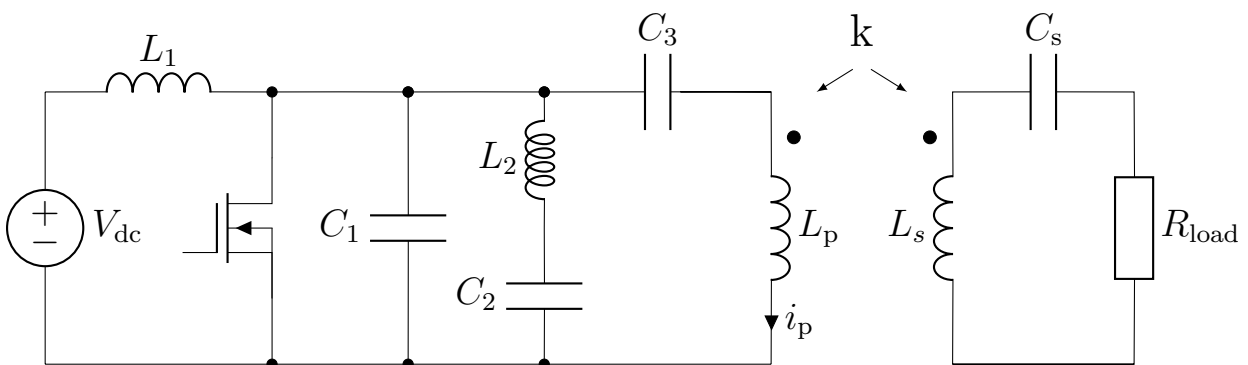


Figure 6.5: Class EF inverter circuit topology

Circuit Simulation

To prove the concept of using an IPT system for localisation, circuit simulations together with an EM simulation were conducted. A load-independent Class EF inverter was simulated inductively coupled with a full-wave rectifier at the receive side on the drone. Here, the voltage after the rectifier was measured against the coupling k between the transmit coil and the receive coil. In this case, which is aimed only for localisation, the rectifier output was set as an open circuit. The simulated circuit parameters can be found in Tbl. 6.1, and the results of the output voltage with respect to coupling can be found in Fig. 6.8. As can be seen from these results, the receiver can provide a voltage of 1 V at a coupling of $k = 0.002$, and a voltage of 20 V at a coupling of $k = 0.02$. These results are then used to roughly determine the range of coupling at which the system can practically operate. Afterwards, the EM simulations will help determine the approximate distance between the transmit and receive coils depending on their shape and size.

Table 6.1: Spice Simulation Component Values

Parameter	Value
V_{dc}	100 V
C_1	433.7 pF
C_2	400 pF
C_3	190.48 pF
L_1	80 μ H
L_2	460 nH
L_p	3.33 μ H
f	6.78 MHz

EM Simulation

With the coupling information from the circuit simulation, an EM simulation was performed using the Computer Simulation Technology (CST) to determine the approximate range for such a localisation method to operate. The simulation graphics and the shape of the coils are shown in Fig. 6.6. The rectangular coil at the bottom side represents the transmit coil and the

circular coil on top represents the receive coil. The simulation assumes the drone is hovering at a height of 50 cm over the transmit coil while the localisation method proposed can occur. Here, the only variable for the simulation is then the horizontal distance between the two coils. As shown in Fig. 6.7, at a coupling of $k = 0.002$, the horizontal displacement between the two coils is approximately 65 cm, which suggests that for an output voltage range of 1 V to 20 V, the method can operate with a total range of 1.2 meters in horizontal displacement.

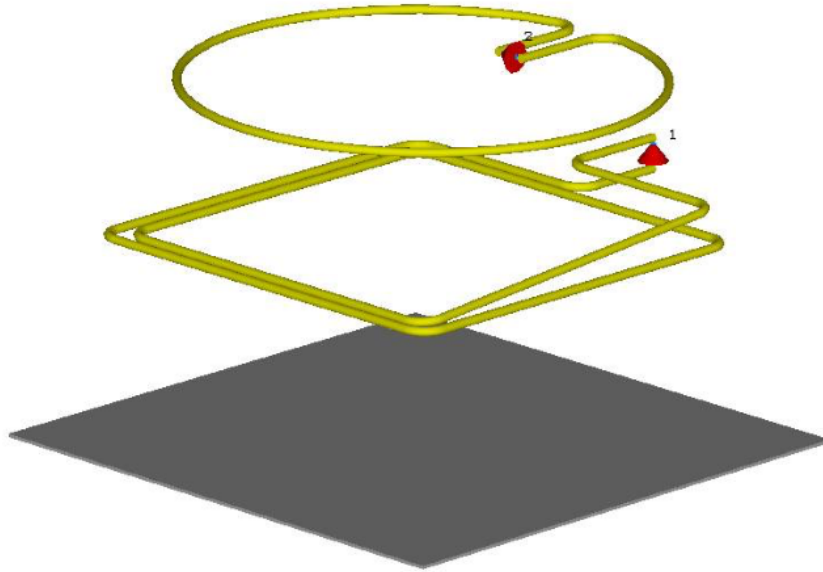


Figure 6.6: Coils shape and size using CST (Christopher Kwan)

6.0.3 Experimental Verification

The experimental setup can be seen in Fig. 6.9. Note that the IPT transmit and receive unit can be swapped if there were a communication link to transmit the induced voltage information between them. In this test, the IPT transmitter is placed under the landing pad on the lab bench. The drone is equipped with a receive coil and the rectifier, and the output voltage was measured with a multimeter (Fig. 6.9) on top of the drone. The vertical distance between the transmit coil and the receive coil varies from 50 cm to 70 cm, and the horizontal displacement ranges from 0 to 60 cm. The measured induced voltage is shown in Fig. 6.10. Note that the data was mirrored horizontally to better indicate the effective localisation range. It can be seen

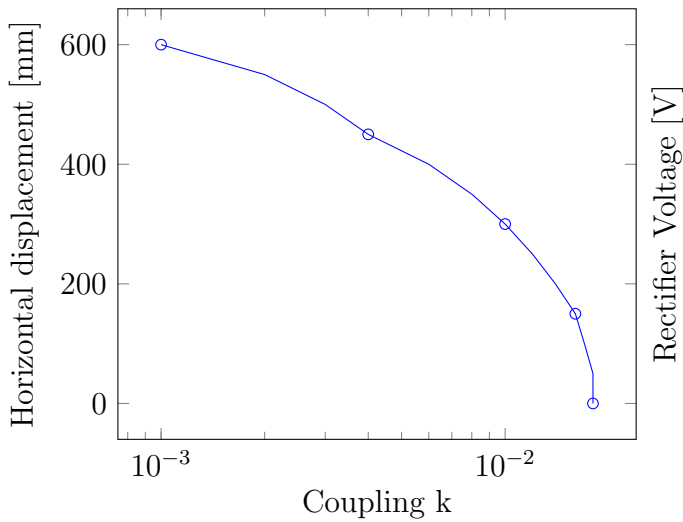


Figure 6.7: Horizontal displacement vs k

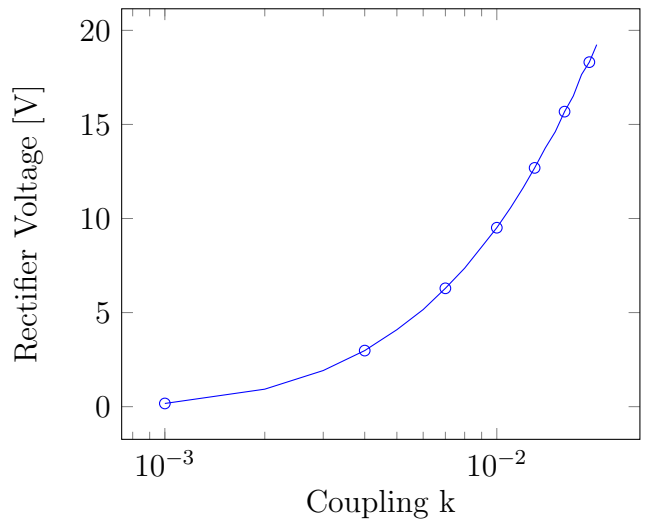


Figure 6.8: Induced Voltage vs k

that even when the drone is well outside the practical charging zone, it can still measure a small voltage at the rectifier’s output. At such distance, the effective area for the final-stage localisation is approximately 2.6 times larger than the original landing pad. The difference in the voltage between the simulation and the experiment could be caused by the modelling or instrumentation error. The output voltage of the rectifier could be further improved by using different rectifier topologies, e.g., half-wave rectifier, voltage doubler, or by increasing the current in the transmit coil.

6.0.4 Summary

Overall, this work proposed a localisation technique that uses an IPT system to assist in accurate tracking for drones to automatically land on a wireless charging pad. The technique is demonstrated experimentally using a load-independent Class EF inverter, which provides a constant magnitude magnetic flux that induces the voltage on the wireless receiver. The circuit simulation is used to determine the minimum coupling allowed for the IPT system to induce enough voltage on the receiver side for it to be practically measured, and following, an electromagnetic simulation was conducted to determine the effective range within this coupling range. Finally, a test rig was used to verify how the proposed technique could be implemented in a real case scenario.



Figure 6.9: Photograph of the experimental setup

70 cm	0.22V	0.50V	1.57V	2.92V	6.47V	8.35V	8.93V	8.35V	6.47V	2.92V	1.57V	0.50V	0.22V	70 cm
60 cm	0.83V	0.53V	0.95V	5.44V	9.41V	13.22V	14.87V	13.22V	9.41V	5.44V	0.95V	0.53V	0.83V	60 cm
50 cm	1.51V	1.84V	1.48V	4.90V	14.49V	24.46V	26.39V	24.46V	14.49V	4.90V	1.48V	1.84V	1.51V	50 cm
	-60 cm	-50 cm	-40 cm	-30 cm	-20 cm	-10 cm	0 cm	10 cm	20 cm	30 cm	40 cm	50 cm	60 cm	

Figure 6.10: IPT induced voltage vs relative position

Chapter 7

Conclusion

The focus of this PhD study is to help make wireless charging safe while trying to push the boundaries of charging speed and range. Overall, this thesis focused on the safety systems design and development for high-frequency inductive power transfer systems. This thesis started with a brief introduction to wireless power transfer and discussed about the widely used Qi standards, especially its limitations in terms of range, power, and safety. This thesis then introduced two real-world HF-IPT systems to demonstrate the capability of HF-IPT, which is the primary focus of the safety systems design and development for the FOD/LOD methods. This thesis evaluated various possible foreign or live object detection methods, and two of them were explored in further detail: the impedance reflection detection method and the mmWave radar detection method. The impedance reflection method could detect objects that closely coupled to the IPT system regardless of the existence of the IPT receiver, while the mmWave radar FOD/LOD method can be used for a wider range of detection. A classification model based on the heatmap data from the mmWave radar sensor was also developed to distinguish between different types of objects. Depending on the IPT application, one or more of the suggested FOD/LOD methods could be implemented for different safety requirements. For applications that do not involve any live or unintended objects, a localisation system could be implemented to achieve unmanned wireless charging instead. In chapter 6, a localisation method based on the IPT system was introduced to help guide a drone to a wireless charging pad. Such a system

could reduce the risk of wireless charging by eliminating human's involvement.

7.0.1 Main Research Outcomes

- A safety analysis of commercially available wireless chargers is presented in this thesis. The purpose of this analyses is to stress the safety concerns while going for higher range and power wireless charging systems. This analysis also clarifies the different types of safety considerations for wireless power transfer.
- A 100 W high-frequency IPT system was designed and developed for a commercial quad-copter drone. The developed system has achieved a tolerance of misalignment to the level that could allow autonomous drone charging to be practical. The developed system could also maintain the same charging rate as the dedicated cable charger. To the author's best knowledge, the developed system was the first to achieve such tolerance of misalignment in the drone application.
- An integrated IPT receiver that includes a receive coil, rectifier, DC-DC converter, battery management system, lithium battery cells, UWB communicate module, and additional sensors were designed and developed. This integrated receiver allows certain sensors, e.g., microphones, to operate for up to a month period, and can be recharged via an IPT transmitter equipped drone.
- Five different existing and potential FOD/LOD methods were analysed and benchmarked in this thesis. Six different metrics including accuracy, speed, range, robustness, LOD, integration, and cost were used to measure the capability of each FOD/LOD method for high-frequency IPT systems. This benchmark method is also used to evaluate the newly proposed FOD/LOD method.
- An FOD/LOD method by analysing the drain-source voltage waveform of the switching transistor was designed and developed. The proposed method could perform foreign object detection without any additional sensors except an ADC and a microprocessor.

Unlike the efficiency measurement FOD method used in the Qi-standard, the communication between IPT transmitter and receiver is not required for the drain-source voltage waveform FOD method. Along with the proposed FOD/LOD method, techniques for reducing the hardware requirement of high-speed sampling were also discussed in this thesis, including a sub-sampling technique and a way to perform near real-time tasks on a general purpose computer.

- FOD/LOD methods based on mmWave radar sensors were also designed and developed. Two different approaches of implementing the mmWave radar were discussed. The first approach is similar to most typical radar applications, and it detects objects using the reflected point cloud data, which is objects with position data. Such a method offers an easy way to implement without much postprocessing. The other approach, on the other hand, not only performs object detection, it could also be trained to recognise different types of objects to provide better accuracy. This was achieved by a combination of mmWave heatmap data and a machine learning classification model. The trained classification model could classify six different FO scenarios with an average accuracy up to 96%.
- An IPT-based localisation method is also designed for applications where human operation is not needed, for example, autonomous robots or drones. The designed system is capable of transmitting the induced voltage information from the IPT receive side to the transmit side. The voltage values can be used to estimate the distance between the IPT transmit and receive units.

7.1 Author's Contribution

This thesis showcased two real-world high-frequency IPT applications together with two foreign/live object detection methods. Some of the work reported were done in collaboration with other members of the Wireless Power Lab as well as other researchers from Imperial College London and University of Bologna. For clarity, the author's contributions are discussed below.

The first major contribution by the author is the design and development of a real-world application of the high-frequency IPT system. While there has been a considerable amount of research in high-frequency IPT, few real-world demonstrations that showcased the potential of HF-IPT were presented. The reported work in this thesis includes the design and development of an 100 W IPT system for a commercial quad-copter drone. Real-world applications face additional challenges that were not seen on a lab bench demo. The developed IPT system transmit side were designed to be able to operate in different environments to avoid detuning of the system. In addition, both the transmit side and receive side were designed to minimise the interference of the drone's own electronics and the remote control communication link. The interface between the receive side unit and the battery on the drone was also taken into account during the development. Thermal design was also carefully considered to avoid overheating during long-period operation. To the author's best knowledge, the developed system was the first to achieve the reported tolerance of misalignment.

Another contribution by the author in this thesis is the design and development of an integrated IPT receiver that includes a receive coil, rectifier, DC-DC converter, battery management system, lithium battery cells, UWB communicate module and additional sensors. One of the major challenges for remote sensor deployment is the sensor power source. While some sensors could be powered by sunlight, this is not the case for some sensors that buried underground. An integrated sensor with battery and IPT receiver could be charged by an IPT equipped drone, when the battery is depleted. The designed integrated solution not only acts as a wireless power receiver, it also manages the charging of the battery cell, as well as powering the sensors and a UWB communication link to send sensor and battery status information to the drone. The author's major contribution is on the power electronics side of this work.

The author also contributed in designing and developing a reflected impedance based FOD/LOD method. Such a method detects objects by analysing the drain-source voltage waveform of the switching transistor was designed and developed. The proposed method could perform FOD only with an ADC and a microprocessor. Unlike the efficiency measurement FOD method used in Qi-standard, the communication between IPT transmitter and receiver is not required for the drain-source voltage waveform FOD method. To author's best knowledge, the proposed FOD method was the first implementation, and the method has been filed for a patent, which is currently under review in US (US20210203192A1), CA (CA3101405A1) , WO (WO2019229217A1), CN (CN112534677A) AU (AU2019276285A1) and EP (EP3804083A1).



Figure 7.1: WPW2019

Another FOD/LOD method based on mmWave radar sensor was also designed and developed by the author. Unlike traditional radar applications, the proposed method does not rely on the point cloud data as the source to perform object detection. Instead, it uses a combination of mmWave heatmap data and machine learning techniques to train a classification model to perform LOD/LOD. Although object classification using mmWave radar is not first mentioned by the author, such technique was not reported to be used for IPT applications. The trained classification model achieved classifying six different FO scenarios with an average accuracy up

to 96%. The author also implemented the trained model on a low-cost hardware (Raspberry Pi) while maintaining the same classification accuracy.

The author also contributed organising the Wireless Power Week 2019 (WPW2019) as the local organising committee co-chair. (Fig. 7.1)

7.2 Publications

- (Patent) L. Lan, S. Aldhafer, D. C. Yates and P. D. Mitcheson, “Wireless Power Transmission System and Method”, 2019, (USPTO), Patent No.: WO2019229217A1
- L. Lan et al., “Foreign Object Detection for Wireless Power Transfer,” 2018 2nd URSI Atlantic Radio Science Meeting (AT-RASC), Meloneras, 2018, pp. 1-2. doi: 10.23919/URSI-AT-RASC.2018.8471551
- J. M. Arteaga, L. Lan, S. Aldhafer, G. Kkelis, D. C. Yates and P. D. Mitcheson, “A Multi-MHz IPT-link Developed for Load Characterisation at Highly Variable Coupling Factor,” 2018 IEEE Wireless Power Transfer Conference (WPTC), Montreal, QC, Canada, 2018, pp. 1-4. doi: 10.1109/WPT.2018.8639239
- L. Lan, J. M. Arteaga, D. C. Yates and P. D. Mitcheson, “A Reflected Impedance Estimation Technique for Inductive Power Transfer,” 2019 IEEE PELS Workshop on Emerging Technologies: Wireless Power Transfer (WoW), London, United Kingdom, 2019, pp. 45-48.
- L. Lan, C. H. Kwan, J. M. Arteaga, D. C. Yates and P. D. Mitcheson, “A 100W 6.78MHz Inductive Power Transfer System for Drones,” 2020 14th European Conference on Antennas and Propagation (EuCAP), 2020, pp. 1-4, doi: 10.23919/EuCAP48036.2020.9135731.
- J. M. Arteaga, L. Lan, C. H. Kwan, D. C. Yates and P. D. Mitcheson, “Characterisation of High Frequency Inductive Power Transfer Receivers Using Pattern Recognition on the Transmit Side Waveforms,” 2020 IEEE Applied Power Electronics Conference and Exposition (APEC), 2020, pp. 825-831, doi: 10.1109/APEC39645.2020.9124398.
- L. Lan et al., “An Induction-Based Localisation Technique for Wirelessly Charged Drones,” 2020 IEEE PELS Workshop on Emerging Technologies: Wireless Power Transfer (WoW), 2020, pp. 275-277, doi: 10.1109/WoW47795.2020.9291257.
- J. M. Arteaga, N. Pucci, L. Lan and P. D. Mitcheson, “Load Characterization in High-Frequency IPT Systems Using Class EF Switching Waveforms,” in IEEE Transactions on

Power Electronics, vol. 36, no. 10, pp. 11036-11044, Oct. 2021, doi: 10.1109/TPEL.2021.3074751.

- J. M. Arteaga et al., “Design of a One-to-Four Isolated DC-DC Converter Using a 13.56 MHz Resonant Air-Core Transformer,” 2021 IEEE Applied Power Electronics Conference and Exposition (APEC), 2021, pp. 2580-2585, doi: 10.1109/APEC42165.2021.9487409.
- J. M. Arteaga, L. Lan, N. Pucci and P. D. Mitcheson, “Design and Development of a Wireless UAV Charger for Hopping and Recharging Missions,” in 2020 16th European Conference on Antennas and Propagation (EuCAP), 2022 (submitted).

7.3 Suggestions for Future Work

Although this thesis has discussed some potential solutions to ensure the safety of wireless charging, they do have their limitations in various aspects, and a continuous effort to achieve a better safety of wireless charging is always desired. The following suggestions are made for future researchers interested in this topic.

- The impedance reflection FOD/LOD method discussed in this thesis has demonstrated some potential in becoming a standard safety system for HF-IPT applications. However, to eventually integrate this method into a product level IPT application, many other factors, e.g., cost, size, external interference, etc. need to be considered. One method of reducing the cost of ADC by using sub-sampling technique is introduced in this chapter but has not been fully integrated and tested. In addition, this impedance reflection method was tested with an AC load at the IPT Rx side, which is perfectly tuned to the operation frequency of the IPT system, so it reflects the minimum reactance to the Tx side. In reality, passive rectifiers could be used instead, which could reflect a higher reactance back to the Tx side due to the capacitance in the rectifier diodes, therefore, resulting in false-positive detection. One approach to minimise the reflected reactance from the IPT receiver is by using synchronous rectification on the IPT receive side.
- The mmWave radar-based FOD/LOD solution has also performed well in detecting live objects with an accurate object classification model. However, this technique was designed and developed without the IPT system. An integrated system should be developed to better evaluate the performance of the proposed FOD/LOD method and to see if there is any interference between the mmWave radar sensor and the IPT system. In addition, the classification model was trained as a proof of concept, with approximately 1000 training data sets. In real world applications, a higher training set size can be collected to potentially achieve better classification accuracy. In addition, the mmWave radar sensor chosen in this thesis could also be outdated as the technology advances rapidly over the recent years. More cost-effective mmWave radar sensors could be available and be implemented

for better results.

- The IPT-based localisation introduced in chapter 6 has demonstrated the possibility of estimating the distance between a pair of IPT transmit and receive coils. The actual implementation of the localisation technique based on the IPT system has not been fully tested. This is partially due to the interruptions caused by COVID-19, and partially due to the fact that the previous localisation stage that is based on the GPS and UWB has not been fully completed to guide the drone close enough to the IPT induced voltage range. Once the drone can be reliably guided into the IPT range, this localisation method can then be verified with a real-world application.

Bibliography

- [1] Matthew Schormans, Virgilio Valente, and Andreas Demosthenous. Practical inductive link design for biomedical wireless power transfer: A tutorial. *IEEE Transactions on Biomedical Circuits and Systems*, 12(5):1112–1130, 2018.
- [2] Nikola Tesla. The transmission of electrical energy without wires. *Electrical World and Engineer*, pages 21–24, 1905.
- [3] L. P. Wheeler. Ii — tesla’s contribution to high frequency. *Electrical Engineering*, 62(8):355–357, Aug 1943.
- [4] A. Kawamura, K. Ishioka, and J. Hirai. Wireless transmission of power and information through one high frequency resonant ac link inverter for robot manipulator applications. In *IAS ’95. Conference Record of the 1995 IEEE Industry Applications Conference Thirtieth IAS Annual Meeting*, volume 3, pages 2367–2372 vol.3, 1995.
- [5] W. C. Brown. Free-space transmission. *IEEE Spectrum*, 1(10):86–91, 1964.
- [6] Guoxing Wang, Wentai Liu, R. Bashirullah, M. Sivaprakasam, G.A. Kendir, Ying Ji, M.S. Humayun, and J.D. Weiland. A closed loop transcutaneous power transfer system for implantable devices with enhanced stability. In *2004 IEEE International Symposium on Circuits and Systems (IEEE Cat. No.04CH37512)*, volume 4, pages IV–17, 2004.
- [7] K. van Schuylenbergh and R. Puers. *Inductive Powering: Basic Theory and Application to Biomedical Systems*. Analog Circuits and Signal Processing. Springer Netherlands, 2009.

- [8] Paul D. Mitcheson, Eric M. Yeatman, G. Kondala Rao, Andrew S. Holmes, and Tim C. Green. Energy harvesting from human and machine motion for wireless electronic devices. *Proceedings of the IEEE*, 96(9):1457–1486, 2008.
- [9] Christopher R. Valenta and Gregory D. Durgin. Harvesting wireless power: Survey of energy-harvester conversion efficiency in far-field, wireless power transfer systems. *IEEE Microwave Magazine*, 15(4):108–120, 2014.
- [10] Pavan S. Yedavalli, Taneli Riihonen, Xiaodong Wang, and Jan M. Rabaey. Far-field rf wireless power transfer with blind adaptive beamforming for internet of things devices. *IEEE Access*, 5:1743–1752, 2017.
- [11] Kaibin Huang and Erik Larsson. Simultaneous information and power transfer for broadband wireless systems. *IEEE Transactions on Signal Processing*, 61(23):5972–5986, 2013.
- [12] Hubregt J. Visser, Adrianus C. F. Reniers, and Jeroen A. C. Theeuwes. Ambient rf energy scavenging: Gsm and wlan power density measurements. In *2008 38th European Microwave Conference*, pages 721–724, 2008.
- [13] Weiyang Zhou and Ke Jin. Optimal photovoltaic array configuration under gaussian laser beam condition for wireless power transmission. *IEEE Transactions on Power Electronics*, 32(5):3662–3672, 2017.
- [14] Kate J Duncan. Laser based power transmission: Component selection and laser hazard analysis. In *2016 IEEE PELS Workshop on Emerging Technologies: Wireless Power Transfer (WoW)*, pages 100–103, 2016.
- [15] Naoki Shinohara. History of research and development of beam wireless power transfer. In *2018 IEEE Wireless Power Transfer Conference (WPTC)*, pages 1–4, 2018.
- [16] Jaime Garnica, Raul A. Chinga, and Jenshan Lin. Wireless power transmission: From far field to near field. *Proceedings of the IEEE*, 101(6):1321–1331, 2013.

- [17] Alanson P. Sample, David T. Meyer, and Joshua R. Smith. Analysis, experimental results, and range adaptation of magnetically coupled resonators for wireless power transfer. *IEEE Transactions on Industrial Electronics*, 58(2):544–554, 2011.
- [18] Grant A. Covic and John T. Boys. Inductive power transfer. *Proceedings of the IEEE*, 101(6):1276–1289, 2013.
- [19] Siqi Li and Chunting Chris Mi. Wireless power transfer for electric vehicle applications. *IEEE Journal of Emerging and Selected Topics in Power Electronics*, 3(1):4–17, 2015.
- [20] Mitchell Kline, Igor Izyumin, Bernhard Boser, and Seth Sanders. Capacitive power transfer for contactless charging. In *2011 Twenty-Sixth Annual IEEE Applied Power Electronics Conference and Exposition (APEC)*, pages 1398–1404, 2011.
- [21] Jiejian Dai and Daniel C. Ludois. A survey of wireless power transfer and a critical comparison of inductive and capacitive coupling for small gap applications. *IEEE Transactions on Power Electronics*, 30(11):6017–6029, 2015.
- [22] A. Kumar, S. Pervaiz, Chieh-Kai Chang, S. Korhummel, Z. Popovic, and K. K. Afridi. Investigation of power transfer density enhancement in large air-gap capacitive wireless power transfer systems. In *2015 IEEE Wireless Power Transfer Conference (WPTC)*, pages 1–4, 2015.
- [23] V. F. Tseng, S. S. Bedair, and N. Lazarus. Acoustic wireless power transfer with receiver array for enhanced performance. In *2017 IEEE Wireless Power Transfer Conference (WPTC)*, pages 1–4, 2017.
- [24] Angad S. Rekhi, Butrus T. Khuri-Yakub, and Amin Arbabian. Wireless power transfer to millimeter-sized nodes using airborne ultrasound. *IEEE Transactions on Ultrasonics, Ferroelectrics, and Frequency Control*, 64(10):1526–1541, 2017.
- [25] D. van Wageningen and T. Staring. The qi wireless power standard. In *Proceedings of 14th International Power Electronics and Motion Control Conference EPE-PEMC 2010*, pages S15–25–S15–32, 2010.

- [26] Sungryul Huh, Bumjin Park, Dongwook Kim, Jongwook Kim, Jaehyoung Park, Haerim Kim, Yujun Shin, and Seungyoung Ahn. Optimal transmitter selection method for maximum power efficiency for wireless power transfer system using multi-transmitter. In *2020 IEEE Wireless Power Transfer Conference (WPTC)*, pages 296–299, 2020.
- [27] Yuan Cao and Jaber A. Abu Qahouq. Analysis and evaluation of input power splitting method between multiple transmitters for maximum wireless power transfer. In *2018 IEEE Applied Power Electronics Conference and Exposition (APEC)*, pages 959–962, 2018.
- [28] Prasad Jayathurathnage and Fu Liu. Optimal excitation of multi-transmitter wireless power transfer system without receiver sensors. In *2019 IEEE PELS Workshop on Emerging Technologies: Wireless Power Transfer (WoW)*, pages 25–28, 2019.
- [29] Prasad Jayathurathnage, D. M. Vilathgamuwa, Shaun D. Gregory, John F. Fraser, and Ngoc Tham Tran. Effects of adjacent transmitter current for multi-transmitter wireless power transfer. In *2017 IEEE Southern Power Electronics Conference (SPEC)*, pages 1–4, 2017.
- [30] Apple reveals more technical details about airpower in a european patent filing. <https://tinyurl.com/5fdm3uju>. Accessed: 2021-08-27.
- [31] Apple cancels airpower wireless charger. <https://tinyurl.com/2uvx984s>. Accessed: 2021-08-27.
- [32] J. Glenn Künzler. What really happened to apple’s airpower? <https://tinyurl.com/nd2juh5>. Accessed: 2021-08-27.
- [33] Airpower and xiaomi tracking wireless charger teardown. <https://www.bilibili.com/video/BV1Hv411i7LV?zw>. Accessed: 2021-08-27.
- [34] Yuan-Hua Zhang, Yi-Cheng Lin, Sheng-Xiu Lin, Wei-Zhe Gao, Liang-Bi Chen, Wan-Jung Chang, Wei-Wen Hu, and Chao-Tang Yu. An implementation of an automatic adjustment power transfer position wireless battery charging system for mobile devices. In *2017 IEEE 6th Global Conference on Consumer Electronics (GCCE)*, pages 1–2, 2017.

- [35] Samer Aldhafer, Paul D. Mitcheson, Juan M. Arteaga, George Kkelis, and David C. Yates. Light-weight wireless power transfer for mid-air charging of drones. In *2017 11th European Conference on Antennas and Propagation (EUCAP)*, pages 336–340, 2017.
- [36] How wireless power charging could recharge a flying drone. <https://www.bbc.com/news/av/technology-37821459>. Accessed: 2021-08-27.
- [37] C. H. Kwan, J. M. Arteaga, D. C. Yates, and P. D. Mitcheson. Design and construction of a 100 w wireless charger for an e-scooter at 6.78 mhz. In *2019 IEEE PELS Workshop on Emerging Technologies: Wireless Power Transfer (WoW)*, pages 186–190, 2019.
- [38] L. Lan, C. Kwan, J. M. Arteaga, D. C. Yates, and P. D. Mitcheson. A 100 w 6.78 mhz inductive power transfer system for drones. In *2020 EUCAP*, page Accepted, 2019.
- [39] Wireless power transfer & charging standards - airfuel alliance, 2020. <https://airfuel.org/>. Accessed: 31 Oct 2021.
- [40] International Commission on Non-Ionizing Radiation Protection and others. Guidelines for limiting exposure to time-varying guidelines for limiting exposure to time-varying electric, magnetic and electromagnetic fields. *Health Physics*, 74:494–522, 1998.
- [41] C. H. Kwan, D. C. Yates, and P. D. Mitcheson. Design objectives and power limitations of human implantable wireless power transfer systems. In *2016 IEEE Wireless Power Transfer Conference (WPTC)*, pages 1–4, May 2016.
- [42] C. H. Kwan, D. C. Yates, and P. D. Mitcheson. Design objectives and power limitations of human implantable wireless power transfer systems. In *2016 IEEE Wireless Power Transfer Conference (WPTC)*, pages 1–4, May 2016.
- [43] A. Christ, M. G. Douglas, J. M. Roman, E. B. Cooper, A. P. Sample, B. H. Waters, J. R. Smith, and N. Kuster. Evaluation of wireless resonant power transfer systems with human electromagnetic exposure limits. *IEEE Trans. Electromagn. Compat.*, 55(2):265–274, April 2013.

- [44] Design of wireless power transfer systems in the presence of living objects. Christopher H. Kwan, Imperial College London. [PhD thesis].
- [45] H.A. Wheeler. Formulas for the skin effect. *Proceedings of the IRE*, 30(9):412–424, 1942.
- [46] I.D. Vagner, B.I. Lembrikov, and P.R. Wyder. *Electrodynamics of Magnetoactive Media*. Springer Series in Solid-State Sciences. Springer Berlin Heidelberg, 2003.
- [47] Mn-zn ferrite material characteristics. https://product.tdk.com/en/system/files?file=dam/doc/product/ferrite/ferrite/ferrite-core/catalog/ferrite_mn-zn_material_characteristics_en.pdf. [online] Accessed: 8 Feb 2022.
- [48] James Lawson, David C. Yates, and Paul D. Mitcheson. High Q coil measurement for inductive power transfer. *IEEE Transactions on Microwave Theory and Techniques*, 67(5):1962–1973, 2019.
- [49] S. Aldhafer, D. C. Yates, and P. D. Mitcheson. Design and development of a class ef_2 inverter and rectifier for multimegahertz wireless power transfer systems. *IEEE Transactions on Power Electronics*, 31(12):8138–8150, Dec 2016.
- [50] K. Peng and E. Santi. Class e resonant inverter optimized design for high frequency (mhz) operation using egeant hemts. In *2015 IEEE Applied Power Electronics Conference and Exposition (APEC)*, pages 2469–2473, March 2015.
- [51] J. M. Arteaga, G. Kkelis, S. Aldhafer, D. C. Yates, and P. D. Mitcheson. Probability-based optimisation for a multi-MHz IPT system with variable coupling. In *IEEE PELS Workshop on Emerging Technologies: Wireless Power (WoW)*, pages 1–5, June 2018.
- [52] S. Aldhafer, D. C. Yates, and P. D. Mitcheson. Design and development of a class ef_2 inverter and rectifier for multimegahertz wireless power transfer systems. *IEEE Transactions on Power Electronics*, 31(12):8138–8150, Dec 2016.

- [53] D. M. Divan and G. Skibinski. Zero-switching-loss inverters for high-power applications. *IEEE Transactions on Industry Applications*, 25(4):634–643, 1989.
- [54] Samer Aldhafer, Paul D. Mitcheson, and D. C. Yates. Load-independent Class EF inverters for inductive wireless power transfer. In *IEEE Wireless Power Transfer Conf. (WPTC)*, pages 1–4, May 2016.
- [55] Breaking speed limits with gan power ics. <https://navitassemi.com/breaking-speed-limits-with-gan-power-ics/>. Accessed: 31 Oct 2021.
- [56] The tesla model 3 is driving the chip industry’s transition into the post-silicon age. <https://www.teslarati.com/tesla-model-3-sic-chip-revolution/>. Accessed: 31 Oct 2021.
- [57] J. M. Arteaga, L. Lan, S. Aldhafer, G. Kkelis, D. C. Yates, and P. D. Mitcheson. A multi-mhz ipt-link developed for load characterisation at highly variable coupling factor. In *2018 IEEE Wireless Power Transfer Conference (WPTC)*, pages 1–4, 2018.
- [58] Design of high frequency inductive power transfer systems for integration into applications. Juan M. Arteaga, Imperial College London. [PhD thesis].
- [59] M.K. Kazimierczuk and J. Jozwik. Class-e zero-voltage-switching and zero-current-switching rectifiers. *IEEE Transactions on Circuits and Systems*, 37(3):436–444, 1990.
- [60] George Kkelis, David C. Yates, and Paul D. Mitcheson. Class-e half-wave zero dv/dt rectifiers for inductive power transfer. *IEEE Transactions on Power Electronics*, 32(11):8322–8337, 2017.
- [61] How many people are affected by electrocution? <https://www.electrocuted.com/safety/statistics/>. Accessed: 31 Oct 2021.
- [62] Wikipedia: Radiation. <https://en.wikipedia.org/wiki/Radiation>. Accessed: 2021-09-01.
- [63] Radiation: Electromagnetic fields. <https://www.who.int/news-room/q-a-detail/radiation-electromagnetic-fields>. Accessed: 2021-08-31.

- [64] International Commission on Non-Ionizing Radiation Protection and others. Guidelines for limiting exposure to time-varying electric and magnetic fields (1 Hz to 100 kHz). *Health physics*, 99(6):818–836, 2010.
- [65] ICNIRP. Guide-lines for limiting exposure to time-varying electric magnetic and electromagnetic fields (up to 300 ghz). In *Health Physics*, volume 74, pages 494–522, 2016.
- [66] Highly resonant wireless power transfer: Safe, efficient, and over distance. <http://large.stanford.edu/courses/2016/ph240/surakitbovorn1/docs/kesler.pdf>. [online] Accessed: 31 Oct 2021.
- [67] S. Aldhafer, Paul D. Mitcheson, J. M. Arteaga, G. Kkelis, and D. C. Yates. Light-weight wireless power transfer for mid-air charging of drones. In *11th European Conf. on Antennas and Propagation (EUCAP)*, pages 1–5, March 2017.
- [68] Jane Horrell. Testing the waters: a new challenge for the wireless power lab drone.: Imperial news: Imperial college london, Jun 2019.
- [69] A. Raciti, S. A. Rizzo, and G. Susinni. Drone charging stations over the buildings based on a wireless power transfer system. In *Industrial and Commercial Power Systems Technical Conference (I CPS)*, pages 1–6, May 2018.
- [70] Milan Erdelj, Enrico Natalizio, Kaushik R. Chowdhury, and Ian F. Akyildiz. Help from the sky: Leveraging uavs for disaster management. *IEEE Pervasive Computing*, 16(1):24–32, 2017.
- [71] Mars 2. <https://nssdc.gsfc.nasa.gov/nmc/spacecraft/display.action?id=1971-045A>. Accessed: 1st Oct 2021.
- [72] China’s mars rover zhurong completes primary mission, gets life extension. <https://www.space.com/china-zhurong-mars-rover-extended-mission>. Accessed: 1st Oct 2021.
- [73] Mars 2020 mission overview. <https://mars.nasa.gov/mars2020/mission/overview/>. Accessed: 1st Oct 2021.

- [74] Nasa's ingenuity mars helicopter recharges its batteries in flight. <https://www.nasa.gov/feature/jpl/nasas-ingenuity-mars-helicopter-recharges-its-batteries-in-flight>. Accessed: 1st Oct 2021.
- [75] C. H. Choi, H. J. Jang, S. G. Lim, H. C. Lim, S. H. Cho, and I. Gaponov. Automatic wireless drone charging station creating essential environment for continuous drone operation. In *2016 International Conference on Control, Automation and Information Sciences (ICCAIS)*, pages 132–136, Oct 2016.
- [76] Shu Yuen Ron Hui, Wenxing Zhong, and Chi Kwan Lee. A critical review of recent progress in mid-range wireless power transfer. *IEEE Trans. on Power Electron.*, 29(9):4500–4511, Sept 2014.
- [77] M. Pinuela, D. C. Yates, S. Lucyszyn, and P. D. Mitcheson. Maximizing DC-to-load efficiency for inductive power transfer. *IEEE Trans. Power Electron.*, 28(5):2437–2447, May 2013.
- [78] J. M. Arteaga, S. Aldhafer, G. Kkelis, C. Kwan, D. C. Yates, and P. D. Mitcheson. Dynamic capabilities of multi-MHz inductive power transfer systems demonstrated with batteryless drones. *IEEE Trans. on Power Electron.*, 34(6):5093–5104, June 2019.
- [79] S. Aldhafer, D. C. Yates, and P. D. Mitcheson. Load-independent class E/EF inverters and rectifiers for MHz-switching applications. *IEEE Trans. on Power Electron.*, pages 1–1, 2018.
- [80] J. M. Arteaga, S. Aldhafer, G. Kkelis, D. C. Yates, and P. D. Mitcheson. Multi-MHz IPT systems for variable coupling. *IEEE Trans. Power Electron.*, 33(9):7744–7758, Sept 2018.
- [81] Patrick C. K. Luk and Samer Aldhafer. Analysis and design of a class d rectifier for a class e driven wireless power transfer system. In *2014 IEEE Energy Conversion Congress and Exposition (ECCE)*, pages 851–857, 2014.

- [82] Analog ltc3895. <https://www.analog.com/media/en/technical-documentation/data-sheets/3895fa.pdf>. [datasheet] Accessed: 31 Oct 2021.
- [83] Thales drone. <https://www.youtube.com/watch?v=erzGmX2SZ2Y>. Accessed: 31 Oct 2021.
- [84] Wolfspeed c3d04060e. <https://assets.wolfspeed.com/uploads/2020/12/C3D04060E.pdf>. [datasheet] Accessed: 31 Oct 2021.
- [85] Ti bq25895. <https://www.ti.com/product/BQ25895>. [datasheet] Accessed: 31 Oct 2021.
- [86] Panasonic ncr18650b. <https://www.battery.com.sg/our-products/2520-panasonic-ncr18650b-18650-37v-rechargeable-li-ion-battery.html>. [datasheet] Accessed: 31 Oct 2021.
- [87] Methods for foreign object detection in inductive wireless charging. <https://www.wirelesspowerconsortium.com/data/downloadables/1/9/0/9/wpc1704-vladimir-muratov-methods-for-foreign-object-detection.pdf>. Accessed: 2021-09-07.
- [88] Ying Sun, Guo Wei, Kejun Qian, Peng He, Chunbo Zhu, and Kai Song. A foreign object detection method based on variation of quality factor of detection coil at multi-frequency. In *2021 IEEE 12th Energy Conversion Congress Exposition - Asia (ECCE-Asia)*, pages 1578–1582, 2021.
- [89] V Muratov. Robust foreign objects detection, 2019.
- [90] Jia Tang Xiue Gao. Human bioelectrical impedance measuring method based on principle of multi-frequency and multi-segment. *2011 International Conference on Advances in Engineering*, 24:459–463, 2011.
- [91] M. D. Fariñas, T. E. Gómez Álvarez-Arenas, E. Cuevas Aguado, and M. García Merino. Non-contact ultrasonic inspection of cfrp prepregs for aeronautical applications during

- lay-up fabrication. In *2013 IEEE International Ultrasonics Symposium (IUS)*, pages 1590–1593, 2013.
- [92] F. Guarato, V. Laudan, and J. F. C. Windmill. Ultrasonic sonar system for target localization with one emitter and four receivers: Ultrasonic 3d localization. In *2017 IEEE SENSORS*, pages 1–3, 2017.
- [93] D. Bank and T. Kampke. High-resolution ultrasonic environment imaging. *IEEE Transactions on Robotics*, 23(2):370–381, 2007.
- [94] Ultrasonic sensing basics. <https://www.ti.com/lit/an/slaa907c/slaa907c.pdf>. Accessed: 2021-09-10.
- [95] Yaser S. Abu-Mostafa, Malik Magdon-Ismail, and Hsuan-Tien Lin. *Learning From Data*. AMLBook, 2012.
- [96] Jia Deng, Wei Dong, Richard Socher, Li-Jia Li, Kai Li, and Li Fei-Fei. Imagenet: A large-scale hierarchical image database. In *2009 IEEE Conference on Computer Vision and Pattern Recognition*, pages 248–255, 2009.
- [97] Kaiming He, Xiangyu Zhang, Shaoqing Ren, and Jian Sun. Deep residual learning for image recognition. In *2016 IEEE Conference on Computer Vision and Pattern Recognition (CVPR)*, pages 770–778, 2016.
- [98] D. Gerónimo, J. Serrat, A. M. López, and R. Baldrich. Traffic sign recognition for computer vision project-based learning. *IEEE Transactions on Education*, 56(3):364–371, 2013.
- [99] J. Canny. A computational approach to edge detection. *IEEE Transactions on Pattern Analysis and Machine Intelligence*, PAMI-8(6):679–698, 1986.
- [100] Yolor. <https://viso.ai/deep-learning/yolor/>. Accessed: 2021-09-28.
- [101] S. Paisitkriangkrai, C. Shen, and A. v. d. Hengel. Pedestrian detection with spatially pooled features and structured ensemble learning. *IEEE Transactions on Pattern Analysis and Machine Intelligence*, 38(6):1243–1257, 2016.

- [102] W. Menzel and A. Moebius. Antenna concepts for millimeter-wave automotive radar sensors. *Proceedings of the IEEE*, 100(7):2372–2379, 2012.
- [103] C. Lovescu and S. Rao. The fundamentals of millimeter wave sensors. In *Texas Instruments*, 2017.
- [104] Manfred Constapel, Marco Cimdins, and Horst Hellbrück. A practical toolbox for getting started with mmwave fmcw radar sensors. In *Proceedings of the 4th KuVS/GI Expert Talk on Localization*, 2019.
- [105] A. Nguyen. mmwave radar sensors: Object versus range. In *Texas Instruments*, 2018.
- [106] J. H. Wehling. Multifunction millimeter-wave systems for armored vehicle application. *IEEE Transactions on Microwave Theory and Techniques*, 53(3):1021–1025, 2005.
- [107] R. J. Evans, P. M. Farrell, G. Felic, H. T. Duong, H. V. Le, J. Li, M. Li, W. Moran, and E. Skafidas. Consumer radar: Opportunities and challenges. In *2014 11th European Radar Conference*, pages 5–8, 2014.
- [108] V. Jain, F. Tzeng, L. Zhou, and P. Heydari. A single-chip dual-band 22–29-ghz/77–81-ghz bicmos transceiver for automotive radars. *IEEE Journal of Solid-State Circuits*, 44(12):3469–3485, 2009.
- [109] L. Lan, J. M. Arteaga, D. C. Yates, and P. D. Mitcheson. A reflected impedance estimation technique for inductive power transfer. In *2019 IEEE PELS Workshop on Emerging Technologies: Wireless Power Transfer (WoW)*, pages 45–48, 2019.
- [110] Vladimir N. Vapnik. *The Nature of Statistical Learning Theory*. Springer-Verlag, Berlin, Heidelberg, 1995.
- [111] Kunihiro Fukushima. Neocognitron: A self-organizing neural network model for a mechanism of pattern recognition unaffected by shift in position. *Biological Cybernetics*, 36(4):193–202, Apr 1980.

- [112] Nunzio Pucci, Juan M. Arteaga, Christopher H. Kwan, David C. Yates, and Paul D. Mitcheson. Induced voltage estimation from class ef switching harmonics in hf-ipt systems. *IEEE Transactions on Power Electronics*, 37(4):4903–4916, 2022.
- [113] D. Graupe, R. W. Liu, and G. S. Moschytz. Applications of neural networks to medical signal processing. In *Proceedings of the 27th IEEE Conference on Decision and Control*, pages 343–347 vol.1, Dec 1988.
- [114] S. Lawrence, C. L. Giles, Ah Chung Tsoi, and A. D. Back. Face recognition: a convolutional neural-network approach. *IEEE Transactions on Neural Networks*, 8(1):98–113, Jan 1997.
- [115] The mnist database. <http://yann.lecun.com/exdb/mnist/>. [online] Accessed: 11 Feb 2022.
- [116] Y. Lecun, L. Bottou, Y. Bengio, and P. Haffner. Gradient-based learning applied to document recognition. *Proceedings of the IEEE*, 86(11):2278–2324, 1998.
- [117] J. M. Arteaga, L. Lan, S. Aldhaher, G. Kkelis, D. C. Yates, and P. D. Mitcheson. A multi-MHz IPT-link developed for load characterisation at highly variable coupling factor. In *IEEE Wireless Power Transfer Conf. (WPTC)*, pages 1–4, June 2018.
- [118] Moshe Mishali and Yonina C. Eldar. From theory to practice: Sub-nyquist sampling of sparse wideband analog signals. *IEEE Journal of Selected Topics in Signal Processing*, 4(2):375–391, 2010.
- [119] Ad9226. <https://www.analog.com/media/en/technical-documentation/data-sheets/AD9226.pdf>. Accessed: 2021-10-11.
- [120] Raspberry pi as an oscilloscope @ 10 msps. <https://digibird1.wordpress.com/raspberry-pi-as-an-oscilloscope-10-msps/>. Accessed: 2021-10-11.
- [121] Adc12010. <https://www.ti.com/product/ADC12010>. Accessed: 31 Oct 2021.
- [122] Thermal testing raspberry pi 4. <https://www.raspberrypi.com/news/thermal-testing-raspberry-pi-4/>. Accessed: 31 Oct 2021.

- [123] Jyoti Bhatia, Aveen Dayal, Ajit Jha, Santosh K. Vishvakarma, J Soumya, M. B. Srinivas, Phaneendra K. Yalavarthy, Abhinav Kumar, V. Lalitha, Sagar Koorapati, and Linga Reddy Cenkeramaddi. Object classification technique for mmwave fmcw radars using range-fft features. In *2021 International Conference on COMmunication Systems NETworkS (COMSNETS)*, pages 111–115, 2021.
- [124] Zihao Zhao, Yuying Song, Fucheng Cui, Jiang Zhu, Chunyi Song, Zhiwei Xu, and Kai Ding. Point cloud features-based kernel svm for human-vehicle classification in millimeter wave radar. *IEEE Access*, 8:26012–26021, 2020.
- [125] Texas Instruments. *IWR6843AOP Single-Chip 60- to 64-GHz mmWave Sensor Antennas-On-Package (AOP)*, 4 2021.
- [126] Iwr6843aopevm. <https://www.ti.com/tool/IWR6843AOPEVM>. Accessed: 2021-09-28.
- [127] Ti mmwave demo visualiser. https://dev.ti.com/gallery/view/mmwave/mmWave_Demo_Visualizer/ver/3.5.0/. Accessed: 2021-09-28.
- [128] Christopher H. Kwan, Juan M. Arteaga, Nunzio Pucci, David C. Yates, and Paul D. Mitcheson. A 110w e-scooter wireless charger operating at 6.78mhz with ferrite shielding. In *2021 IEEE PELS Workshop on Emerging Technologies: Wireless Power Transfer (WoW)*, pages 1–4, 2021.
- [129] mmwave demo - alec. https://youtu.be/wdaEZ9J4P_8. Accessed: 2021-10-11.
- [130] Shizhe Zang, Ming Ding, David Smith, Paul Tyler, Thierry Rakotoarivelo, and Mohamed Ali Kaafar. The impact of adverse weather conditions on autonomous vehicles: How rain, snow, fog, and hail affect the performance of a self-driving car. *IEEE Vehicular Technology Magazine*, 14(2):103–111, 2019.
- [131] Create simple deep learning network for classification. <https://www.mathworks.com/help/deeplearning/ug/create-simple-deep-learning-network-for-classification.html>. Accessed: 2021-09-28.

- [132] mmwave object detector demo - 17th may. https://www.youtube.com/watch?v=FTX-Nc7pUGg&ab_channel=SteveLan. Accessed: 2021-09-28.
- [133] Manfred Constapel, Marco Cimdins, and Horst Hellbrück. A practical toolbox for getting started with mmwave fmcw radar sensors. In *Proceedings of the 4th KuVS/GI Expert Talk on Localization*, 2019.
- [134] L. Lan, T. Polonelli, Y. Qin, N. Pucci, J. Arteaga, C. Kwan, D. Boyle, D. Yates, E. Yeatman, and P. Mitcheson. An induction-based localisation technique for wirelessly charged drones. In *2020 IEEE PELS Workshop on Emerging Technologies: Wireless Power Transfer (WoW)*, page Accepted, 2020.
- [135] Dji osdk. <https://developer.dji.com/onboard-sdk/documentation/introduction/homepage.html>. [datasheet] Accessed: 31 Oct 2021.
- [136] Stm32f4discovery. <https://www.st.com/en/evaluation-tools/stm32f4discovery.html>. [datasheet] Accessed: 31 Oct 2021.
- [137] Marko Malajner, Peter Planinšič, and Dušan Gleich. Uwb ranging accuracy. In *2015 International Conference on Systems, Signals and Image Processing (IWSSIP)*, pages 61–64, 2015.